INVESTIGATIONS ON THE STRUCTURAL, OPTICAL AND MAGNETIC PROPERTIES OF NANOSTRUCTURED CERIUM OXIDE IN PURE AND DOPED FORMS AND ITS POLYMER NANOCOMPOSITES

Thesis submitted to

Cochin University of Science and Technology

in partial fulfillment of the requirements

for the award of the Degree of

DOCTOR OF PHILOSOPHY

By

DHANNIA.T

DEPARTMENT OF PHYSICS

COCHIN UNIVERSITY OF SCIENCE AND TECHNOLOGY

COCHIN-682022

January 2012

INVESTIGATIONS ON THE STRUCTURAL, OPTICAL AND MAGNETIC PROPERTIES OF NANOSTRUCTURED CERIUM OXIDE IN PURE AND DOPED FORMS AND ITS POLYMER NANOCOMPOSITES

Ph.D thesis in the field of Material Science

Author:

Dhannia.T

Division for Research in Advanced Materials

Department of Physics

Cochin University for Science & Technology

Kochi- 682022, Kerala, India.

Email:dhanniat@gmail.com

Supervisor:

Dr. S. Jayalekshmi,

Professor,

Division for Research in Advanced Materials

Department of Physics

Cochin University for Science & Technology

Kochi- 682022, Kerala, India.

Email:jayalekshmi@cusat.ac.in

January 2012

Dr. S. Jayalekshmi
Professor
Division for Research in Advanced Materials
Department of Physics
Cochin University for Science & Technology
Kochi- 682022, Kerala, India.
Email:jayalekshmi@cusat.ac.in

Date: 30/01/ 2012

Certificate

Certified that the work presented in the thesis entitled "INVESTIGATIONS ON THE STRUCTURAL, OPTICAL AND MAGNETIC PROPERTIES OF NANOSTRUCTURED CERIUM OXIDE IN PURE AND DOPED FORMS AND ITS POLYMER NANOCOMPOSITES" is based on the research work carried out by ***Smt. Dhannia.T*** *under my guidance in the Department of Physics, Cochin University of Science And Technology and no part of this work has been presented by her for the award of any other degree.*

Dr. S. Jayalekshmi
(Supervising Guide)

Declaration

I hereby declare that the present work entitled "**INVESTIGATIONS ON THE STRUCTURAL, OPTICAL AND MAGNETIC PROPERTIES OF NANOSTRUCTURED CERIUM OXIDE IN PURE AND DOPED FORMS AND ITS POLYMER NANOCOMPOSITES**" is based on the original work done by me under the guidance of **Dr. S. Jayalekshmi**, Professor**,** Department of Physics, Cochin University of Science And Technology, and has not been included in any other thesis submitted previously for the award of any other degree.

Dhannia.T

Kochi- 22
30/01/2012

Dedicated to my beloved teachers

Acknowledgement

I would like to use this opportunity to express my sincere thanks and gratitude to Dr. S Jayalekshmi, Professor, Department of Physics, Cochin University of Science and Technology, for her excellent guidance and encouragement throughout the course of this work.

I am thankful to Prof. M. R. Anantharaman, the present Head of the Department of Physics and also to the former Heads of the Department of Physics Prof. K. Babu Joseph , Prof. M. Sabir, Prof. K. P. Rajappan Nair, Prof. Elizabeth Mathai, Prof. K.P Vijayakumar, Dr. V. C. Kuriakose, Dr. Ramesh Babu T, Dr. Godfrey Louis for providing all facilities. I express my gratitude to my teachers Prof. B. Pradeep, Prof. C. Sudha Kartha, Prof. T.M Abdhul Rasheed, Mr. M. M Kuttappan, Mr. P. K. Sarangadharan of the Department of Physics, Cochin University of Science and Technology.

I express my sincere thanks to Prof. T. Balasubramanian and Prof. D. Sastikumar Heads of the Department of Physics, National Institute of Technology, Thiruchirappalli for permitting me to do part of my research work in NIT, Trichy.

I am grateful to Dr. A. Chandrabose, Dr. J. Hemalatha and Dr. T. Prasada Rao, Department of Physics, National Institute of Technology, Thiruchirappalli, for their help to initiate the work in Nanotechnology during my stay in NITT. I am also thankful to Dr. R. Justin Josephyus and his students Mr. K. Prakash and Mr. T. Arun of Department of Physics, NITT for their valuable help in VSM and TGA measurements. I acknowledge with thanks the help and encouragement of all faculty members and research scholars of NITT.

I thank all the non-teaching staff of Department of the Physics, CUSAT, for their help and co-operation. The help extended by the technical staff of STIC and USIC, CUSAT, is also acknowledged.

I remember late Dr. K. Ravindranath of Acquinas College, Dr. Sajeev U S, Dr. Santhosh D shenoy, Dr. Sindhu S, Dr. Veena Gopalan, Dr. Vijutha Sunny, Dr. Sagar and Ms. Geetha with deep gratitude and affection. I would always remember Mr. Vimal, Dr. Pramitha, Saju sir and Anila teacher for the support given to me all through my research carrier.

I acknowledge the co-operative and helpful attitude of all my fellow research scholars in the Dream Lab in the Department of Physics.

Words are insufficient to express my acknowledgements for my colleagues in the school of Engineering, CUSAT, without whose advices, help and motivations, it would have not been possible to complete the research work.

And at last but not the least I have no words to express my thanks to my parents and husband, for they have been the inspiring force behind me.

Dhannia.T

Contents

Page No

PREFACE

In recent years, nanoscience and nanotechnology has emerged as one of the most important and exciting frontier areas of research interest in almost all fields of science and technology. This technology provides the path of many breakthrough changes in the near future in many areas of advanced technological applications. Nanotechnology is an interdisciplinary area of research and development. The advent of nanotechnology in the modern times and the beginning of its systematic study can be thought of to have begun with a lecture by the famous physicist Richard Feynman. In 1960 he presented a visionary and prophetic lecture at the meeting of the American Physical Society entitled "*there is plenty of room at the bottom"* where he speculated on the possibility and potential of nanosized materials.

Synthesis of nanomaterials and nanostructures are the essential aspects of nanotechnology. Studies on new physical properties and applications of nanomaterials are possible only when materials are made available with desired size, morphology, crystal structure and chemical composition. Cerium oxide (ceria) is one of the important functional materials with high mechanical strength, thermal stability, excellent optical properties, appreciable oxygen ion conductivity and oxygen storage capacity. Ceria finds a variety of applications in mechanical polishing of microelectronic devices, as catalysts for three-way automatic exhaust systems and as additives in ceramics and phosphors. The doped ceria usually has enhanced catalytic and electrical properties, which depend on a series of factors such as the particle size, the structural characteristics, morphology etc. Ceria based solid solutions have been widely identified as promising electrolytes for intermediate temperature solid oxide fuel cells (SOFC). The success of many promising device technologies depends on the suitable powder synthesis techniques. The challenge for introducing new nanopowder synthesis techniques is

to preserve high material quality while attaining the desired composition. The method adopted should give reproducible powder properties, high yield and must be time and energy effective. The use of a variety of new materials in many technological applications has been realized through the use of thin films of these materials. Thus the development of any new material will have good application potential if it can be deposited in thin film form with the same properties. The advantageous properties of thin films include the possibility of tailoring the properties according to film thickness, small mass of the materials involved and high surface to volume ratio. The synthesis of polymer nanocomposites is an integral aspect of polymer nanotechnology. By inserting the nanometric inorganic compounds, the properties of polymers can be improved and this has a lot of applications depending upon the inorganic filler material present in the polymer.

An important field of research is the development of new synthetic processes to produce ultrafine CeO_2 particles with nanocrystalline structure that heighten the performance of the material. So one of the important objectives of the present work is to synthesize nanostructured cerium oxide in pristine and doped forms using surfactant free, hydrolysis assisted chemical precipitation method which is a simple and cost effective technique. This method using cerium chloride and ammonia as precursors is a novel method for synthesizing nanostructured ceria, since this technique has not been pursued previously. Another important objective of the present work is to search for Room Temperature Ferromagnetism (RTFM) in nanostructured ceria (both in pristine and doped forms) and cerium oxide thin films deposited by spray pyrolysis technique. Detailed investigations on the optical and photoluminescence properties of hydrolysis assisted chemically synthesized nanostructured ceria both in the pristine and doped forms is another objective of the present work. polymer/ceria nanocomposites constitute an interesting field of research area which has not been subjected to extensive investigations. So in the present work

emphasis is also given to the synthesis of polymer/ceria nanocomposite using different polymers and their characterizations for possible practical applications.

In the present work nanocrystalline CeO_2 powder samples have been prepared by hydrolysis assisted chemical precipitation method employing cerium chloride and ammonia as precursors. Extensive investigations have been carried out on the structural and optical properties of nanostructured ceria and iron, aluminium and cobalt doped ceria. One of the highlights of these studies is the observation that both pure and doped ceria offer the prospects of applications as cost effective and non toxic inorganic material for efficient UV filtering in sunscreen cosmetics. RTFM has been observed for the first time in pure ceria nanocrystals synthesized by chemical precipitation technique and also in iron and cobalt doped ceria nanocrystals. RTFM is also reported for the first time in high quality cerium oxide thin films deposited by spray pyrolysis technique. The origin of RTFM has been ascribed to the presence of oxygen vacancies on the surface of ceria nanoparticles. Based on the experimental data good correlation between the magnetic, structural and optical properties of these samples has also been established. Based on the dependence of PL intensity on annealing temperature a self trapped exciton (STE) mediated PL mechanism has been proposed for the observed PL in ceria nanocrystals. The polymer/ceria nanocomposites prepared using a variety of polymers such as PVDF, PVA, PMMA and PS possess good UV absorption window regions of approximately 250 nm width. Hence these nanocomposites offer prospects of potential applications in the development of efficient UV filters.

The present thesis consists of eight chapters. The significance of nanomaterials and their applications in different areas of science and technology are briefly introduced in **chapter 1**. It gives some general ideas about nanomaterials and a brief review on ceria and related compounds. The objectives of the present investigations are also detailed in this chapter.

The **second chapter** describes the various experimental techniques employed for the preparation and characterization of the materials relevant to the present work. These include XRD, TEM, EDX and FTIR for structural characterization, Photoluminescence, Diffuse Reflectance and UV-Vis absorption spectroscopic techniques for optical characterization, TGA for thermal studies and VSM for magnetic studies.

In the **third chapter,** the preparation of cerium oxide nanoparticles by hydrolysis assisted chemical precipitation method using cerium chloride and ammonia precursors is addressed. This technique is a simple and cost effective one, without the need for any surfactants or high temperature and pressure conditions. The observation of STE mediated photoluminescence in pure cerium oxide forms the highlight of this chapter.

The **fourth chapter** includes the synthesis and characterization of aluminium, iron and cobalt doped cerium oxide nanoparticles prepared by the same simple chemical precipitation technique similar to the one used for synthesizing pure ceria. The structural and optical properties of these samples have been investigated in detail. The presence of α - Fe_2O_3 phase in iron doped ceria has been used to explain some of the observed features of the room temperature ferromagnetic behaviour of this sample, which forms a significant part of the next chapter.

The **fifth chapter** gives detailed investigations on the magnetic and thermal properties of pure ceria nanocrystals and transition metals (Fe and Co) doped ceria nanocrystals. RTFM has been observed first time in cerium oxide, both in pure and doped forms, synthesised by chemical precipitation technique. A detailed theoretical explanation of the observed RTFM has also been attempted.

The **sixth chapter** describes the preparation and characterization of ceria thin films using spray pyrolysis method. Spray pyrolysed thin films offer high film

quality and low processing costs compared to conventional thin films, prepared using techniques such as pulsed laser deposition and chemical or physical vapour deposition. Room temperature ferromagnetism has been observed in pure ceria thin films of the present study, for the first time. Though the magnetization value of ceria thin film is small compared to the bulk oxide, the observed signature of FM in ceria thin films is significant from the view point of applications in the development of spintronic devices.

In the **seventh chapter** a detailed discussion of the synthesis and various characterization of CeO_2 nanocomposites using different polymers such as PVDF, is included. Optical absorption and photoluminescence characteristics of these polymer nanocomposites have been investigated in detail.

Chapter eight is the concluding chapter of the thesis. General conclusions and inferences arrived at, based on the present investigations are summarized in this chapter. Suggestions for the improvements in the synthesis conditions are also discussed and the scope for further investigations are also high-lighted.

List of Publications

Journal Papers

[1] Effect of aluminium doping on structural and optical properties of cerium oxide nanoparticles, **T Dhannia**, S Jayalekshmi, M C Santhosh Kumar, T Prasada Rao and A Chandra Bose, J.Phys & Chem of solids, 70 (2009) 1443-1447.

[2] Effect of iron doping on structural and optical properties of cerium oxide nanoparticles, **T Dhannia**, S Jayalekshmi, M C Santhosh Kumar, Prasada Rao and A Chandra Bose, J.Phys & Chem of solids 71 (2010) 1020-1025

[3] Self Trapped Excitons in chemically precipitated cerium oxide nanocrystals, **T Dhannia**, S Jayalekshmi, M C Santhosh Kumar (under review)

[4] Magnetic study of chemically prepared Fe-doped ceria, **T Dhannia**, S Jayalekshmi, M C Santhosh Kumar (communicated)

[5] Synthesis, structural and optical properties of Polymer/Ceria nanocomposites, **T Dhannia** and S Jayalekshmi (communicated)

[6] Structural and optical properties of ceria thin film, **T Dhannia**, T Prasada Rao, M C Santhosh Kumar, S Jayalekshmi (communicated)

Conference Papers

[1] **T Dhannia**, S Jayalekshmi, M C Santhosh Kumar, T Prasada Rao and A Chandra Bose, Structural and optical properties of chemically prepared cerium oxide nanocrystals, National Conference on New Horizons in theoretical and experimental Physics (NHTEP-2007), Department of Physics, Cochin University of Science & Technology.

[2] **T Dhannia**, S Jayalekshmi, M C Santhosh Kumar, T Prasada Rao and A Chandra Bose, Lattice constant dependence of particle size of doped cerium oxide nanoparticles on annealing, National conference on Emerging materials and technologies for India-2020, Department of Metallurgical and Materials Engineering, NITT, TamilNadu, 2008.

[3] **T Dhannia**, S Jayalekshmi, M C Santhosh Kumar and T Prasada Rao The effect of annealing on the structural and optical properties of aluminium doped cerium oxide nanocrystals, Proceedings of 53rd DAE Solid State Physics Symposium, 2008.

[4] **T Dhannia**, S Jayalekshmi, M C Santhosh Kumar, Aluminium doped nanocrystalline cerium oxide-a new material for SOFC, Cochin nano-2009, Department of Physics, Cochin University of Science & Technology

Chapter 1
INTRODUCTION

Contents

1.1. Nanoscience and Nanotechnology

Research in nanoscience and nanotechnology has gained considerable momentum in the last 15 years, owing to its present and future applications in various walks of life like consumer electronics, sensors, health care, nanomedicine, food technology etc. Nanoscience is the study of phenomena and manipulation of materials at atomic, molecular and macromolecular scales, where properties differ significantly from those at a larger scale. Nanotechnology is a new field or a new scientific domain. Similar to quantum mechanics, on nanometer scale, materials or structures may possess new physical properties or exhibit new physical phenomena. Some of these properties are already known. There may be many more unique physical properties not known to us yet. These new physical properties or phenomena may not satisfy everlasting human curiosity, but offer the prospects of new advancements in technology. Nanotechnology also promises the possibility of creating nanostructures of metastable phase with non-conventional properties including superconductivity and magnetism. Yet another very important aspect

of nanotechnology is the miniaturization of current and new instruments, sensors and machines that will greatly impact the new world we live in. Nanotechnology has an extremely broad range of potential applications from nanoscale electronics and optics to nanobiological systems and nanomedicine, to new materials and therefore it requires formation of and contribution from multidisciplinary teams of physicists, chemists, material scientists, engineers and molecular biologists. Such a multidisciplinary team of workers has to work together on (1) synthesis and processing of nanomaterials and nanostructures, (2) understanding the physical properties related to the nanometer scale, (3) design and fabrication of nanodevices or devices with nanomaterials as building blocks, and (4) design and construction of novel tools for characterization of nanostructures and nanomaterials [1].

The applications of nanomaterials utilize not only chemical composition but also the size, shape and surface dependent properties. These properties of nanoparticles in novel applications lead to remarkable performance characteristics. Particles with size smaller than the wavelength of visible light have an important role in a broad range of applications in material science. Synthesis of nanomaterials with well-controlled size, morphology and chemical composition may open new opportunities in exploring new and enhanced physical properties. The recent emergence of tools and techniques capable of constructing structures with dimensions ranging from 0.1 nm to 50 nm has opened up numerous possibilities for investigating new devices in this size domain, which was inaccessible to experimental researchers till now. Decreasing dimension in microelectronic and optoelectronic devices requires knowledge of material properties below a critical size [2].

There are two approaches for the preparation of nanostructures. They are top-down and bottom up approaches. In bottom-up approach, the atoms and

molecules are collected, consolidated and fastened together into the structure. This is carried out by a sequence of chemical reactions controlled by catalysts. In top-down method, a large scale object or pattern gradually gets reduced in dimensions to form nanostructures. This can be accomplished by a technique called lithography in which radiation through a template is given to a surface coated with a radiation sensitive resist; the resist is then removed and the surface is chemically treated to produce the nanostructures [2]. When the size or dimension of a material is continuously reduced from a large or macroscopic size to a very small size, the properties remain the same at first, and then small changes begin to occur, until finally when the size drops below 100 nm, dramatic changes in properties occur. If one dimension is reduced to the narrow range while the other two dimensions remain large, then we obtain a structure known as quantum well. If two dimensions are so reduced and one remains large, the resulting structure is referred to as a quantum wire. The extreme case of this process of size reduction in which all the three dimensions reach low nanometer range is called quantum dot.

Nanoparticles can be produced by a variety of methods. These include combustion synthesis, plasma synthesis, wet-phase processing, chemical precipitation, sol-gel processing, microwave synthesis, mechanical processing, mechanochemical synthesis, high-energy ball-milling, chemical vapour deposition, laser ablation etc. In the sol-gel process, alkoxide or organo-metallic compounds are usually used as precursors. However, the expensive precursor materials and more complicated reaction mechanism often restrict the potential use of sol-gel process. The reactions for hydrothermal synthesis and forced hydrolysis are often carried out under several different conditions, such as higher temperature, higher pressure and longer reaction time [3]. In microwave synthesis, electromagnetic radiation with frequency range of 0.3-300GHz and

corresponding wavelengths from 1mm to 1m is employed. In the microwave irradiation region, the frequency of applied irradiation is low enough so that the dipoles have time to respond to the alternating electric field and therefore rotation. However, the frequency is not high enough for the rotation to precisely follow the field, which causes energy to be lost from the dipole by molecular friction and collision, giving rise to the dielectric heating [4]. In micro-emulsion method, it is necessary to mix micro-emulsion containing ions to be precipitated with another kind of micro emulsion, solid or gas containing precipitants. It is a very efficient method for preparing highly monodispersed nanoparticles, but is hard to scale up commercially. The oxide particles obtained by ceramic processes are rather large and non uniform in size. These non uniform particles result in scratching or rough surfaces in polishing [5]. Solvothermal synthesis utilizes a solvent under pressure and temperatures above its critical point to increase the solubility of a solid and to speed up reactions between solids [6]. Most of these techniques are complex, energy consuming and expensive. Compared to these methods, precipitation is more attractive because cheap salt precursors are needed and the operation is simple and quite suitable for mass production. Moreover, the reaction conditions of precipitation are mild and adjustable for satisfying a variety of purposes [3]. In homogeneous precipitation process, the precipitants can be uniformly generated on-site by their precursors. Homogeneous precipitation method, which is based on acid-base reaction, is convenient for preparing rare earth oxides from a view point of industrial application as well as a lab scale experiments [7].

The optical properties of nanoparticles are markedly different from those of bulk. In the case of metals, as the size of the particle decreases we start observing oscillations of electron gas on the surface of nanoparticles. These oscillations are called surface plasmons. So, if the nanoparticles are exposed to

an electromagnetic wave having a wavelength comparable to or greater than the size of the nanoparticles and the light has a frequency close to that of the surface plasmon then the surface plasmon would absorb energy. Thus nanoparticles start exhibiting different colors as their size changes and the frequency of the surface plasmon changes with it. This frequency of the surface plasmon absorption is a function of the dielectric constant of the material, size of the particles and also the specific geometrical shape that the particle has. In the case of semiconducting naoparticles the properties change in a different fashion. One of the important properties that changes as the size of the nanoparticles changes is the absorption spectrum of the material. The strength of the absorption depends on the material and wavelength passed. For a given material in its bulk state, the absorption spectrum is unique. But when the material is in the form of nanostructures then the absorption spectrum changes and undergoes a blue shift. The nanostructures have a different density of states compared with the bulk state. This change in density of states has implications on the electrical properties of nanoparticles.

Physical properties of a semiconductor are related to its band gap, which can be substantially modified (increased or decreased), by doping. The magnitude of the shift is determined by two competing mechanisms. There is a band gap narrowing (BGN) which is a consequence of many body effects on the conduction and valence bands. The shrinkage is counteracted by the Burstein-Moss effect, which gives a band gap widening (BGW) as a result of the blocking of lowest states in the conduction band [8].

Magnetic nanoparticles show a variety of unusual magnetic behavior when compared with the bulk materials. This is mostly due to surface/interface effects, including symmetry breaking, electronic environment/charge transfer and magnetic interactions. The diverse applications of magnets require the

magnetization curve to have different properties. Nanostructuring of magnetic materials can be used to design the magnetization curve of the material at hand. The dynamics of magnetization and demagnetization of magnetic materials in any device are governed by the presence of domain walls and regions having magnetization in different directions. These phenomena change the hysteresis loop of magnetic nanoparticles as compared to bulk material. Due to the formation of nanoparticles the atoms which are on the surface are now facing different potentials in different directions. The resulting surface stress in nanoparticles modifies its mechanical and structural properties.

Spray pyrolysis has been developed as a powerful tool for the deposition of various kinds of thin films such as metal oxides and nanophase materials. In comparison with other techniques, it has several advantages such as high purity and excellent control of chemical uniformity in multi component system. It can be adapted easily for production of large area films. Spray pyrolysis method is a one step synthesis process in which a precursor solution is sprayed by means of a compressed carrier gas. During spray-pyrolysis deposition, a precursor solution of metal salts and solvents is sprayed as fine droplets onto a heated substrate. When the droplets reach the heated substrate, they spread out and undergo pyrolytic decomposition. Newly deposited flat droplets, with thickness in the 10-20 nm range, pile up on the previously deposited ones and undergo pyrolytic decomposition as well. This process continues until a film thickness of 100-500 nm is reached. The degree of decomposition is determined by the relation between substrate temperature, the boiling point of the solvents and the melting point of the salts used for the precursor [9]. It is a simple and cost effective method for the deposition of variety of thin films. Only limited data is available on the preparation of ceria thin films using spray pyrolysis technique. CeO_2 thin films are attractive for various electronic and optical applications,

such as silicon-on-insulator structures, miniaturized stable capacitors, oxygen sensors, optical coatings etc.

Synthesis and characterization of nanosized metal polymer composites have been particularly gaining importance due to their potential applications in biomedical, electronic and optical devices and also as heterogeneous green catalysts. Generally such composites are synthesized in two to three steps wherein the polymer and metal particles are prepared separately followed by mechanical mixing or metal/ metal oxide particles are generated inside the already prepared polymer by vapor deposition or by reduction/oxidation etc.

Nanocomposites can be obtained by two different approaches viz, in-situ and ex-situ techniques. In the in-situ methods, nanoparticles are generated inside a polymer matrix by decomposition or chemical reduction of a metallic precursor dissolved into the polymer. In the ex-situ approach, nanoparticles are first produced by soft-chemistry routes and then dispersed into polymer matrices. General methods for processing nanocomposites are mechanical alloying, sol-gel synthesis and thermal spray synthesis. Mechanical alloying occurs as a result of repeated breaking up and joining of the component particles. This method can prepare highly metastable structures such as amorphous alloys and nanocomposite structures with high flexibility. In sol-gel method, metal or main group element compounds undergo hydrolysis and condensation reactions giving gel materials with extended three-dimensional structures. These methods are commonly used to prepare nanocomposite materials because the method occurs readily with a wide variety of precursors and can be conducted at or near room temperature. Thermal spray coating is very effective because agglomerated nanocrystalline powders are melted, accelerated against a substrate and quenched very rapidly in a single step. Usually the preparative scheme allows obtaining nanoparticles whose surface

can be passivated by monolayers of suitable agents like n- alkanethiol molecules. Surface passivation has a fundamental role since it avoids aggregation and surface oxidation or contamination phenomenon. General methods for processing nanocomposites are mechanical alloying, sol-gel synthesis, and thermal spray synthesis. Nowadays polymer based nanocomposites are of considerable interest in research areas because of their ability to combine the advantages of both polymers and filler components. There are several applications of polymeric nanocomposites based on their optical, electrical, mechanical and magnetic properties. The use of inorganic nanoparticles into the polymer matrix can provide high performance novel materials that find applications in many industrial fields. With this respect, frequently considered features are optical properties such as light absorption (UV and color), the extent of light scattering, photoluminescence and magnetic properties such as super-paramagnetism, electromagnetic wave absorption etc [10].

1.2. Cerium Oxide: structure, properties and applications

The nanoscience and nanotechnology have brought about new chances for new applications of some traditional materials, such as ceria-based materials, which are of great interest due to their wide applications, in particular, as redox or oxygen storage promoters in the three-way catalysts, catalysts for H_2 production from fuels, solid state conductors for fuel cells etc. Cerium is the most abundant element in lanthanides or rare earth elements in the periodic table in which the inner 4f electron shell is being filled. The most stable oxide of cerium is cerium dioxide, CeO_2, also called ceria or ceric oxide. Cerium (atomic number 58, atomic weight 140.12) can be chemically present in two stable valence states, Ce^{4+} (ceric) and Ce^{3+} (cerous), and this property triggers several technological uses. The ground state of all neutral Ln atoms is

probably either [Xe] $4f^n5d^16s^2$ or [Xe] $4f^{n+1}6s^2$ where the increase in n from 0 to 14 corresponds to the change from La to Lu. Cerium is the second and most reactive member of the Ln series. It is highly electro-positive and is predominantly ionic due to the low ionization potential for the removal of the three most weakly bound electrons. The energetics is such that for all lanthanides, the most stable state is a trivalent one (Ln^{3+}) with [Xe] $4f^n$ configuration; i.e. for Ce^{3+}, it is [Xe] $4f^1$. The 4f electrons have well-shielded inner orbital which are not influenced by the external environment and hence the chemical behavior of all Ln^{3+} ions, including Ce^{3+}, is very similar. At the start of the Ln series, the 5d orbitals are not much higher in energy than the 4f shell. However, in the case of cerium a potential 4f−5d charge transition accounts for the absorption by Ce (III) compounds in the UV region just outside the visible region. The relative increased stability of empty $4f^0$, half-full $4f^7$, and completely full $4f^{14}$ shells for certain elements can cause oxidation states other than three also to be reasonably stable, in particular Ce^{4+} with a [Xe] $4f^0$ configuration [11].

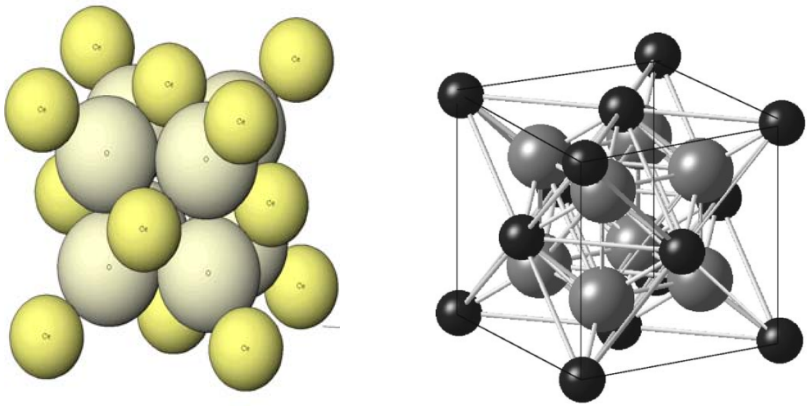

Figure 1.1: The crystal structure of CeO_2

Ceria has the fluorite (CaF_2) structure, space group Fm3m (a = 0.541134 nm, JCPDS 34-394) with 8-coordinate cations and 4-coordinate anions. In other

words, each cerium cation is coordinated to eight equivalents nearest oxygen anions at the corner of a cube, each anion being tetrahedrally coordinated by four cations. The structure is illustrated in figure 1.1. Extending this structure by drawing cubes of oxygen ions at each corner reveals the eightfold cubic co-ordination of each cerium, which alternately occupies the centre of the cube. This clearly shows that there are large vacant octahedral holes in the structure, a feature, which will be significant when movement of ions through the defect structure is considered. Ceria has only one crystallographic form throughout the range of temperatures. It has a strong tendency to remain in the fluorite-structured lattice even after losing considerable amount of oxygen, thus stabilizing a structure with an elevated number of oxygen vacancies [11].

Powdered ceria is slightly hygroscopic and will absorb a small amount of carbon dioxide from the atmosphere. Cerium also forms cerium (111) oxide but CeO_2 is the most stable phase at room temperature and under atmospheric conditions. Oxygen atoms in CeO_2 units are very mobile and easily leave the ceria lattice, giving rise to a large variety of non-stoichiometric oxides with two limiting cases being CeO_2 and Ce_2O_3.

Oxides with the cubic fluorite structure like ceria (CeO_2) are known to be good solid electrolytes when they are doped with cations of lower valency than the host cations. The high ionic conductivity of doped ceria makes it an attractive electrolyte for solid oxide fuel cells, whose prospects as an environmentally friendly power sources are very promising. In these electrolytes, the current is carried by oxygen ions that are transported by oxygen vacancies, present to compensate for the lower charge of the dopant cations. Doped ceria with trivalent ions results in a lowering of the energy barrier for oxygen migration. A clear physical picture of the connection between the

choice of a dopant and the improvement of ionic conductivity in ceria is still lacking [12].

It has been proved that the lattice of CeO_2 can be modified by incorporating metal ions with smaller radius and lower valence such as Fe, Cu, Mn or larger lanthanide elements with similar properties to Ce. The key factor in the design of modified ceria is the choice of dopant elements, as well as their amount introduced. In addition, the preparation method of the powder has also very strong influence on the homogeneity and stability of the solid solutions. Nanosized doped ceria with oxides of di or trivalent metals are shown to be a promising solid electrolyte with good ionic conductivity at low temperatures. The partial replacement of Ce^{4+} ions with di or trivalent ions produces large density of oxygen vacancies in ceria lattice enhancing the conductivity of these materials. Because of its lower valence state than ceria and low price, a good candidate for doping can be iron. No detailed analysis has been reported on the properties of ceria prepared by chemical precipitation method and doped with dopants such as iron, aluminium, cobalt etc.

The search for room temperature ferromagnetism (RTFM) in non magnetic oxides including cerium oxide has been the subject of extensive research during the past few years. Though there are a few reports related to the observation of RTFM in nanostructured ceria both pristine and doped forms, in all these reports the synthesis of cerium oxide involves special synthesis conditions such as the presence of surfactants, high temperature and pressure conditions etc. There are no reports on the observation of RTFM in cerium oxide synthesized by hydrolysis assisted chemical precipitation technique. This technique is simple and cost effective technique [13] and is the one employed for the synthesis of cerium oxide in the present study.

The value of the magnetic moment is the measure of the strength of the magnetism that is present in the material. Atoms in various transition series of the periodic table have unfilled inner energy levels in which the spins of the electrons are unpaired, giving the atom a net magnetic moment. Several recent studies have pointed out that oxygen vacancies, F-centers and defects in diluted magnetic semiconductor (DMS) systems play a major role in the magnetic exchange mechanism. Ferromagnetic (FM) ordering through F-centre exchange mechanism is mediated by oxygen vacancies and strongly depends on the valence state of Fe dopant [14].

The major drawback of the ceria based electrolytes is that, Ce^{4+} can be reduced to Ce^{3+} under reducing conditions at high temperatures above 700 ^{0}C, resulting in high electronic conductivity, which is detrimental to the functioning of electrolyte in the SOFCs. Also in polycrystalline ceria based electrolytes, the impurities such as Si and Ca segregate at grain boundaries and form thin blocking layers within the grain boundary network, which affect the grain boundary conductivity. One way of reducing the larger contribution of segregated impurities is to reduce the grain size, so that the grain boundary per unit volume is increased and the total amount of impurities can be spread over a large interfacial area. Also, it has been speculated that, in the nanostructured materials, grain boundary may provide fast diffusion pathway for ionic defects resulting in enhanced ionic conductivity in the finely grained materials. So the nanocrystalline materials with improved electrochemical properties are expected to overcome some of the draw backs associated with microcrystalline ceria based electrolyte, opening wide range of applications in the intermediate temperature range. Therefore, in recent years, the nanostructured ceria based electrolyte materials doped with different dopants and dopant concentrations have attracted a great interest for their development as electrolyte materials for SOFCs. Currently

enormous effects are being made to understand the electrolyte properties of nanoscale ceria based materials for application purpose [12].

1.3. A Brief Review

Synthesis forms a vital aspect of the science of nanomaterials. Chemical methods have proved to be more effective and versatile than physical methods and have therefore, been employed widely to synthesize a variety of nanomaterials including nanocrystals, nanowires, nanotubes etc.

1.3.1. Pure and doped ceria

The synthesis of nanomaterials with controlled size and composition has become one of the important topics of colloid and materials chemistry because of their size or shape dependent properties**.** Recently, several methods have been developed to prepare pure and doped CeO_2 powder, including wet chemical synthesis, thermal hydrolysis, flux method, hydrothermal synthesis, gas condensation method, microwave technique, sonochemical, reverse micellar synthesis, solvothermal method, mechano-chemical, sol-gel method, composite-hydroxide-method, precipitation, thermal decomposition, polymer method combustion synthesis, SPRT method, microemulsion method, electrochemical method, low temperature decomposition method, precursor-growth- calcination process, citrate method, solid state synthesis, polyol method, ball milling method, freeze drying etc. [15 - 93]. Among these methods, precipitation is more attractive because it is a simple technique which requires easily available and cost effective precursors. There is also a possibility for the mass production quite easily. Although CeO_2 in doped and pristine form have already been studied, there are no reports on systematic investigations related to the synthesis and properties of nanostructured cerium oxide (both in pristine and doped forms)

using the cost effective technique of hydrolysis assisted chemical precipitation technique.

1.3.2. Ceria thin films

Different thin film deposition methods have been employed for ceria. The various techniques can be divided into three main classes: 1) chemical processes, MO-CVD, spray pyrolysis, sol-gel, flame–assisted vapor deposition etc. 2) Physical methods-sputtering, laser ablation etc. 3) ceramic powder processes-tape casting, screen printing, atomic layer deposition etc. [94-125].

Spray pyrolysis is an attractive thin film preparation method because it is inexpensive and can be used to deposit large area films. Spray-pyrolysed thin films offer high film quality and low processing costs compared to conventional thin film preparation techniques such as pulsed laser deposition and chemical or physical vapor deposition. There are a few reports on the preparation of nanostructured cerium oxide thin films using spray pyrolysis technique. Hence in the present work, attempts have been made to prepare high quality cerium oxide thin films using spray pyrolysis technique and investigate the structural, optical and magnetic properties of these films.

1.3.3. Polymer/Ceria nanocomposites

Even though many polymer/metal nanocomposite systems have been extensively studied, polymer/ceria nanocomposite systems have not been given much attention [126-128]. Hence, the part of the present investigation is devoted to the synthesis and characterization of polymer/ceria nanocomposite systems using different polymers such as PVDF, PMMA, PS and PVA.

1.4. Objectives of the present work

Most of techniques employed for the preparation of nanoparticles and thin films are complex, energy consuming, and expensive. Therefore, simple and cost effective routes to synthesize nanoparticles by utilizing cheap, nontoxic and environmentally benign precursors have to be identified and implemented. The work present in the thesis is centered around the synthesis of nanostuctured ceria in pristine and doped forms, the preparation of ceria thin films using spray pyrolysed technique, the synthesis of polymer/ceria nanocomposites and detailed investigations on the various properties of these systems. An important field of research is the development of new synthetic processes to produce ultrafine CeO_2 particles with nanocrystalline structure that heighten the performance of the material.

The objectives of the present work can be summarized as follows.

- In the present work emphasis is given to the synthesis of nanostructured cerium oxide in pristine and doped forms using surfactant free, hydrolysis assisted chemical precipitation method which is a simple and cost effective technique. This method, using cerium chloride and ammonia as precursors is a new approach for synthesizing nanostructured ceria, since this technique has not been pursued previously.
- Room temperature ferromagnetism (RTFM) has been reported in nanostructured ceria synthesized using variety of techniques, however, there are no reports related to RTFM in ceria synthesized by the hydrolysis assisted precipitation method. One of the important objective

of the present work is to search for RTFM in nanostructured ceria (both in pristine and doped forms) and finds a correlation between the observed magnetic, structural and optical properties.

- Detailed investigations on the optical and photoluminescence properties of hydrolysis assisted chemically synthesized nanostructured ceria both in the pristine and doped forms is the another objective of the present work.
- Attempts will be making for RTFM in cerium oxide thin films deposited by spray pyrolysis deposition technique.
- Polymer/ceria nanocomposites constitute an interesting field of research area which has not been subjected to extensive investigations
- In the present work emphasis is also given to the synthesis of polymer/ceria nanocompoiste using different polymers and their characterizations for possible practical applications.

Reference

[1] G Gao, Nanostructures & Nanomaterials, Synthesis, Properties & Applications, Imperial College press, London(2004)

[2] T Pradeep, Nano: The Essentials, Understanding Nanoscience and Nanotechnology, Tata Mc Graw- Hill Publishing Company Limited, New Delhi (2007)

[3] H Chen, H Chang, Colloids and Surfaces A: Physicochem.Eng. Aspects 242 (2004) 61

[4] H Yang, C Huang, A Tang, X Zhang, W Yang, Mat. Res. Bull. 40 (2005) 1690

[5] Y He, B Yang, G Cheng, Mat. Lett. 57 (2003)1880

[6] C Sun, H Li, H Zhang, Z Wang, L Chen, Nanotechnology 16 (2005) 1454

[7] M Ozawa, R Onoe, H Kato, J. Alloys. Compd. 408-412 (2006) 556

[8] A Jain, P Sagar, R M Mehra, Solid State Electronics 50 (2006) 1420

[9] T Prasada Rao, Ph.D Thesis, Preparation of n-type and p-type Zno thin films for optoelectronic applications (2011)

[10] T Hanemann, D V Szabo, Materials 3 (2010) 3468

[11] B T Kilbourn, Cerium and cerium compounds, Ulllmann's encyclopedia Vol 5.

[12] D A Andersson, S I Simak, N V Skorodumova, I A Abrikosov, B Johansson, PNAS 83 (1996) 1

[13] A C Bose, R Ramamoorthy, S Ramaswamy, Mat. Lett. 44 (2000) 203

[14] Z D Dohcevic-Mitrovic, N Paunovic, M Radovic, Z V Popovic, B Matovic, B Cekic, V Ivaanovski, Appl. Phys. Lett. 96 (2010) 203104

[15] M Hirano, Y Fukuda, H Iwata, Y Hotta, M Inagaki, J. Am. Ceram. Soc. 83 (5) (2000) 1287

[16] F Bondioli, A B Corradi, C Leonelli, T Manfredini, Mat. Res. Bull. 34, 14/15 (1999) 2159

[17] K Kaneko, K Inoke, B Freitag, A B Hungria, P A Midgley, T W Hansen, J Zhang, S. Ohara, T. Adschiri, Nanoletters 72 (2007) 421

[18] Z Yang, K Zhou, X Liu, Q Tian, D Lu, S Yang, Nanotechnology 18 (2007) 185606

[19] A I Y Tok, F Y C Boey, Z Dong, X L Sun, J. Mater. Process. Tech 190 (2007) 217

[20] F Zhou, X Ni, Y Zhang, H Zheng, J. Colloids. Inter. Sci. 307 (2007) 135

[21] S Dikmen, P Shunk, M Greenblatt, Solid State Ionics 126 (1999) 89

[22] G Li, R L Smith, H Inomata, J. Am. Chem. Soc. 123 (2001) 11091

[23] G Xiao, S Li, H Li, L Chen, Microporous and Mesoporous Materials 120 (2009) 426

[24] Y M Chiang, E B Lavik, I Kosacki, H L Tuller, J Y Ying, Appl. Phys. Lett. 69 (2) (1996) 8

[25] T Nakayama, B Skarman, L R Wallenberg, T Sekino, Y H Choa, T A Yamamoto, K Niihara, Scripta Mater. 44 (2001) 1929

[26] H Yang, C Huang, A Tang, X Zhang, W Yang, Mat. Res. Bull. 40 (2005) 1690

[27] M L Dos Santos, R C Lima, C S Riccardi, R L Tranquilin, P R Bueno, J A Varela, E Longo, Mat. Lett. 62 (2008) 4509

[28] H S Potdar, S B Deshpande, S P Gokhale, S K Date, Y B Khollam, A J Patil, Mat. Chem. Phy. 74 (2002) 306

[29] H Wang, J Zhu, J Zhu, X Liao, S Xu, T Ding, H Chen, Phys. Chem. Chem. Phys. 4 (2002) 3794

[30] S Sathyamurthy, K J Leonard, R T Dabestani, M P Paranthaman, Nanotechnology 16 (2005) 1960

[31] C Sun, H Li, H Zhang, Z Wang, L Chen, Nanotechnology 16 (2005) 1454

[32] Y X Li, W F Chen, X Z Zhou, Z Y Gu, C M Chen, Mat. Lett. 59 (2005) 48

[33] V N Morris, R A Farrell, A M Sexton, M A Morris, J. Phy: Conf. Series 26 (2006)119

[34] C Liu, L Luo, X Lu, Kinetics and Catalysis 49 (2008) 676

[35] M Gateshki, M Niederberger, A S Deshpande, Y Ren, V Petkov, J. Phys: Cond. Matter 19 (2007) 156205

[36] K S Kumar, T Mathews, J. Alloys Compd. 391 (2005) 177

[37] P C A Brito, D A A Santos, J G S Duque, M A Macedo, Physica B 405 (2010) 1821

[38] C Hu, Z Zhang, H Liu, P Gao, Z L Wang, Nanotechnology 17 (2006) 5983

[39] C Xia, C Hu, P Chen, B Wan, X He, Y Tian, Mater. Res. Bull. 49 (2010) 794

[40] Nagai, T Yamamoto, T Tanaka, T Nonaka, A Suda, Physica Scripta T 115 (2005) 664

[41] M Boaro, A Trovarelli, J Hwang, T Mason, Solid State Ionics 147 (2002) 85

[42] A I Y Tok, L H Luo, F Y C Boey, J. Mater. Res. 21 (2006) 1

[43] V Thangadurai, P Kopp, J. Power Sources 168 (2007) 178

[44] C Y Kang, H Kusaba, H Yahiro, K Sasaki, Y Teraoka, Solid State Ionics 177 (2006) 1799

[45] E Suda, B Pacaud, M Mori, J. Alloys. Compd. 408-412 (2006) 1161

[46] Z Tianshu, P Hing, H Huang, J Kilner, Solid State Ionics 148 (2002) 567

[47] T H Yeh, C Chou, Physica Scripta T1129 (2007) 303

[48] T Oshita, Y Sawaki, M Kishimoto, J. Alloys. Compd. 408-412 (2006) 1118

[49] B Zhu, X Liu, M Sun, S Ji, J Sun, Solid State Sciences 5 (2003) 1127

[50] A Thurber, K M Reddy, V Shutthanandan, M H Engelhard, C Wang, J Hays, A Punnoose, Physical Review B 76 (2007) 165206

[51] L Truffault, M Ta, T Devers, K Konstantinov, V Harel, C Simmonard, C Andreazza, I P Nevirkovets, A Pineau, O Veron, J Blondeau, Mat. Res. Bull. 45 (2010) 527

[52] Y Liu, Z Lockman, A Aziz, J Macmanus-Driscoll, J Phys: Cond. Matt. 20 (2008) 165201

[53] S Kumar, Y J Kim, B H Koo, H Choi, C G Lee, IEEE Trans of Magnetics 45 (2009) 2439

[54] F Zhang, S Chan, J E Spanier, E Apak, Q Jin, Appl. Phy. Lett. 80 (2002) 1

[55] D Zhang, X Ni, H Zheng, X Zhang, J Song, Solid State Sciences 8 (2006) 1290

[56] H Chen, H Chang, Solid State Comm. 133 (2005) 593

[57] J Zhang, Z Y Wu, L X Rong, B Z Dong, Physica Sripta, T 115 (2005) 661

[58] H Chen, H Chang, Ceramics Inter. 31(2005) 795

[59] L Mei, W Mitang, L Zhaogang, H U Yanhong, W U Jinxiu, J. Rare Earths 27 (2009) 991

[60] G Wang, Q Mu, T Chen, Y Wang, J. Alloys. Compd. 493 (2010) 202

[61] Y Liu, Z Lockman, A Aziz, J M Driscoll, J. Phy: Condens. Matter 20 (2008) 165201

[62] M G Sujana, K K Chattopadyay, S Anand, Appl. Surf. Sci 254 (2008) 7405.

[63] Y Konishi, T Murai, S Asai, Ind. Eng. Chem. Res. 36 (1997) 2641

[64] M Yan, W Wei, N Zuoren, J. Rare earths 25 (2007) 53

[65] D Xu, Q Wang, Y Tang, Z Lu, Z Liu, S Liu, G Zhang, W Su, J. Phys: Cond. Matt. 14 (2002)11265

[66] S Y Chen, Y Lu, T Huang, D Yan, C Dong, J. Phys. Chem. C 114 (2010) 19576

[67] S Phoka, P Laokul, E Swatsitang, V Promarak, S Seraphin, S Maensiri, Mat. Chem. Phy.115 (2009) 423

[68] W Shan, W Shen, C Li, Chem. Mater 15 (2003) 4761

[69] X Chen, G Li, Y Su, X Qiu, L Li, Z Zou, Nanotechnology 20 (2009) 115606

[70] A Gayen, K R Priolkar, A K Shukla, N Ravishankar, M S Hegde, Mat. Res. Bull. 40 (2005) 421

[71] C Peng, Z Zhang, Ceramics Inter. 33 (2007) 1133

[72] Z Dohcevic-Mitrovic, M J Scepanovic, M U Grujic Brojcin, Z V Popovic, S Boskovic, B Matovic, F Aldinger, Solid State Comm. 137 (2005) 387

[73] S Babu, R Thaneeru, T Inerbaev, R Day, A E Masunov, A Schulte, S Seal, Nanotechnology 20 (2009) 085713

[74] Z D Dohcevic-Mitrovic, N Paunovic, M Radovic, Z V Popovic, B Matovic, B Cekic, V Ivaanovski, Appl. Phys. Lett. 96 (2010) 203104

[75] B Matovic, Z Dohcevic-Mitrovic, M Radovic, Z Brankovic, G Brankovic, S Boskovic, Z V Popovic, J. Power Sources 193 (2009) 146

[76] Y He, B Yang, G Cheng, Mat. Lett. 57 (2003) 1880

[77] R Thanneeru, S Patil, S Deshpande, S Seal, Acta Materialia 55 (2007) 3457

[78] T Wang, D Sun, Mater. Res. Bull. 43 (2008) 1754

[79] J M Heintz, J C Bernier, J. Mat. Sci. 21 (1986) 1569

[80] L Guo-cong, C Li-miao, D Xue-chen, L Da-wen, Trans. Nonferrous Met. Soc. China 18 (2008) 897

[81] C Peng, Z Zhang, Ceramics Inter. 33 (2007) 1133

[82] H Lv, H Tu, B Zhao, Y Wu, K Hu, Solid State Ionics 177 (2007) 3467

[83] A K Baral, V Sankaranarayanan, Appl. Phys. A 98 (2010) 367

[84] L R Shah, B Ali, H Zhu, W G Wang, Y Q Song, H W Zhang, S I Shah, J Q Xiao, J. Phys. Cond. Matt. 21 (2009) 486004

[85] Q Wen, H Zhang, Q Yang, Y Song, M Han, IEEE Trans of Magnetics 44 (2008) 2704

[86] Q Wen, H Zhang, Y Song, Q Yang, H Zhu, J Q Xiao, J. Phys: Cond. Matt. 19 (2007) 246205

[87] P Datta, P Majewski, F Aldinger, Materials Characterization 60 (2009)138

[88] H Yamamura, S Takeda, K Kakinuma, Solid State Ionics 178 (2007) 1059

[89] Q Wen, H Zhang, Y Song, Q Yang, H Zhu, IEEE Transactions on Magnetic 44 (2008) 2704

[90] T Karaca, T Gurkaynak, M F Oksuzomer, Ceramics Inter. 36 (2010)1101

[91] T S Zhang, J Ma, L B Kong, Z Q Zeng, P Hing, J A Kilner, Mat. Sci. Eng. B103 (2003) 177

[92] J C C Abrantes, D Perez-coll, P Nunez, J R Frade, Electrochimica Acta 48 (2003) 2761

[93] V Petrovsky, B P Gorman, H U Anderson, T Petrovsky, J. Appl. Phys. 90 (2001) 2517

[94] I K Skofic, S Sturm, M Ceh, N Bukovec, Thin Solid Films 422 (2002)170

[95] A Thurber, K M Reddy, V Shutthanandan, M H Engelhard, C Wang, J A Punnoose, Phys. Rev. B 76 (2007) 165206

[96] Turkovic, P Dubcek, S Bernstorff, Mat. Sci. Eng. B85 (1999) 263

[97] A Verma, A K Bakhshi, S A Agnihotry, Solar Energy Mat. Solar Cells 90 (2006) 1640

[98] N Ozer, Sol. Ener. Mat. Solar Cells 68 (2001) 391

[99] C Avellaneda, M Berton, L Bulhoes, Solar Energy Mat. Solar Cells 92 (2008) 240

[100] Z C Orel, B Orel, Solar Ener. Mat. Solar Cells 40 (1996) 205

[101] M Li, Z Wang, S Fan, Q Zhao, G Xiong, Nuclear Instruments and Methods in Phy. Res. B 135 (1998) 535

[102] T Chaudhuri, S Phok, R Bhattacharya, Thin Solid Films 515 (2007) 6971

[103] A H Morshed, M E Moussa, S M Bedair, R Leonard, X Liu, N El-Masry, Appl. Phys. Lett. 70 (1997) 13

[104] J C Nie, Z Y Hua, R F Dou, Q Y Tu, J. Appl. Phys. 103 (2008) 054308

[105] Y Jiang, N Bahlawane , J. Alloys. Compds. 485 (2009) L52

[106] H G Lee, Y M Lee, H S Shin, C Kim, G Hong, Mat. Sci. Eng. B90 (2002) 20

[107] Y Kobayashi, Y Fujiwara, J. Alloys. Compd. 408-412 (2006) 1157

[108] B Tatar, E D Sam, K Kutla, M Urgen, J. Mater. Sci. 43 (2008) 5102

[109] C Charitidis, P Patsalas, S Logothetidis, J. Phy: Conf. series 10 (2005) 226

[110] A Siokou, S Ntais, V Copoulos, S Papaefthimiou, G Leftheriotis, P Yianoulis, Thin solid Films 514 (2006) 87

[111] P Patsalas, S Logothetidis, L Sygellou, S Kennou, Phy. Rev. B 68 (2003) 035104

[112] M Stuart, Brit, J. Appl. Phys. 1969 SER 2 Vol 2

[113] H G Lee, Y M Lee, H S Shin, C H Jung, D Youm, G W Hong, Super cond. Sci. 13 (2000) 1368

[114] P Patsalas, S Logothetidis, C Metaxa, Appl. Phys. Lett 81 (2002)466

[115] E E Khawaja, S M A Durrani, M F Al-Kuhaili, J. Phys. D: Appl. Phys. 36 (2003) 545

[116] V Matolin, J Libra, I Matolinova, V Nehasil, L Sedlacek, F Sutara, Appl. Surf. Sci. 254 (2007) 153

[117] S Debnath, M R Islam, M S R Khan, Bull. Mater. Sci. 30 (2007) 315

[118] V Fernandes, R J O Mossanek, P Schio, J J Klein, A J A de Oliveira, W A Ortiz, N Mattoso, J Varalda, W H Schreiner, M Abbate, D H Mosca, Phys. Rev. B 80 (2009) 035202

[119] M Y Chen, X T Zu, X Xiang, H L Zhang, Physica B 389 (2007) 263

[120] S Swaroop, M Kilo, A E Kossoy, I Lubomirsky, I Riess, Solid State Ionics, DOI: 10.1016/j.ssi.2007.12.006

[121] T Ami, M Suzuki, Mater. Sci. Engg. B 54 (1998) 84

[122] N Savvides, A Thorley, S Gnanarajan, A Katsaros, Thin Solid Films 388 (2001) 177

[123] B Elidrissi, M Addou, M Regragui, C Monty, A Bougrine, A Kachouane, Thin Solid Films 379 (2000) 23

[124] F Sutara, M Cabala, L Sedlacek, T Skala, M Skoda, V Matolin, K C Prince, V Chab, Thin solid Films 516 (2008) 6120

[125] C Chunlin, Y Shaoyan, L Zhikai, L Meiyong, C Noufu, Chin. Sci. Bull. 48 (2003) 1198

[126] N M Ushakov, G Y Yurkov, L V Gorobinskii, O V Popkov, I D Kosobudskii, Acta Materrialia 56 (2008) 2336

[127] A A Ansari, M A M Khan, M N Khan, S A Alrokayan, M Alhoshan, M S Alsalhi, J. Semiconductors 32 (2011) 043001

[128] K S Sivudu, D Shailaja, Mat. Lett. 61 (2007) 2167

Chapter

2

EXPERIMENTAL TECHNIQUES

Contents

2.1. Introduction

This chapter focuses mainly on the fundamentals and basic principles of the preparation techniques of nanomaterials and thin films and the characterization tools, which are used in the present investigation. The characterization techniques include structural, optical, thermal and magnetic characterization methods used to characterize the nanomaterials and nanostructures. The structural characterizations include X-ray Diffraction (XRD), Scanning Electron Microscopy (SEM), Energy Dispersive X-ray Spectroscopy (EDX) and Transmission Electron Microscopy (TEM) techniques. Optical characterizations include Diffuse Reflectance Spectroscopy (DRS), Fourier Transform IR Spectroscopy (FTIR) and Photoluminescence Spectroscopy (PL) methods. Vibrating Sample Mgnetometer (VSM) is used to investigate the magnetic properties.

2.2. Synthesis methods

Synthesis forms an essential component of nanoscience and nanotechnology. While nanomaterials have been generated by physical methods such as laser ablation, arc-discharge and evaporation, chemical methods have been proved to be more effective, as they provide better control on the size, shape and functionalization of the nanomaterials synthesized [1].

2.2.1. Chemical precipitation

Precipitation technique of rare earth compounds from aqueous solutions using suitable reagents is useful for the development of nanoparticles of oxides for various applications. Homogeneous precipitation method, which is based on acid-base reaction, is conventional for preparing functional rare earth oxides from a view point of industrial applications. Chemical precipitation of various salts (nitrates, chlorides etc.) under a fine control of pH using NaOH or NH_4OH solutions is used for synthesizing the corresponding oxide nanoparticles. Particle size of the as-precipitated material is strongly dependent on the pH of the precipitation medium and morlarity of the starting precursors. Consequently, control over the particle size can be easily achieved. The reaction and transport rates are affected by the concentration of reactants, temperature, pH of the solutions and the order in which the reagents are added to the solution and mixing. The structure and crystallinity of the particles can be influenced by the reaction rates and impurities. Particle morphology is influenced by factors such as supersaturation, nucleation and growth rates.

In the present investigation a modified version of chemical precipitation is used. The modified technique is called hydrolysis assisted precipitation method. Here the required quantity of precursor salts are dissolved in deionized water and taken in round bottom flak fitted with a Liebig's condenser. The

solution is heated to about 120 ^{0}C using a mantle heater. The solution thus vapourized is condensed in the Liebig's condenser and fall back to the round bottom flask. This hydrolysis is carried out for many hours (72 hours) to get the required size distribution. After the completion of the hydrolysis process ammonia solution is added to the solution to get precipitate. The precipitate is washed many times with deionized water and then centrifuged. Then it is heated to 100 ^{0}C to remove water and ground using agate mortar and pestle to get fine nanoparticles [2].

2.2.2. Spray pyrolysis

Spray pyrolysis is one of the relatively simple and cheap methods, which can easily be adopted for mass production of large – area coatings for industrial applications. This method has been widely used for the preparation of transparent conducting oxide films. In the present investigation, we have used the spray pyrolysis technique for the preparation of CeO_2 thin films.

Spray pyrolysis involves a thermally stimulated chemical reaction between fine droplets of different chemical species. In this technique of film preparation, a solution (usually aqueous) containing soluble salts of the number of constituents atoms of the compound is sprayed onto a preheated substrate in the form of fine droplets by a nozzle sprayer with the help of a carrier gas. Upon reaching the hot surface, these droplets undergo pyrolytic decomposition to be formed as a thin film on the substrate surface. The hot substrate provides the thermal energy for the decomposition and subsequent chemical reaction. The carrier gas may or may not play an active role in the pyrolytic reaction process.

According to the previous studies, the decomposition process is the net result of

a. Spreading of a drop into a disc

b. Pyrolytic reaction between the decomposed reactants

c. Evaporation of the solvent

d. Repetition of the proceeding process with succeeding droplets

Consequently, the film contains overlapping discs; each corresponds to a single droplet. A schematic diagram of a typical spray pyrolysis set up is shown in figure 2.1.

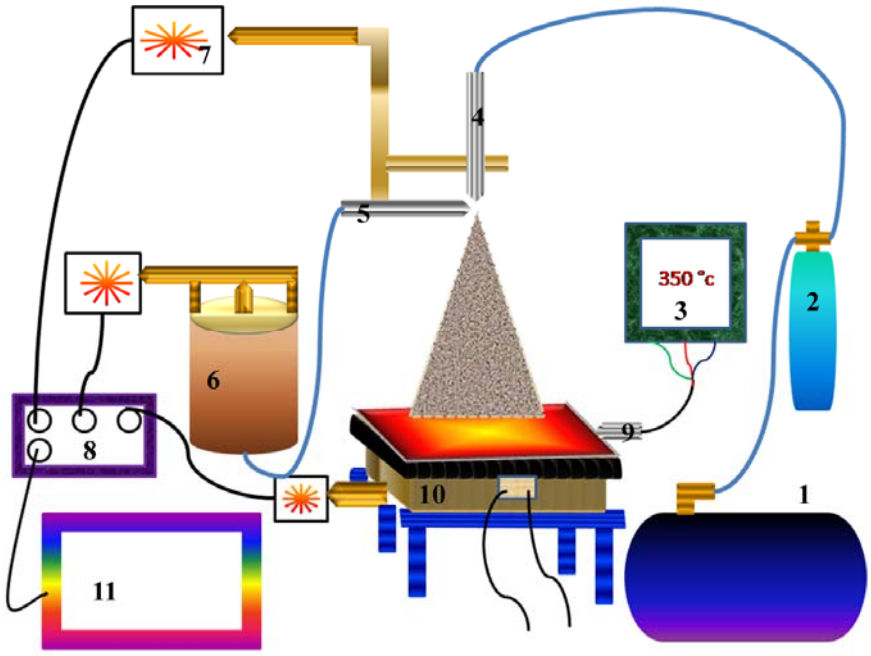

Figure 2.1: Schematic diagram of spray pyrolysis experimental setup.

The spray pyrolysis experimental setup consists of the following components.

1) Air Compressor
2) Pressure Controller
3) Temperature Controller
4) Nozzle for Air
5) Nozzle for Solution

6) Solution Container

7) Stepper Motor

8) Microprocessor Controller

9) Temperature sensor

10) Heater setup

11) Computer

Spray pyrolysis is a simple technique that has become popular owing to the number of advantages it offers over the other thin film deposition techniques. The quality of the spray deposited films depends on the deposition parameters such as the spray rate, spray interval, spray time, substrate temperature and ratio of the various constituents in the solutions. Compared to other thin film deposition techniques, pyrolytic technique has been most widely used for the deposition of semiconductor films such as zinc oxide, indium oxide and tin oxide. In comparison with other deposition techniques, this method is rather easy to use and most economical in terms of equipment cost. In a properly designed reactor with suitable adjustment of process parameters, the film deposited is highly reproducible. The spray pyrolysis technique has the following advantages [3-5]:

- It is a cost effective technique and the apparatus can be implemented in the laboratory with greater ease.
- The film production cost is quite low in comparison to the other thin film deposition techniques.
- It does not require high quality targets and vacuum at any stage.
- Large area coating and high reproducibility are possible.

- It is possible to change the useful deposition parameters such as flow rate of carrier gas, solution concentration level of the host and dopant atoms, substrate temperature, and substrate-nozzle distance, spray angle, spray rate, spray time and spray interval independently.
- The thickness of the films and rate of deposition can be easily controlled over a wide range, simply by controlling the spray parameters.

In the present investigation, the automated spray pyrolysis unit supplied by Holmarc Opto-mechatronics Ltd, Kochi, India has employed for the preparation of CeO_2 thin films. Figure 2.2 depicts the photograph of the spray pyrolysis unit. The important components of the system are discussed below.

Heater and Temperature Controller:

Resistive heating is achieved with the help of a heater that has heating coils. The heating coils are wound on a ceramic kettle. The heater is provided with proper thermal insulation (by means of glass wool) to avoid the thermal loss in the form of radiation. A stainless steel plate kept on top of the heater is used as the base for holding the substrates. A digital DTC503 temperature controller is used for monitoring the substrate temperature with the resolution of 1 °C. A Cromel-Alumel thermocouple that is kept on the surface of hot plate is used as thermal sensor. The thermocouple is placed at the optimized position in order to make sure that the measured temperature is approximately at par with that on the substrates surface.

Air Compressor:

An air compressor with the container capacity of 45 litres has been employed in the present study to supply the carrier gas. A pressure regulator that is fixed at the outlet of the container is used to control the pressure of carrier gas, which is a useful deposition parameter of spray pyrolysis technique.

The outlet of this regulator is connected to air filter to remove the oil content or the other impurities mixed with the carrier gas. The outlet of the air filter is connected with an open/close valve, with which the spraying action can be started or stopped.

Solution Container:

A teflon cylinder with a capacity of 250 ml is used as a solution container. A tube (janatics, pneumatic, 10 bar, D25j) is connected to the cylinder and the other end is connected to the spray nozzle. The solution is sprayed by the movement of a piston connected to a stepper motor and controlled by micro-controller. The spray rate is adjusted through software and can be stored for the future deposition.

Chamber:

A chamber has been designed and fabricated to cover the entire experimental setup. One side of the chamber is covered with glass doors, which can be used to operate the setup and as a see through port. All the other sides are covered with iron sheets.

Deposition process

In this deposition technique, a starting solution, containing metal precursors, is sprayed by means of a nozzle, assisted by a carrier gas, over a hot substrate. When the fine droplets arrive at the hot substrate, the compounds in the precursor decompose to become a new chemical compound in solid state, which is then deposited on the substrate surface. All other byproducts are in the gaseous form, and are taken away by the carrier gas. In the present investigation, CeO_2 thin films of various thicknesses were deposited on soda lime glass substrates using the spray pyrolysis technique at a substrate temperature of 623 K.

The selection of the substrate and methods adopted for cleaning the substrate surface are very important in the formation of thin films with reproducible properties. Selection of substrates determines the surface properties and these are directly or indirectly related to the film formation stages of adatom, nucleation, interface formation and film growth. The material, nature, size and surface roughness and cleanliness of the substrate surface play an important role on the thin film properties such as adhesion, pin hole density, porosity, film microstructure, morphology and mechanical properties. A well cleaned substrate surface is a pre-requisite for the preparation of films with reproducible properties. In this study micro glass slides were chosen as substrates since a film deposited on the glass substrate shows less dependence of interfacial energy on the film orientation and hence smooth nucleation for the measurement of optical and electrical properties.

In general, the contaminants present on the substrate surface can be broadly classified under two headings such as organic and inorganic. Organic contaminants can be easily removed by emulsifying the substrate surface with washing solutions. However, a direct mechanical approach is required for the removal of inorganic contaminants particularly when they are in particle form. A number of procedures [4] are available for the substrate cleaning such as immersing in solvents, ultrasonic cleaning, cleaning with solvents, cleaning by heating and irradiation, spray cleaning, electrical discharge etc. Amongst the different procedures, ultrasonic cleaning is one of the best methods. In this method, ultrasonic waves with high accelerating force separate the contaminating particles that are stuck to the substrate surface. The systematic procedures adopted in this study for cleaning the substrates are outlined in the following steps.

Step 1 : Initially, the substrates were wiped with acetone and cotton to remove the visible contamination such as air dust.

Step 2 : Cleaned thoroughly with industrial detergent in running water.

Step 3 : Later, the substrates were subjected to ultrasonic agitation for 30 minutes followed by washing with double distilled water.

Step 4 : Then the substrates were dried in a hot air oven before mounting them on the substrate holder.

2.2.3. Synthesis of polymer/CeO_2 nanocomposites

CeO_2 nanoparticles are prepared using hydrolysis assisted chemical precipitation method as described in 2.2.1. Polymer/ CeO_2 nanocomposites are prepared by adding 10 wt % of CeO_2 powder into four different polymer solutions (polyvinylidene fluoride (PVDF), polyvinyl alcohol (PVA), polymethyl methaacrylate (PMMA) and polystyrene (PS)) in respective solvents (10 % w/v). The mixtures are then stirred for 2 hours then sonicated for 10 min [6].

2.3. Structural Characterization

Characterization of nanomaterials and nanostructures has been largely based on the surface analysis techniques and conventional characterization methods developed for bulk materials. These include: XRD, TEM, SEM, EDS and FT-IR. To understand a nanomaterial we must, first, learn about its structure, i.e., determine the types of atoms that constitute its building blocks and how these atoms are arranged relative to each other.

2.3.1. X-ray Diffraction

X-ray diffractometry (XRD) is a powerful technique for the investigation of crystalline matter. Information concerning phase composition,

grain size, internal lattice strain, preferred crystal orientation etc. can be obtained. In this work, x-ray diffraction has been used as a method for grain size calculation and strain determination.

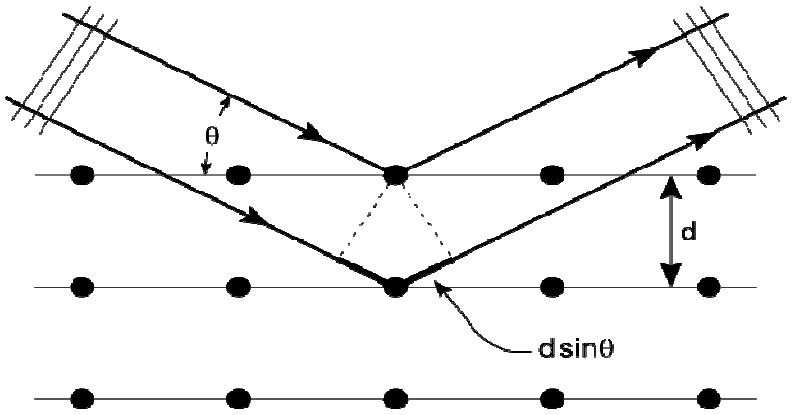

Figure 2.2: X-ray diffraction from crystal planes.

As the sample is exposed to a beam of x-rays each atom is the source of a coherently scattered wave that will interfere in a constructive or destructive way with the waves from other surrounding atoms. This is shown schematically in figure 2.2. The Bragg law describes the path difference. The condition for constructive reflection of the incident radiation is [7]

$$2d_{(hkl)} \sin\theta = n\lambda \qquad (1)$$

where $d_{(hkl)}$ is the distance between atom planes, θ is the angle of incidence, λ is the wavelength of the x-ray, and n is the order of the reflection. The Bragg law is a consequence of the periodicity of the space lattice. This law does not refer to the arrangement or basis of atoms associated with each lattice point. The composition of the basis determines the relative intensity of the various orders "n" of diffraction from given set of parallel planes. Bragg reflection can occur only for wavelengths $\lambda \leq 2d$, since $(n\lambda/2d) \leq 1$. Further,

Scherrrer's formula is commonly used for determining the mean grain size, D, in a crystalline material. This quantity is given by

$$D = \frac{0.9\lambda}{\beta \cos\theta} \qquad (2)$$

where D is the average dimension of the crystallites normal to the reflecting planes, β is the crystallite-size breadth defined by $\beta^2 = B^2 - b^2$ in which B is the FWHM of observed peak, b is the instrumental factor. The Scherrer method may be used when the effect of internal strain can be neglected. The lattice constant 'a' is calculated using the following equation:

$$\frac{1}{d^2_{(hkl)}} = \left[\frac{h^2 + k^2 + k^2}{a^2}\right] \qquad (3)$$

2.3.2. Transmission Electron Microscopy (TEM)

TEM is an imaging technique whereby a beam of electrons is focused onto a specimen causing an enlarged version to appear on a fluorescent screen or layer of photographic film or to be detected by a CCD camera. Electrons are generated by a process known as thermionic discharge in the same manner as the cathode ray tube, or by field emission; they are then accelerated by an electric field and focused by electric and magnetic fields on to the sample. The electrons can be focused onto the sample providing a resolution far better than possible with light microscopes, and with improved depth of vision. Details of the sample can be enhanced with light microscopy by the use of stains. Similarly, with electron microscopy, compounds of heavy metals such as osmium, lead or uranium can be used to selectively deposit in the sample to enhance structural details, the electrons that remain in the beam can be detected using a photographic film, or fluorescent screen. Figure 2.3 shows schematic diagram of TEM.

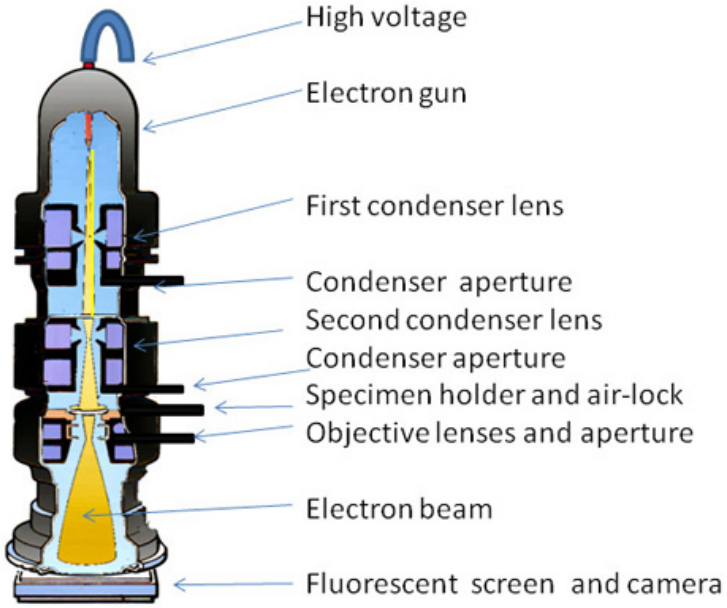

Figure 2.3: Schematic diagram of TEM

A particle of mass m moving with a large velocity v behaves like a wave of wavelength $\lambda = h/mv$. This wave nature of the particle is used in the construction of an electron microscope. An electron microscope is similar to that of an optical microscope. In an electron microscope, a beam of electrons is used in the place of ordinary light and focusing is done by electric and magnetic fields.

Electron beams are not only capable of providing crystallographic information about nanoparticle surfaces but also can be used to produce images of the surface, and they play this role in electron microscopes. In a transmission electron microscope, the electrons from a source such as an electron gun enter the sample, are scattered as they pass through it, are focused by an objective lens, are amplified by a magnifying lens, and finally produce the desired image. A TEM can form images by the use of selected area electron diffraction (SAED) aperture located between the objective and projector lenses. The main

part of the electron beam transmitted by the sample consists of electrons that have not undergone any scattering. The beam also contains electrons that have lost energy through inelastic scattering with no deviation of their path, and electrons that have been reflected by various (hkl) crystallographic planes. To produce what is called a bright-field image, the aperture is inserted so that it allows only the main undedicated transmitted electron beam to pass. The bright field image is observed at the detector or viewing screen. If the aperture is positioned to select only one of the beams reflected from a particular (hkl) plane, it generates a dark –field image at the viewing screen [8].

2.3.3. Scanning Electron Microscopy (SEM)

Scanning electron microscopy (SEM) is often used for surface analysis and imaging. The sample is hit by a beam of electrons, from a field emission or thermionic cathode, accelerated by a voltage of 1 to 30 kV. When the beam of electrons interacts with the surface of the sample, secondary electrons, back scattered electrons, and Auger electrons can be collected using different detectors; as shown in figure 2.4.

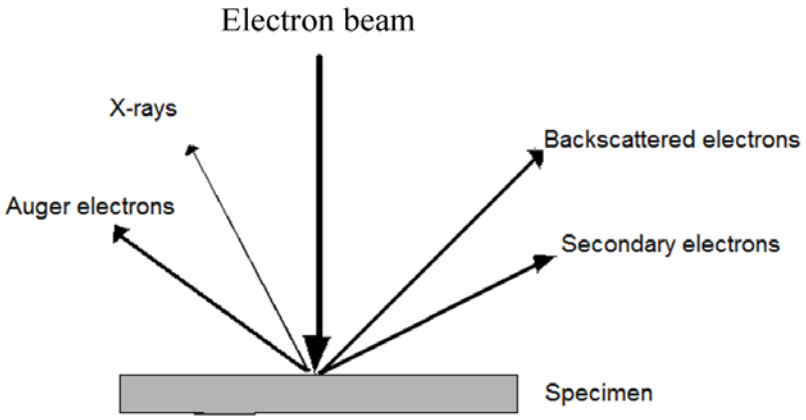

Figure.2.4: Schematic diagram of electron beam interaction with material

Scanning electron microscopy can provide information on surface morphology. Using additional equipment, for example an energy dispersive spectrometer (EDS-detector), one can obtain elemental information and produce elemental maps of the sample surface. Upon impinging on the specimen, there is an interaction between the atoms and electrons in the sample. This interaction causes various signals to be generated and the most commonly used signals are those from secondary and elastic back-scattered electrons. The secondary electrons are electrons of very low energy and thus contain information of only a few angstroms deep on the surface of the layer. These electrons are then detected by a detector consisting of a scintillator-photomultiplier combination, which in turn through the system electronics drive the cathode ray tube. These images are the ones commonly used in SEM to interpret the morphology of a sample [9].

2.3.4. Energy-Dispersive X-ray spectroscopy (EDX)

The chemical composition of the grown layers plays an important role in deciding the electrical and optical properties. A small change in composition from the desired concentration of elements can lead to drastic variations in the electro-optical properties of thin films. In the present investigation, Energy dispersive analysis of X-rays technique is employed to analyze the composition of nanoparticles and films.

In EDX, high energy (>200 kV) electrons transmitted through sample sections allow atomic resolution imaging as well as nanometer scale elemental identification via characteristic X-ray generation. Its characterization capability is mainly related to the fundamental principle that each element of the periodic table has a unique atomic structure allowing X-rays that are characteristic of an element's atomic structure to be uniquely distinguished from each other.

The basic principle involved in EDX is that X-rays are produced as a result of the ionization of an atom by high-energy radiation wherein an inner shell electron is removed. When the ionized atom returns to its ground state, an electron from a higher energy outer shell fills the vacant inner shell and, in the process, an amount of energy equal to the potential energy difference between the two shells is released. This excess energy, which is unique for every atomic transition, will be emitted by the atom either as an X-ray photon or will be self absorbed and emitted as an Auger electron. For example, if the K-shell is ionized and the ejected K-shell electron is replaced by an electron from the L-shell, the emitted X-ray is labeled as a characteristic $K\alpha_1$ line. The hole that exists in the L-shell will be filled by an electron from a higher shell, say the M-shell, if one exists. This M-L transition may result in the emission of another X-ray, labeled according to one of the many M-L transitions possible. The cascade of transitions will continue until the last shell is reached. Thus, in an atom with many shells, many emissions can result from a single primary ionization.

The qualitative and quantitative analysis for all elements from carbon onwards can be done and the detection limits typically 0.1 – 100 wt% for most elements. Further the multi- element quantitative analysis of materials and features $\geq$ 2 μm are realizable using modern EDX. Based on the practical observation the energy dispersive X-ray spectrometry in the SEM has limits of approximately 0.1 wt% [9].

2.3.5. Fourier Transform Infra-red Spectroscopy (FTIR)

Molecules and crystals can be thought of as systems of balls (atoms or ions) connected by springs (chemical bonds). These systems can be set into vibration, and vibrate with frequencies determined by the mass of the balls

(atomic weight) and by the stiffness of the spring (bond-strength). The mechanical molecular and crystal vibrations are at very high frequencies, which is in the infra red regions of the electromagnetic spectrum.

Vibrational spectroscopy involves photons that induce transition between vibrational states in molecules and solids, typically in the (IR) frequency range. The energy gaps of many semiconductors are in this same frequency region and can be studied by IR techniques.

If the impinging IR energy is in resonance with the energy of the chemical bond in the sample the intensity of the beam is measured before and after it interacts with the sample. The incident radiation can be detected in transmission or reflection experiments. The intensity is then plotted as a function of frequency in the IR spectrum. From the characteristic peaks, different functional groups present in the compound can be identified [10].

2.4. Optical characterization

Optical spectroscopy has been widely used for the characterization on nanomaterials, and the techniques can be generally categorized into two groups: absorption and emission spectroscopy and vibrational spectroscopy. The former determines the electronic structures of atoms, ions, molecules or crystals through exciting electrons from the ground to excited states (absorption) and relaxing from the excited to ground states (emission). The vibrational techniques may be summarized as involving the interactions of photons with species in a sample via vibrational excitation or de excitation. The vibrational frequencies provide the information of chemical bonds in the detecting samples.

Semiconductors are distinguished by the nature and mechanisms of the processes that bring about the absorption or emission of light. Incident light with photon energies less than the band gap energy Eg passes through the sample without absorption, and higher-energy photons can raise electrons from

the valence band to the conduction band, leaving behind holes in the valence band. The technique of photoluminescence excitation has become a standard one for obtaining information on the nature of nanostructures such as quantum dots. One advantage of these techniques is that the optical spectroscopy systems are inexpensive and have fast data acquisition.

2.4.1. UV-VIS absorption Spectroscopy

Optical absorption studies are necessary for the determination of the band structure of semiconductors and these measurements are non-destructive. This technique involves the interaction of light with matter in which the photo-induced electronic transitions can occur between different bands by the absorption or emission of radiation at a characteristic frequency. The basic principle of optical spectroscopy is that electromagnetic radiations from a source are dispersed and this dispersed light is passed through the sample under study. A part of the transmitted radiation is studied as a function of incident wavelength with a suitable detecting system. The optical spectrometer consists of three main components, a light source with monochromator, sample and reference port and the detecting system. There are various types of sources, monochromators, and sample containers and detecting units, the choice of which depends on the materials under study [11]

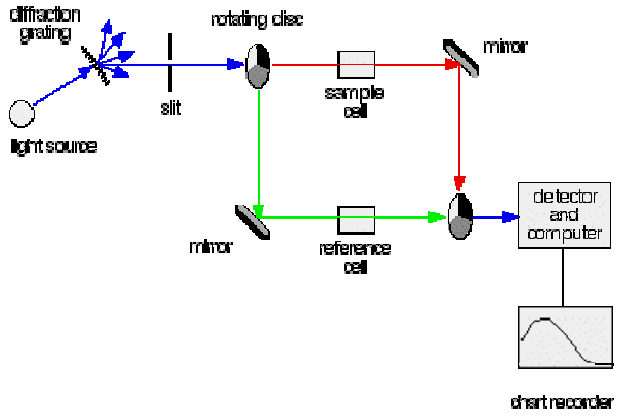

Figure.2.5: Double beam UV-visible spectrometer

UV-Vis-NIR radiation is a form of energy and a fruitful part of electromagnetic radiation spectrum ranging from 300 to 1100 nm. When a beam of UV-Vis-NIR radiation strikes any object it can be absorbed (A), transmitted (T), scattered (S) and reflected (R). Since some of the energy of the incident photon is retained in the molecule (or is lost by a non – radiative process such as collision with another molecule) the emitted photon has less energy and hence a longer wavelength than the absorbed photon. Surface roughness, micro cracks, incorporated particulates and impurities act as sources of scattering. Since the scattering effect is negligibly small, it is generally omitted. Then we can emphasize the familiar relation as R+T+A=100%. Absorption of light by different materials can induce various types of transitions such as band to band, between sub-bands, between impurity levels and bands, interactions with free carriers in with a band, resonance due to vibrational state of lattice and impurities. These lead to the appearance of bands or absorption peaks in the absorption spectra.

A schematic diagram of a spectrophotometer is shown in figure 2.5. The transmissions of the thin films were recorded using Shimadzu UV-1700 Spectrophotometer in the wavelength range 300 to 1100 nm in the present studies.

2.4.2. Diffuse Reflectance Spectroscopy (DRS)

This technique is readily applicable for the characterization of nanostructures and nanomaterials. The characteristic lines observed in the reflection spectra of nearly isolated atoms and ions due to transitions between quantum levels are extremely sharp. As a result, their wavelengths or photon energies can be determined with great accuracy**.** The lines are characteristic of a particular atom or ion and can be used for identification purposes. In solids, the large degeneracy of the atomic levels is split by interactions into quasi-

continuous bands (valence and conduction bands), and makes their optical spectra rather broad. The energy difference between the highest lying valence (the highest occupied molecular orbital, HOMO) and the lowest lying conduction (the lowest unoccupied molecular orbital, LUMO) bands is designated as the fundamental gap.

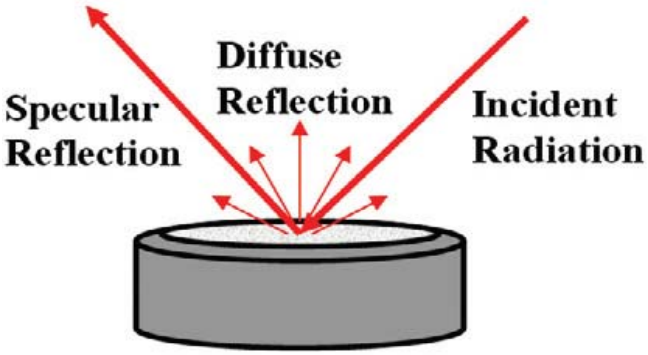

Figure 2.6: Schematic diagram showing the diffuse reflection.

Figure 2.6 shows a schematic diagram of processes taking place when a beam of radiation incident on a solid sample. In a diffuse reflectance spectrum, the ratio of the light scattered from a thick layer of sample and an ideal non-absorbing reference sample is measured as a function of wavelength. The relation between the diffuse reflectance of the sample (Rα), absorption (K) and scattering (S) coefficients are related by the Schuster-Kubelka-Munk (SKM) remission function.

The absorption coefficients of the samples were calculated from Munk-Kubleka relation, which is useful for compounds that are difficult to analyze in transmission mode [12].

$$\frac{k}{s} = \frac{(1-R_\infty)^2}{2R_\infty} \qquad (4)$$

R_∞ is the diffuse reflectivity from an infinitely thick layer of powder, k the absorption coefficient and s the scattering factor independent of wavelength for particle sizes larger than the wavelength of light.

The relation $(\alpha h\nu) = A\left(h\nu - E_g\right)^n$ remains valid if the coefficient α is replaced by k/s. Where E_g is the band gap, ν is the frequency, A is a constant and n can have values 1/2, 3/2, 2 and 3 depending up on the mode of inter band transition i.e. direct allowed, direct forbidden, indirect allowed and indirect forbidden transition respectively. The direct optical band gap E_g is determined by extrapolating the curve $(h\nu k/s)^2$ vs. $(h\nu)$ to zero absorption (Tauc plot). Similarly plotting $(h\nu k/s)^{1/2}$ as a function of photon energy $(h\nu)$, and extrapolating the linear portion of the curve to absorption equal to zero gives the value of indirect band gap energy.

The study of the optical properties of solid is a powerful tool in understanding the electronic and atomic structure of solids. Measurement of optical constants, the refractive index (n), the extinction coefficient (k) and the absorption coefficient (α) has crucial importance from the point of view of basic and applied research. This is because, these constants are determined by the structure and bonding of atoms in the solid. Hence the measurement of these quantities as a function of wavelength can give valuable information regarding the structure and bonding. Moreover any application of the materials in optics or opto-electronics, n & k are the most important quantities.

Commonly used methods for measuring the optical constants are spectroscopic ellipsometry, simultaneous measurement of transmission and reflection, and measurement of reflection/transmission only. The spectroscopic ellipsometry offers a precise determination of optical constants, particularly at photon energies well above the fundamental edge. But the method is applicable

only in the region of wavelength where polarizers and analyzers are available. Moreover elaborate mathematical calculation is needed. One advantage of this method is that the material need not be transparent to the radiation used. Simultaneous measurement of transmission and reflection is the most used method for the measurement of the optical constants. This method is applicable in any region of the spectrum if suitable light source and detectors are available and also if the material is fairly transparent. In the highly absorbing region of the spectrum of the material, reflectivity measurements are the only available method.

Intrinsic optical absorption of a single photon across the band gap is the dominant optical absorption process in a semiconductor. When the energy of the incident photon (hν) is larger than the band gap energy the excitation of electrons from the valence band to the empty states of the conduction band occurs. The light passing through the material is then absorbed and the number of electron hole pairs generated depends on the number of incident photons $S_0(\nu)$ (per unit area, unit time and unit energy). The frequency ν is related to the wavelength - by the relation, λ= c/ν, where c is the velocity of light. The photon flux $S(x,\nu)$ decreases exponentially inside the crystal according to the relation

$$S(x,v) = S_0 \exp(-\alpha x) \qquad (5)$$

where, the absorption coefficient α, (α(ν) = 4πkν/c) is determined by the absorption process in semiconductors and k is the extinction coefficient. For the parabolic band structure, the relation between the absorption coefficient (α) and the band gap of the material is given by

$$\alpha h\nu = A(h\nu - E_g)^n \qquad (6)$$

where, n = 1/2 for allowed direct transitions, n = 2 for allowed indirect transitions, n = 3 for forbidden indirect transitions and n = 3/2 for forbidden direct transitions.

A is the parameter which depends on the transition probability. The absorption coefficient can be deduced from the absorption or transmission spectra using the relation

$$I = I_0 e^{-\alpha t} \quad (7)$$

where, I is the transmitted intensity and I_0 is the incident intensity of the light and t is the thickness of the film. The absorption coefficient α is calculated from the relation [5]

$$T = (1 - R)exp(-\alpha t) \quad (8)$$

where T is the transmittance, R is the reflectance and t is the film thickness. In the case of direct transition, from equation, $(\alpha h\nu)^2$ will show a linear dependence on the photon energy ($h\nu$). A plot of $(\alpha h\nu)^2$ against $h\nu$ will be a straight line and the intercept on energy axis at $(\alpha h\nu)^2$ equal to zero will give the band gap energy.

2.4.3. Photoluminescence Spectroscopy (PL)

Luminescence refers to the emission of light by a material through any process other than black body radiation. The emission of light can result from a variety of stimulations. In PL, one measures physical and chemical properties of materials by using photons to induce excited electronic states in the material system and analyzing the optical emission as these states relax. Typically light is directed onto the sample for excitation, and the emitted luminescence is collected by a lens and passed through an optical spectrometer onto a photon detector. The spectral distribution and time dependence of the emission are related to electronic transition probabilities within the sample and can be used to provide qualitative and sometimes, quantitative information about chemical composition, structure, impurities, kinetic process and energy transfer.

Sensitivity is one of the strengths of the PL technique, allowing very small quantities or low concentrations of material to be analyzed.

In PL, a material gains energy by absorbing photon at some wavelength by promoting an electron from a low to a higher energy level. This may be described as making a transition from the ground state to an excited state of an atom or molecule, or from the valence band to conduction band of a semiconductor crystal. The system then undergoes a non-radiative internal relaxation involving interaction with crystalline or molecular vibrational and rotational modes, and the excited electrons move to a more stable excited level, such as bottom of the conduction band or lowest vibrational molecular state. After a characteristic lifetime in the excited state, electron will return to the ground state. In the luminescent materials some or all of the energy released during this final transition is in the form of light. The wavelength of the emitted light is longer than that of the incident light [13].

Photoluminescence study is one of the techniques widely exploited by the researchers to probe the native defect states in the photoluminescent materials. The PL is a complementary technique to the absorption spectra. The emission spectrum contains "fingerprint"- type peaks related to the energy of each excited level and can be used as a sensitive probe to find impurities and other defects in semiconductors.

Uses:

- To determine the band gap energy and/or the wavelength of maximum gain
- To determine the composition of ternary or quaternary layers
- To determine impurity levels
- To investigate recombination mechanisms

Limitations:

- Identification of impurity and defect states depends on their optical property
- Although PL is a very sensitive probe of radiative levels, one must rely on secondary evidence to study the states that couple weakly with light
- Materials with poor radiative efficiency, such as low quality indirect band gap semiconductors are difficult to be studied through ordinary PL.

2.5. Thermal characterization

2.5.1. Thermo Gravimetric Analysis (TGA)

TGA is a technique widely used for determining the organic or inorganic content of various materials. Its basic rule of function is the high precision measurement of weight gain/loss with increasing temperature under inert or reactive atmospheres. Each weight change corresponds to physical (crystallization, phase transformation) or chemical (oxidation, reduction, reaction) processes that take place by increasing the temperature. The sample is placed into platinum or alumina pan and along with an empty or standard pan. Both the pans are placed onto two high precision balances inside a high temperature oven.

The substance is subjected to a programmed heating and cooling, it normally undergoes physical and chemical or mechanical changes. The gain or loss in weight of a sample as a function of temperature is measured by thermogravimetry (TG). It is very useful technique for the study of solid-gas systems [14].

2.6. Magnetic Characterization

2.6.1. Vibrating Sample Magnetometer (VSM)

The vibrating sample magnetometer (VSM) has become a widely used instrument for determining magnetic properties of a large variety of materials: diamagnetic, paramagnetic, ferromagnetic and anti-ferromagnetic. This experimental technique was invented in 1956 by Simon Foner, a scientist of the MIT. A vibrating sample magnetometer (VSM) operates on Faraday's Law of induction, which tells us that a changing magnetic field will produce an electric field. This electric field can be measured and provides information about the changing magnetic field. A VSM is used to measure the magnetic behavior of magnetic materials. Using VSM the hysteresis loop parameters namely saturation magnetization (Ms), coercive field (Hc), remanence magnetization (Mr) and squareness ratio (Mr/Ms) can be derived. In a VSM, the sample to be studied is placed in a constant magnetic field. If the sample is magnetic, this constant magnetic field will magnetize the sample by aligning the magnetic domains or the individual magnetic spins, with the field. The stronger the constant field, the larger the magnetization. The magnetic dipole moment of the sample will create a magnetic field around the sample, sometimes called the magnetic stray field. As the sample is moved up and down, this magnetic stray field change as a function of time and can be sensed by as set of pickup coils. A transducer converts a sinusoidal ac drive signal provided by a circuit located in the console into a sinusoidal vertical vibration of the sample rod and the sample is thus made to undergo a sinusoidal motion in a uniform magnetic field. Coils mounted on the pole pieces of the magnet pick up the signal resulting from the sample motion. The alternating magnetic field will cause an electric field in the pickup coil as according to Faradays law of induction, the current will be proportional to the magnetization of the sample. The greater the magnetization the greater is the induced current. The induction current is amplified by a trans-

impedance amplifier and a lock–in amplifier. The various components are interfaced via a computer.

Principle of vsm:

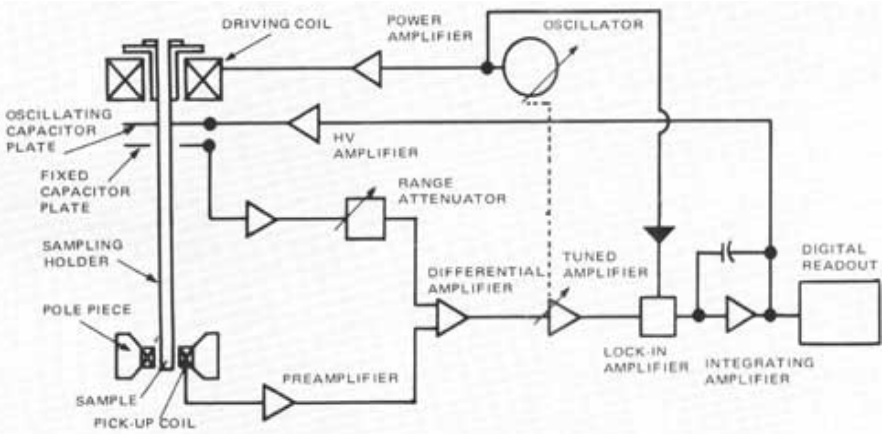

Figure.2.7: Block diagram of vibrating sample magnetometer.

Figure 2.7 shows the schematic diagram of a VSM set up. The sample is fixed to a small sample holder located at the end of a sample rod mounted in a electromechanical transducer. The transducer is driven by a power amplifier which itself is driven by an oscillator at a frequency of 90 Hertz. So, the sample vibrates along the Z axis perpendicular to the magnetizing field. The latter induced a signal in the pick-up coil system that is fed to a differential amplifier. The output of the differential amplifier is subsequently fed into a tuned amplifier and an internal lock-in amplifier that receives a reference signal supplied by the oscillator. The output of this lock-in amplifier, or the output of the magnetometer itself, is a DC signal proportional to the magnetic moment of the sample being studied. The electromechanical transducer can move along X, Y and Z directions in order to find the saddle point (which Calibration of the vibrating sample magnetometer is done by measuring the signal of a pure Ni standard of known the saturation magnetic moment placed in the saddle point.

Using a vibrating sample magnetometer one can measure the DC magnetic moment as a function of temperature, magnetic field, angle and time. So, it allows performing susceptibility and magnetization studies. Some of the most common measurements done are: hysteresis loops, susceptibility or saturation magnetization as a function of temperature (thermomagnetic analysis), magnetization curves as a function of angle (anisotropy), and magnetization as a function of time [15].

In the present studies, Lakeshore (USA) model 7404 vibrating sample magnetometer is used to determine the ferromagnetism induced in the sample and coercivity of the sample at different concentration and annealing temperature.

References

[1] C N R Rao, S R C Vivekchand, K Biswas, A Govindaraj, Synthesis of inorganic nanomaterials, Dalton Trans. (2007) 3728

[2] A Chandra Bose, P Balaya, P Thangadurai, S Ramasamy, J. Phy. Chem. Solids 64 (2003) 659

[3] H L Hartnagel, A L Dawar, A K Jain, C Jagadish, Semiconducting Transparent Thin Films, Institute of Physics Publishing Ltd (1995)

[4] L I Maissel, M H Francombe, An Introduction to Thin Films, Gordon and Breach, New York (1973)

[5] K L Chopra, S R Das, Thin Film Solar Cells, Plenum Press, New York (1983)

[6] P P Jeeju, A M Sajimol, V G Sreevalsa, S J Varma, S Jayalekshmi, Polym. Int. 60 (2011) 1263

[7] B D Cullity, Elements of X-ray Diffraction, Addition-Wesley, Reading, MA (1978)

[8] P E J Flewit, R K Wild, Physical methods for material characterization, Second edition, IOP Publishing, London (2003)

[9] D K Schroder, Semiconductor material and device characterization, second edition, John Wiley & Sons, New York (1998)

[10] C N R Rao, UV–Visible Spectroscopy Chemical applications, Second edition, Butterworth Co Publishers, London (1967)

[11] H H Willard, L L Merret Jr., J D Dean, Instrumental Methods of Analysis, Affiliated East-West Press, New Delhi (1965)

[12] L Djellala, A Bougueliab, H M Kadi, M Trarib, Sol. Ener. Mater. Solar Cells 92 (2008) 594

[13] K Nakamoto, Infrared and Raman Spectra of Inorganic and Coordination Compounds: part-A; Theory and Application In Inorganic chemistry 5th edn., John Wiley and sons, New York (1997)

[14] R K Krishnan & A Banerjee, Rev. Sci. Instrum. 70 (1995) 85

Chapter 3

SYNTHESIS, STRUCTURAL AND OPTICAL CHARACTERIZATION OF CERIUM OXIDE NANOCRYSTALS

Contents

3.1. Introduction

Ceria is a rare earth oxide that has been attracting a great deal of interest due to its unique properties and applications in various fields including catalysis, semiconductor industry, solid oxide fuel cells etc. [1]. It has a fluorite cubic structure with a lattice constant of 0.5411 nm at room temperature, matching closely to silicon (0.5431 nm). It has very high chemical and thermal stability even at high temperature, which is essential for the applications like SOI (silicon on insulator) structure. The dielectric constant of bulk CeO_2 is around 26 which makes it a promising material for applications in high density capacitor devices with small dimensions [2]. Preparation of cerium oxide powders is by no means a new research subject; however, practical methods are still needed for synthesizing high quality ultrafine powders with required characteristics in terms of their size, uniformity, morphology and crystallinity. Recently, several methods have been developed to synthesize nanoceria powder, including thermal hydrolysis, co-precipitation process, combustion method, micro emulsion technique etc. In all these, some special reacting

conditions, such as high temperature, high pressure, capping agents, expensive or toxic solvents etc. have been involved. The large scale production of powders needs to be economically feasible and should not be more complex. So compared to these methods, precipitation is more attractive due to cheap salt precursors and simple operation [3]. The solution based routes have been developed as the most important strategies, with advantages of low temperatures, simple apparatus and easy control. The hydrolysis behavior of cerium gives homogeneous compositions, tunable shapes and uniform sizes. The preparation based on liquid-phase synthesis in aqueous and non aqueous media gives direct precipitation of hydrated ceria from cerium (III) and cerium (1V) salts in strongly basic solutions. Most of the advanced performances of CeO_2 generally appear at small size in particular less than 10 nm, since in that regime the distinct properties are strongly size-dependent and would show significant quantum size effect. Therefore, the priority in tailoring electronic structures for performance improvements is to find the methodologies that can be convenient in getting monodispersed CeO_2 nanoparticles with tunable sizes. CeO_2 nanoparticle growth dynamics is governed by the reaction time, reaction temperature and molar ratio of reactants. In this chapter the realization of synthesis of an environmentally friendly and economically efficient way for the controlled ceria nanoparticles through aqueous-phase synthesis method is described.

3.2. Experimental techniques

3.2.1. Synthesis of cerium oxide

Cerium oxide nanocrystalline powder samples were prepared by hydrolysis assisted precipitation method. 0.1M solution of cerium chloride ($CeCl_3.7H_2O$) was taken in a flask fitted with a Liebig's condenser. The

solution was heated at 120 ^{0}C in an electric oven and evaporated solution was condensed back to the flask by the reflux condenser. This process of hydrolysis was carried out for 72 hours. An appropriate amount of ammonium hydroxide was added to the hydrolyzed solution and the obtained precipitate was washed many times with doubly distilled water to remove the remaining ammonia solution and then dried at 100 ^{0}C for 1 h [4, 5]. The process can be expressed by the following chemical equations:

$$CeCl_3+2H_2O \rightarrow Ce(OH)_2Cl+2HCl$$

$$Ce(OH)_2Cl+NH_4OH\ (aq) \rightarrow CeO_2+H_2O+NH_4Cl$$

3.2.2. Characterizations

XRD investigations were carried out for the as-prepared and annealed samples prepared under the optimum conditions, using a Rigaku Ultima-III X-Ray Diffractometer using Cu Kα_1 radiation in the 2θ range from 20^0 to 80^0 in steps of 0.03^0. JEOL JEM-2010 was used to record the transmission electron micrograms (TEM). FT-IR spectra of the samples were recorded using Perkin Elmer FT-IR spectrometer. UV-Vis Diffuse Reflectance Spectra were recorded using JASCO V570 UV-VIS-NIR Spectrometer. Photoluminescence (PL) measurements were carried out using a luminescence spectrometer (Jobin Yvon Flourimeter) at room temperature.

3.3. Results and discussion

Hydrolysis refers to those reactions of metallic ions with water that liberate protons and produce hydroxide or oxide solids. The rate of cerium oxide precipitation will critically depend on the reaction temperature, reaction time and concentration of precursors. The effect of reaction temperature on size distribution and morphology of precipitants can be ascribed to the effect of

reaction temperature on the precipitation kinetics including nucleation and growth rate. Both nucleation and growth rate are slow at low temperature, but nucleation rate is higher than the growth rate, so it facilitate to form smaller particles. However, growth rate is higher than nucleation rate at high temperature, thereby the particle becomes larger. The size and size distribution of particles vary significantly with the type of reagents used in the synthesis. The optimum conditions for the preparation of cerium oxide nanocrystals are as follows.

Precursor concentration - 0.1M/L

Hydrolysis time - 72 hours

Hydrolysis temperature - 120 ^{0}C

The molarity, hydrolysis duration and hydrolysis temperature are optimized to the above values after many number of trials. When the molar concentration was higher than 0.1M the solution is highly viscous and therefore difficult to boil, while if it is lower, the quantity of powder produced is small. When the hydrolysis temperature is below 120 ^{0}C, it takes long time for boiling and if it is higher, the quantity of the solution decreases because of escape of water vapour without condensation in the condenser.

The XRD spectra of the as-prepared and annealed cerium oxide samples are shown in figure 3.1. The observed broad peaks in the as-prepared samples indicate the formation of cubic nanocrystalline structure of cerium oxide sample. The peaks become gradually sharper with increasing annealing temperature, indicating that the crystallinity of the as-prepared CeO_2 nanoparticles is improved by the annealing process [6, 7]. Grain size of the as-prepared and annealed samples is calculated from XRD data using Scherrer's formula [8]

$$\text{Average grain size } t_{xrd} = \frac{0.9\lambda}{\beta \cos\theta}, \qquad (1)$$

where λ is the wavelength of the incident X-rays (1.5406 Å) β is Full Width Half Maximum and θ the diffraction angle. Table 3.1 shows the variation of the grain size and lattice parameter with annealing temperature. The particle size is found to increase with increase in annealing temperature. The lattice parameter for CeO_2 fluorite structure is 5.4113 Å (JCPDS 34-0394). The lattice parameter calculated from XRD data is found to decrease with increase in annealing temperature. The increase in lattice parameter of the nanoparticles with decrease in particle size is of great importance and would strongly affect the properties of CeO_2 nanoparticles. As-prepared ceria tends to exhibit higher lattice parameters due to the presence of defects and impurities. Such defects are introduced during the sample preparation and vary according to method and reagents used [9]. Deshpande et al. [10] have studied the relationship between the crystallite size and lattice parameter of the synthesized ceria nanoparticles. They have pointed out that the variation in the lattice parameter is attributed to the lattice strain induced by the introduction of Ce^{3+} ions due to the formation of oxygen vacancies.

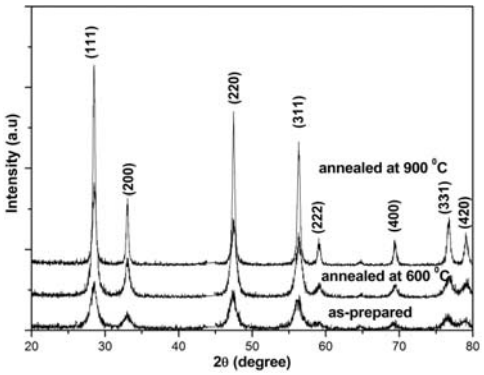

Figure 3.1: XRD patterns of the as-prepared and annealed cerium oxide.

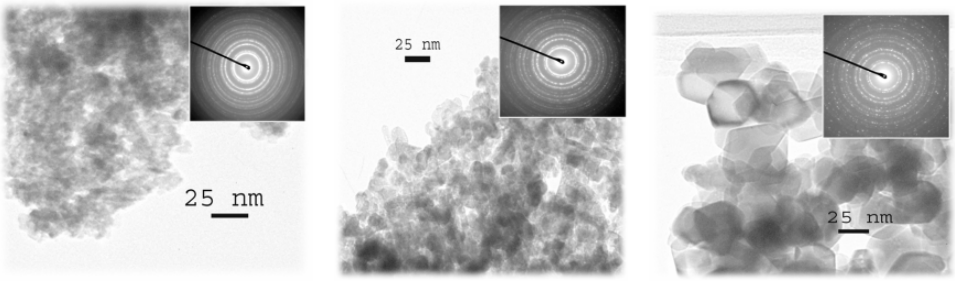

a) as-prepared b) annealed at 600 ^{0}C c) annealed at 900 ^{0}C

Figure 3.2: TEM images of cerium oxide nanoparticles

The morphology and structure of the ceria nanocrystals are investigated by TEM. Figure 3.2 shows TEM images of cerium oxide in the as-prepared and annealed states. Agglomeration of nanoparticles is a very common phenomenon that occurs because the nanoparticles tend to decrease the exposed surface in order to lower the surface energy and the smaller particle size results in stronger agglomeration [11]. The increase of particle size with increase in annealing temperature is also evident from the TEM images. Loose agglomeration of CeO_2 nanoparticles is evident in annealed samples, which suggests that particles could be separated from each other. The inset picture shows the selected area electron diffraction (SAED) pattern and Debye-Scherrer rings of the nanoparticles, which can be indexed as those of cerium oxide with the cubic fluorite structure. The ring patterns obtained in the SAED patterns confirm the polycrystalline nature and the fluorite structure [12]. The as-prepared sample consists of particles of smaller size compared with the annealed samples. The as-prepared particles are more or less spherical in shape, but in the annealed samples the particles appear in different shapes. These TEM results confirm that grains are nanometer in size and show good agreement with the XRD results.

Table 3.1: Variation of the grain size and lattice parameter with annealing temperature

sample	Grain size (nm)		Lattice parameter (Å)	
	XRD	TEM	XRD	TEM
As-prepared	9.42	10.5	5.428	5.395
At 600 ^{0}C	12.92	14.1	5.411	5.390
At 900 ^{0}C	25.84	27.0	5.410	5.350

Figure 3.3 shows EDX image of cerium oxide in the as-prepared state. EDX shows the presence of cerium and oxygen. There is no other impurity peaks in this spectrum.

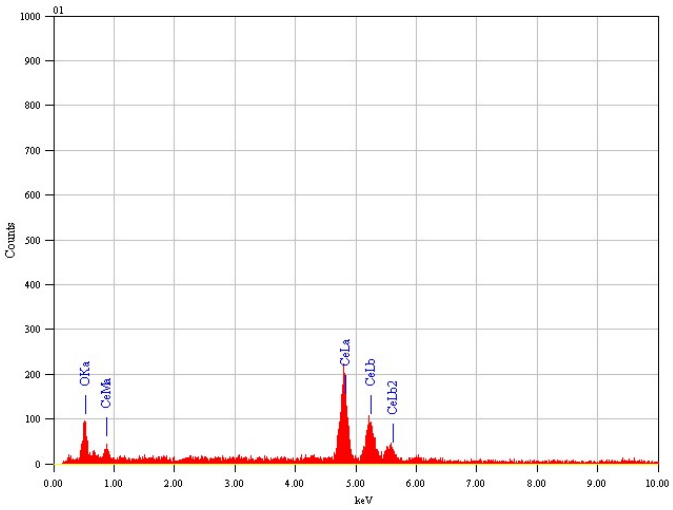

Figure 3.3: EDX of cerium oxide nanoparticles

The FT-IR spectrum in the transmission mode of the as-prepared cerium oxide sample is presented in figure 3.4. The peaks appearing in that figure are characteristic of the material structure. The broad transmission band in the first region (around 3400 cm^{-1}) is due to the presence of surface water. In ambient atmosphere the carbonation of ceria is unavoidable. This effect can be identified in the region below 1800 cm^{-1} with several peaks [13, 14]. In the range of 850 cm^{-1} to 450 cm^{-1} the prominent stretching vibration of Ce-O has been observed, which confirms the formation of CeO_2 [13-15].

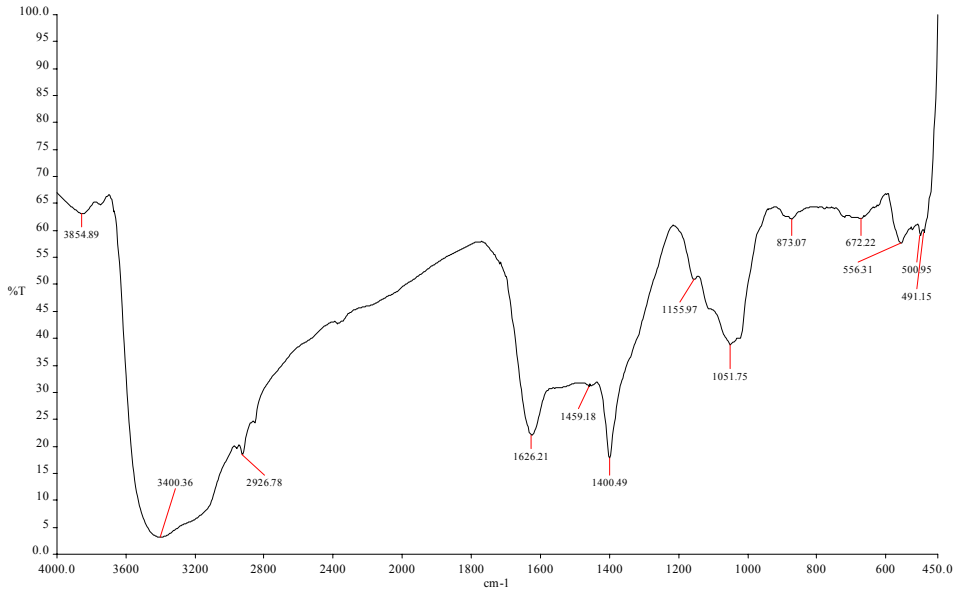

Figure 3.4: FT-IR spectrum of cerium oxide nanoparticles

Figure 3.5 shows UV –Vis diffuse reflectance spectrum of cerium oxide. Cerium oxide shows a strong absorption below 400 nm. The intensity of absorption peak is more or less the same for the as-prepared as well as the annealed samples. Due to the increase of particle size with increase in the annealing temperature, the absorption edge slightly shifts towards longer wavelength side resulting in a slight decrease in band gap energy [16, 17].

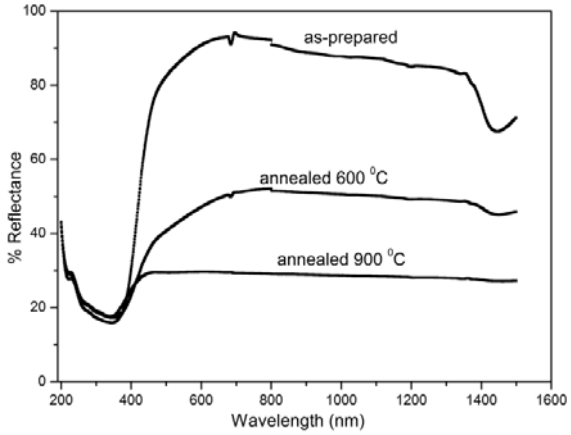

Figure 3.5: Diffuse Reflectance spectra of cerium oxide nanoparticles

The absorption coefficients of the samples were calculated from Munk-Kubleka relation, which is useful for compounds that are difficult to analyze in transmission mode [18].

$$\frac{k}{s} = \frac{(1-R_\infty)^2}{2R_\infty} \qquad (2)$$

R_∞ is the diffuse reflectivity from an infinitely thick layer of powder, k the absorption coefficient and s the scattering factor independent of wavelength for particle sizes larger than the wavelength of light.

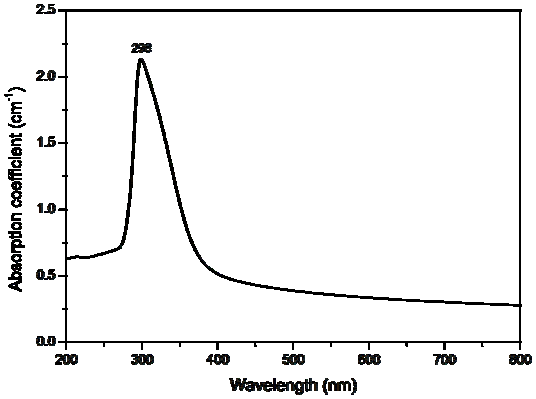

Figure 3.6: Absorption coefficient of cerium oxide nanoparticles

Figure 3.6. shows the plot of absorption coefficient with wavelength of cerium oxide nanoparticles. The absorption curve is composed of one large band, and the maximum absorption is centered on 298 nm. The absorption edge is located around 390 nm. For CeO_2, the fundamental absorption is due to a charge transfer between the filled 2p (O) orbital and the empty 4f (Ce) orbital, which corresponds to an experimental band-gap value of 3.16 eV in the present case for the unannealed sample.

The relation $(\alpha h\nu) = A(h\nu - E_g)^n$ remains valid if the coefficient α is replaced by k/s. Where E_g is the band gap, ν is the frequency, A is a constant

and n can have values 1/2, 3/2, 2 and 3 depending up on the mode of inter band transition i.e. direct allowed, direct forbidden, indirect allowed and indirect forbidden transition respectively. The direct optical band gap E_g is determined by extrapolating the curve $(h\nu k/s)^2$ vs. $(h\nu)$ to zero absorption (Tauc plot) as shown in figure 3.7 (a), which gives the value of the direct band gap E_g = 3.16 eV. Similarly plotting $(h\nu k/s)^{1/2}$ as a function of photon energy $(h\nu)$, and extrapolating the linear portion of the curve to absorption equal to zero as shown in figure 3.7 (b), which gives the value of indirect band gap energy E_g = 2.85 eV [20]. Table 3.2 shows the variation of the direct and indirect band gap energy with annealing temperature. At the outermost CeO_2 nanocrystal surface, Ce^{4+} ions coexist with Ce^{3+} iones. When the particle size decreases, the concentration of Ce^{3+} increases, thereby introducing defect states due to oxygen vacancies, which results in the decrease in the band gap [17, 21]. However in the present case the increase in particle size is brought about by thermal annealing in air and the annealing process converts majority of Ce^{3+} to Ce^{4+}, which removes the defect states and tends to increase the band gap. Therefore in the present experiment although the particle size changes in the range 10-25 nm due to annealing, the change in direct and indirect band gap energy is very small.

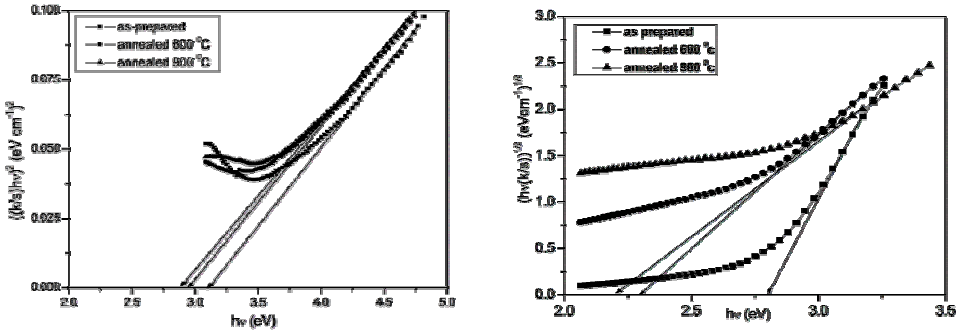

(a) Direct band gap (b) Indirect band gap

Figure 3.7: Tauc plot for cerium oxide nanoparticles

Table 3.2: Comparison of direct and indirect band gap energies of the cerium oxide nanoparticles

Samples	Direct-band gap energy (eV)	Indirect-band gap energy (eV)
As-prepared	3.16	2.85
Annealed at 600 ^{0}C	2.92	2.30
Annealed at 900 ^{0}C	2.85	2.22

The ultra violet radiation reaching the earth's atmosphere consists of UV type B sub range (UVB, 290-320 nm) and the UV type A sub range (UVA, 320-400 nm). Theses wavelengths are the major cause of skin cancers. For the filtration of UVB, nanostructured TiO_2 is being used in sunscreen cosmetic products. But for the filtration of UVA, the availability of suitable inorganic material is limited. In the field of cosmetic products [19], the need for new inorganic nontoxic materials, capable of filtering UVA radiations has increased substantially. In the present investigations with a band gap of 3.16 eV, good transparency in visible region, and no known toxicity, and strong absorption in the 300 nm-400 nm region nanostructured ceria can be a promising inorganic material for UVA filtering in sunscreen cosmetics. Thus from the present investigations it is proved that ceria-based nanomaterials are suitable candidates for application in the new generation of inorganic UV filters.

The room temperature photoluminescence (PL) spectra of CeO_2 powder sample are recorded under the excitation wavelength of 325 nm and are shown in figure 3.8. The samples are annealed at 300 ^{0}C, 600 ^{0}C, 700 ^{0}C and 900 ^{0}C and PL spectra are recorded under the same excitation wavelength and are also shown in figure 3.8. In the PL spectra emission peaks located at 371, 442, 452, 469, 483 and 494 can be clearly observed. The emission peak at 371 nm can be related to the hopping from the localized Ce 4f state to the O 2p valence band. The emission peaks ranging from 400 nm to 500 nm can be related to the hopping from different

defect levels to the O2p level [22]. These weak blue green emissions are possible due to the surface defects in the CeO_2 nanoparticles. A low intense green emission is also observed at around 530 nm, possibly due to low density of oxygen vacancies incorporated during the preparation of the CeO_2 sample [21]. The most intense peak observed at 469 nm can be related to the presence of abundant defect states, which helps in fast oxygen transportation.

From the figure 3.8, PL intensity is found to increase with increase in annealing temperature up to 600 ^{0}C and thereafter decreases. This can be understood from self trapping of excitons (STE) in nanocrystalline CeO_2. In cerium oxide, the strong coupling between lattice and electronic part of excitons would result in the STE. That is, electrons in the valence band are excited to some localized levels by absorbing incident photons and form small polarons, and holes in the valence band interact with the polarons to form STEs. On the basis of the size effect of excitons, it is assumed that the binding energy and the radiative life time of STEs are strongly related to grain size. The spatial overlap

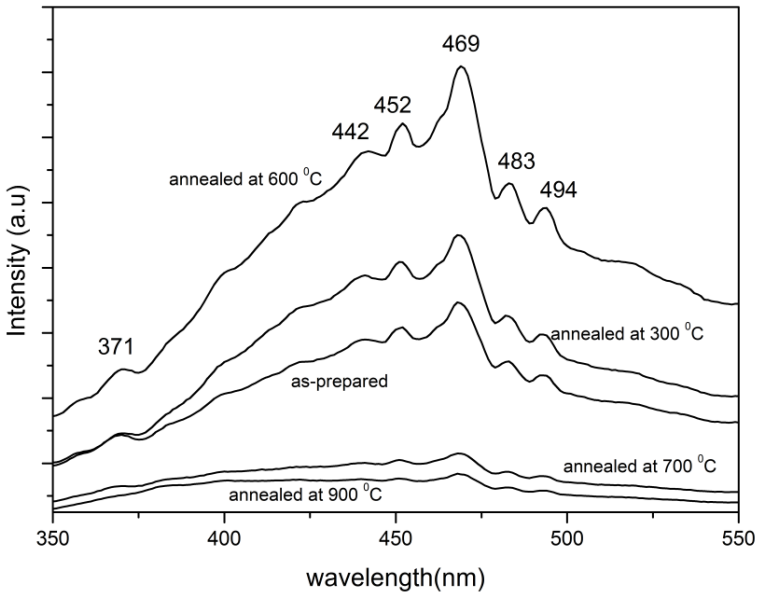

Figure 3.8: PL spectra of the as-prepared and annealed CeO_2 nanoparticles

between the envelop functions of electrons and holes increases with decreasing grain size, leading to the enhancement of the STE binding energy. The enhanced STE binding energy may prolong the STE radiative life time. The dielectric confinement effect also enhances the binding energy because of the penetration of electric force lines between electrons and holes into the surrounding medium. The dielectric confinement effect would become stronger in small sized CeO_2, and in the present work the synthesized nanostructured CeO_2 has a high dielectric constant value around 76 for 1 KHz frequency at room temperature. The small sized particles can introduce more opportunity for the electric force lines to penetrate into the surrounding medium like air with relatively much lower dielectric constant with respect to the CeO_2. When CeO_2 nanoparticles with high dielectric constant are surrounded by air with very low dielectric constant, the dielectric confinement effect is certainly remarkable [23]. Above 600 ^{0}C, however PL intensity starts to drop, and almost disappears for the sample annealed at 900 ^{0}C. It is seen from the table 3.1 that the grain size increases slightly from 9 nm to 12 nm up to 600 ^{0}C. Hence the influence of the grain size on the concentration of STEs is not very significant in the temperature range from room temperature to 600 ^{0}C. However, the dielectric constant of CeO_2 annealed at 600 ^{0}C has the highest value which is around 84. It is observed that PL intensity is maximum for samples annealed at 600 ^{0}C and it decreases for further increase in annealing temperatures. The reason for highest PL intensity for the sample annealed at 600 ^{0}C can be related to the highest dielectric constant value and the comparatively lower grain size. For the samples annealed at 900 ^{0}C the dielectric constant drastically decreases and grain size increases to around 26 nm. The dielectric constant sharply decreases to 31 for the samples annealed at 900 ^{0}C. Hence the increase of concentration of

STE is mainly due to the dielectric confinement effect and, it is only slightly influence by the change in grain size. This STE phenomenon is observed in $SrTiO_3$ in which case maximum PL emission is observed for the samples annealed at 700 ^{0}C. The present observation of STE phenomenon in nanostrucutred CeO_2, based on the dependence of PL emission on the annealing temperature is novel and has not been reported earlier. Figure 3.8 also shows that the spectral lines remain unchanged and the PL peak positions have no detectable shifts for various annealing temperatures.

The nanostructured CeO_2 having intense PL emission at around 469 nm hence, can be used as excellent oxygen ion conductor. These nanocrystals have prospects of applications in developing efficient solid oxide fuel cells.

3.4. Conclusion

Nanocrystalline CeO_2 powder samples have been prepared by hydrolysis assisted chemical precipitation method employing cerium chloride and ammonia as precursors. The prepared samples are air annealed at different temperatures up to 900 ^{0}C. XRD and TEM studies confirm the cubic phase CeO_2 nanocrystalline particle formation. Particle size increases with increase in annealing temperature and lattice parameter decreases. Strong PL emission has been observed around 469 nm which is mainly due to the presence of oxygen vacancies. The dependence of PL emission intensity on the annealing temperatures is explained on the basis of the self trapped exciton phenomenon. Though STE mechanism has already been reported in other oxide systems such as $SrTiO_3$, this is the first time that STE mediated PL emission has been reported for nanostructured ceria samples synthesized by chemical precipitation techniques. In the present work, the dependence of PL intensity on the annealing temperatures,

gives a clear indication of the effect of the dielectric confinement on the formation of self trapped excitons.

References

[1] Z Yang, K Zhou, X Liu, Q Tian, D Lu, S Yang, Nanotechnology 18 (2007) 185606

[2] M Y Li, Z L Wang, S S Fan, Q T Zhao, G C Xiang, Nuclear instruments & methods in Physics Research B 135 (1998) 535

[3] H Chen, H Chan, Colloids and surfaces A: Physicochem. Eng. Aspects 242 (2004) 61

[4] A C Bose, R Ramamoorthy, S Ramaswamy, Mat. Lett. 44 (2000) 203

[5] A C Bose, P Thangadurai, S Ramaswamy, Mat. Chem. Phy. 95 (2006) 72

[6] T Dhannia, S Jayalekshmi, M C Santhosh Kumar, T Prasada Rao, A Chandra Bose, J. Phys. Chem. solids 70 (2009) 1443

[7] T Dhannia, S Jayalekshmi, M C Santhosh Kumar, T. Prasada Rao, A. Chandra Bose, J. Phys. Chem. solids 71 (2010) 1020

[8] B D Cullity, S R Stock, Elements of X-ray Diffraction, 3rd Edn, Prentice Hall, New Jersey (2001)

[9] V N Morris, R A Farrell, A M Sexton, M A Morris, J. Phys. Conf. Ser. 26 (2006) 119

[10] S Deshpande, S Patil, S VNT Kuchibhatla, S Seal, Appl. Phys. Lett. 87 (2005) 133113

[11] C Hu, Z Zhang, H Liu, P Gao, Z L Wang, Nanotechnology 17 (2006) 5983

[12] Y X Li, W F Chen, X Z Zhou, Z Y Gu, C M Chen, Mater. Lett. 59 (2005) 48

[13] K Nakamoto, Infrared and Raman Spectra of Inorganic and Coordination Compounds: part-A; Theory and Application in Inorganichemistry, 5th edn, John Wiley & sons, New York (1997)

[14] M G Sujana, K K Chattopadyay, S Anand, Appl. Surf. Sci. 254 (2008) 7405

[15] M L Dos Santos, R C Lima, C S Riccardi, R L Tranquilin, P R Bueno, J A Varela, E Longo, Mater. Lett. 62 (2008) 4509

[16] H Chen, H chang, Ceram. Int. 31 (2005) 795

[17] D Zhang, X Ni, H Zheng, X Zhang, J Song, Solid State Sci. 8 (2006)1290

[18] L Djellala, A Bougueliab, H M Kadi, M Trarib, Sol. Ener. Mater. Solar Cells 92 (2008) 594

[19] L Truffault, M Ta, T Devers, K Konstantinov, V Harel, C Simmonard, C Andreazza, I P Nevirkovets, A Pineau, O Veron, J Blondeau, Mat. Res. Bull. 45 (2010) 527

[20] S Sathyamurthy, K J Leonard, R T Dabestani, M Parans Paranthaman, Nanotechnology 16 (2005) 1960

[21] S Phoka, P Laokul, E Swatsitang, V Promarak, S Seraphin, S Maensiri, Mater. Chem. Phys. 115 (2009) 423

[22] P Patsalas, S Logothetidis, Phys. Rev. B 68 (2003) 035104.

[23] W F Zhang, Z Yin, M S Zhang, Z L Du, W C Chen, J. Phys: Condens. Matt. 11 (1999) 5655

Chapter 4

SYNTHESIS, STRUCTURAL AND OPTICAL CHARACTERIZATION OF DOPED CERIUM OXIDE NANOCRYSTALS

Contents

4.1. Introduction

Cerium oxide is a fluorite-structured material and it does not show any crystallographic structural change from room temperature up to its melting point (2700 ^{0}C). Ceria based solid solutions have been widely accepted as promising electrolytes for intermediate temperature solid oxide fuel cells (SOFC). Synthesis of ceria-based solid solutions with controllable concentrations of oxygen vacancies is of great fundamental significance because properties and applications of ceria-based solid solutions are determined by defect chemistry related to these concentrations, as well as effects from dopant size and valence. Ceria shows much improved properties under doping. The fluorite lattice is also capable of oxygen storage via electron flow between Ce^{4+} ⇆ Ce^{3+} [1]. The key factor in the design of modified ceria is the choice of doping elements, as well as their amount introduced. In addition, the preparation method of the powder has also very strong influence on the homogeneity and stability of the solid solutions [2]. Ionic conductivity in ceria is closely related to oxygen vacancy formation and

migration properties. A clear physical picture of the connection between the choice of a dopant and the improvement of ionic conductivity in ceria is still lacking [3]. It has been observed that the conductivity of ceria solid solutions tends to be dependent upon the dopant concentration, and a separate maximum is exhibited for each dopant. Attempts have been made in the present work to synthesize solid solutions of metal doped ceria using iron, aluminium and cobalt as dopants and investigate their structural, optical and magnetic properties. These details are given in this chapter. However, due to time constraints and the lack of facilities the dependence of ionic conductivity on dopant concentration couldnot be investigated in detail.

Nano-crystalline fluorite–like structures of iron, aluminium and cobalt doped cerium oxide compounds were prepared by chemical precipitation method. The synthesized samples were characterized by XRD, EDX, TEM, DRS, FT-IR and PL. The effect of thermal annealing on the particle size, lattice parameter and band gap energy was also investigated.

4.2. Experimental techniques

4.2.1. Synthesis of doped ceria

a. Iron doped ceria

Aqueous solutions of cerium chloride ($CeCl_3.7H_2O$) and iron chloride ($FeCl_3$) were taken in a flask fitted with a Liebig's condenser. The mixed solution was heated at 120 ^{0}C in an electric oven and the evaporated solution was condensed back to the flask by the Liebig's condenser. This process of hydrolysis was carried out for 72 hours [4]. An appropriate amount of ammonium hydroxide was added to the hydrolyzed solution and the obtained

precipitate was washed many times with doubly distilled water to remove the remaining ammonia solution and then dried at 100 ^{0}C for 1 h.

b. Aluminium doped ceria

Aluminium doped ceria samples were similarly prepared by mixing 0.1 M aqueous solution of aluminum chloride with that of cerium chloride. Exactly similar process as above was adapted and the obtained product was thoroughly washed and dried [5].

c. Cobalt doped ceria

Cobalt doped ceria samples were prepared adopting an exactly similar procedure as above using 0.1 M aqueous solutions of cerium chloride and cobalt chloride. As before an appropriate amount of ammonia solution was added till precipitation and the obtained precipitate was washed and dried.

4.2.2. Characterizations

X-ray diffraction studies were carried out for the as-prepared and annealed samples using a Rigaku Ultima-III X-ray diffractometer using Cu Kα_1 radiation in the 2θ range from 20^0 to 80^0 at 30 kV, 20 mA at a scanning rate of 3^0/min. JEOL JEM-2010 was used to record the TEM images. EDX spectra were recorded using Jeon JSM- 6390 LA instrument. FT-IR spectra of the samples were obtained using Perkin Elmer FT-IR spectrometer. UV-Vis Diffuse Reflectance Spectra were recorded using JASCO V570 UV-VIS-NIR Spectrometer. The photoluminescence emission spectra were taken using Jobin Yvon Flourimeter using Xe lamp as excitation source under an excitation wavelength of 325 nm.

4.3. Results and discussion

The XRD patterns of the three different concentrations (5, 10, 15 mol %) of iron, aluminum and cobalt doped cerium oxide samples in different annealing conditions are shown in figure 4.1 (a-i). The broad peaks obtained in the samples indicate the nanocrystalline structure. It is observed that with thermal annealing, broadening of the peak decreases; at the same time, the peak intensity increases, suggesting larger crystallite sizes [4,5]. The characteristic peaks are confirmed to be corresponding to the cubic fluorite structured CeO_2 (Fm3m, JCPDS file 81-0792).

Figure 4.1 (a - c) show the XRD patterns of iron doped ceria samples in the as-prepared and annealed conditions. It is seen that all the XRD patterns correspond to single–phased CeO_2 phase which has a fluorite type cubic structure. They display reflections only from cubic ceria (fluorite structure) which means that homogeneous cubic ceria can be obtained through doped ceria also with low concentration of the dopant Fe, in air. When the solid solution is formed, its structure is corresponding to that of the cubic ceria in which some of the Ce^{4+} cations have been substituted by Fe^{3+} cations. The solid solution can be formulated as $Ce_{1-x}Fe_xO_{2-\delta}$, indicating that electrical neutrality is achieved by the O-vacancy formation mechanism [6]. However, in the XRD patterns of 15 % iron doped ceria (Figure 4.1 (c)), there is an additional peak observed at $\sim 35.7^0$ which corresponds to Fe_2O_3 cubic phase in addition to CeO_2 cubic phase. It is formed from unsubstituted iron in the doped sample, which is quite possible since ionic radii of Ce^{4+} ($0.92A^0$) and Fe^{3+} ($0.64A^0$) are quite different [4].

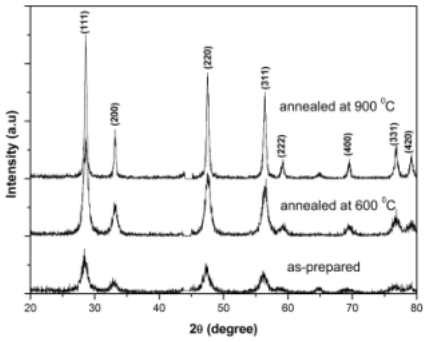

(a) $Ce_{0.95}Fe_{0.05}O_{2-\delta}$

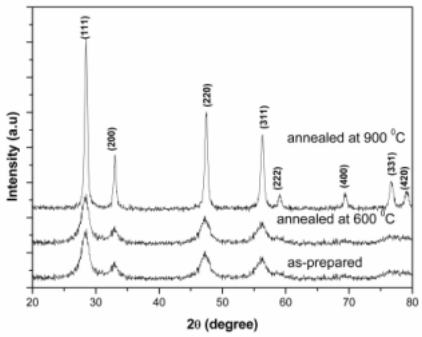

(b) $Ce_{0.9}Fe_{0.1}O_{2-\delta}$

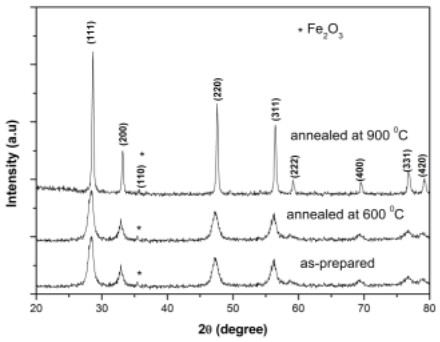

(c) $Ce_{0.85}Fe_{0.15}O_{2-\delta}$

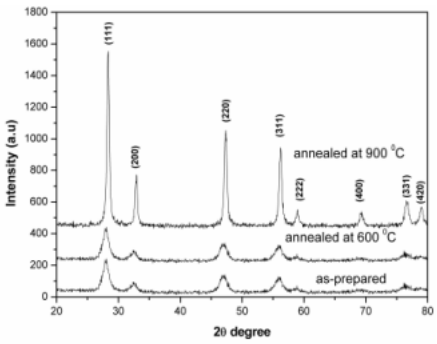

(d) $Ce_{0.95}Al_{0.05}O_{2-\delta}$

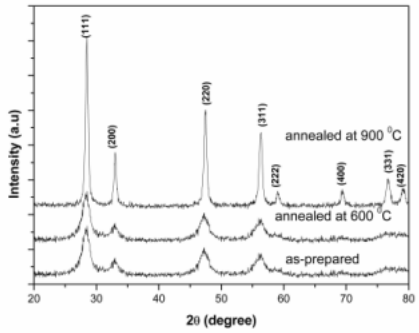

(e) $Ce_{0.9}Al_{0.1}O_{2-\delta}$

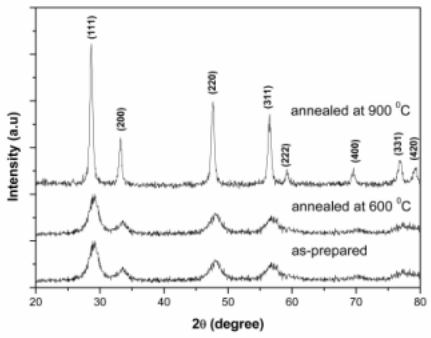

(f) $Ce_{0.85}Al_{0.15}O_{2-\delta}$

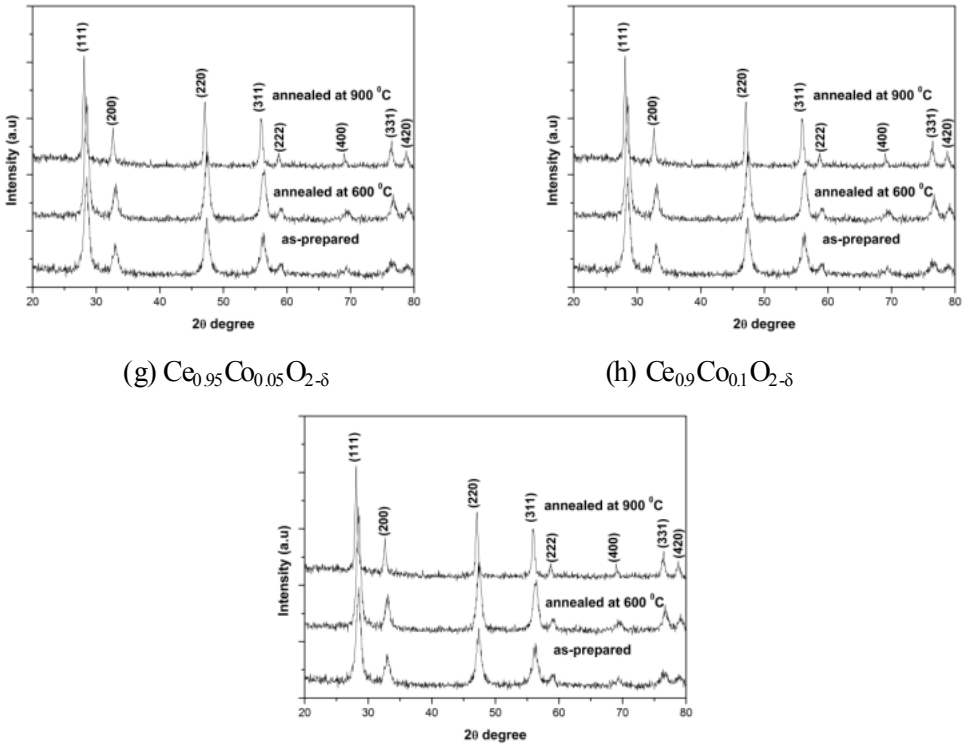

(g) $Ce_{0.95}Co_{0.05}O_{2-\delta}$ (h) $Ce_{0.9}Co_{0.1}O_{2-\delta}$

(i) $Ce_{0.85}Co_{0.15}O_{2-\delta}$

Figure 4.1: XRD patterns of iron, aluminum and cobalt doped ceria

The XRD patterns of aluminium and cobalt doped samples (figure 4.1(d-i)) display reflections only from cubic ceria. As described above, in aluminum doped ceria, some of the Ce^{4+} cations have been substituted by Al^{3+} cations and in cobalt doped ceria some of the Ce^{4+} cations have been substituted by Co^{2+} cations. So the solid solutions can be formulated as $Ce_{1-x}Al_xO_{2-\delta}$ and $Ce_{1-x}Co_xO_{2-\delta}$, indicating that electrical neutrality is achieved by the O-vacancy formation mechanism [6].

Grain size of the as-prepared and annealed samples is calculated from XRD data using Scherrer's formula [7]

$$\text{Average grain size } t_{xrd} = \frac{0.9\lambda}{\beta \cos\theta}, \qquad (1)$$

where λ is the wavelength of the incident X-rays (1.5406 Å) β is Full Width Half Maximum and θ the diffraction angle.

Table 4.1: Variation of lattice parameter and grain size with annealing temperature

Sample		Lattice parameter (A^0)	Grain size(nm)
$Ce_{0.95}Fe_{0.05}O_{2-\delta}$	As-prepared	5.42	9.36
	Annealed at 600 ^{0}C	5.40	11.1
	Annealed at 900 ^{0}C	5.40	25.8
$Ce_{0.90}Fe_{0.10}O_{2-\delta}$	As-prepared	5.43	9.34
	Annealed at 600 ^{0}C	5.40	11.0
	Annealed at 900 ^{0}C	5.40	25.2
$Ce_{0.85}Fe_{0.15}O_{2-\delta}$	As-prepared	5.44	9.30
	Annealed at 600 ^{0}C	5.42	10.8
	Annealed at 900 ^{0}C	5.39	25.0

Sample		Lattice parameter (Å)	Grain size(nm)
$Ce_{0.95}Al_{0.05}O_{2-\delta}$	As-prepared	5.37	6.4
	Annealed at 600 ^{0}C	5.36	8.6
	Annealed at 900 ^{0}C	5.36	19.5
$Ce_{0.90}Al_{0.10}O_{2-\delta}$	As-prepared	5.40	6.2
	Annealed at 600 ^{0}C	5.39	7.4
	Annealed at 900 ^{0}C	5.38	18.6
$Ce_{0.85}Al_{0.15}O_{2-\delta}$	As-prepared	5.41	6.1
	Annealed at 600 ^{0}C	5.40	7.3
	Annealed at 900 ^{0}C	5.38	18.4

Sample		Lattice parameter (Å)	Grain size(nm)
$Ce_{0.95}Co_{0.05}O_{2-\delta}$	As-prepared	5.38	6.8
	Annealed at 600 ^{0}C	5.37	8.4
	Annealed at 900 ^{0}C	5.36	19.5
$Ce_{0.90}Co_{0.10}O_{2-\delta}$	As-prepared	5.40	6.6
	Annealed at 600 ^{0}C	5.39	7.5
	Annealed at 900 ^{0}C	5.38	18.6
$Ce_{0.85}Co_{0.15}O_{2-\delta}$	As-prepared	5.41	5.0
	Annealed at 600 ^{0}C	5.39	6.9
	Annealed at 900 ^{0}C	5.38	18.4

Table 4.1 shows the variations of lattice parameter and grain size with concentrations of iron, aluminium and cobalt and annealing temperature. In all these samples, the lattice parameter increases with increase in doping concentrations. The change in the lattice parameter in doped samples is directly related to the ionic size of the dopants. The ionic sizes of the Ce^{4+}, Fe^{3+}, Al^{3+} and Co^{2+} are given below:

Ce^{4+} ---- ($0.92A^0$)

Fe^{3+} ----- ($0.64A^0$)

Al^{3+} ----- ($0.53A^0$)

Co^{2+} -----($0.70\ A^0$)

Because of the smaller size of the dopants, there should be considerable decrease in the lattice parameter of the CeO_2 lattice. However, as the concentration of dopants increases, there is a simultaneous increase in the oxide ion vacancy and this leads to an increase in the lattice parameter [8]. The increase of the lattice parameter with doping indicates that the volume of the cell has increased due to the effective doping.

The grain size decreases with increase in dopant concentrations for all the three dopants. Basically, the addition of a dopant into a crystalline structure affects the crystalline growth kinetics. Before inserting itself into the CeO_2 structure, the dopants are first located between the grain boundaries and thus disturb the normal growth of CeO_2 crystallites [9].

Lattice parameter is found to be decreasing with increase in annealing temperature because annealing removes the defect states in the samples. Grain size is found to be increasing with increase in annealing temperature due to the enhancement of crystallinity. With the increase of annealing temperature, the growth rate of particles increases more rapidly than the nucleation rate does,

and the aggregation trend of particles becomes stronger. Therefore, the average size of CeO_2 particles increases with increase in annealing temperature [10].

The morphology of the doped cerium oxide nanopowder is investigated by TEM. TEM images of the iron, aluminium and cobalt doped ceria nanoparticles are shown in figure 4.2 (a-i).[Enlarged TEM images are given in page no. 145-147]. The images show that the fine particles are more or less spherical in shape in iron and aluminum doped ceria and each particle is found to be an aggregate of nanocrystallites. Basically, nanoparticles have a natural tendency to agglomerate for two main reasons. The agglomeration is a more stable configuration from an energetic point of view. Thus, nanoparticles tend to agglomerate to allow smooth crystallite growth [11]. The number of these agglomerates is observed to increase with increase in iron concentration. These TEM results confirm that grains are nanometer in size and show good agreement with the XRD results.

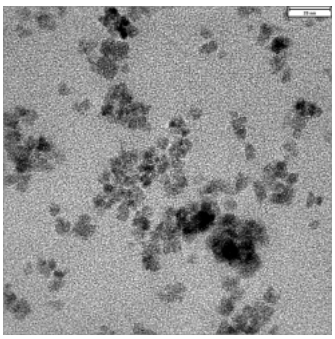

(a)$Ce_{0.95}Fe_{0.05}O_{2-\delta}$

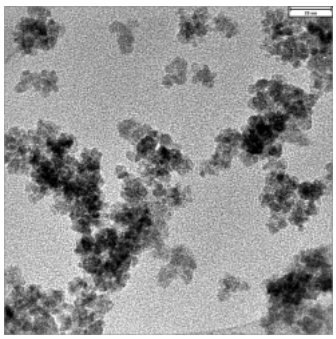

(b) $Ce_{0.90}Fe_{0.10}O_{2-\delta}$

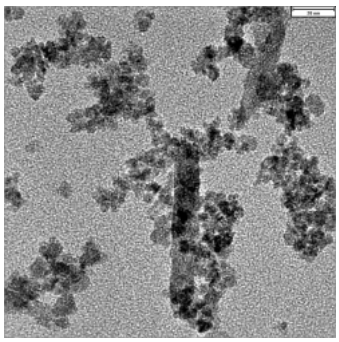

(c) $Ce_{0.85}Fe_{0.15}O_{2-\delta}$

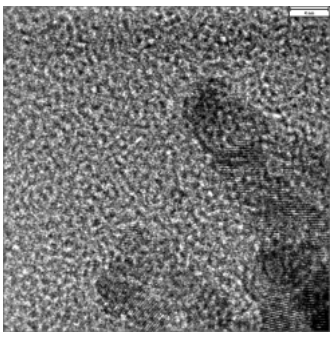

(d) $Ce_{0.95}Al_{0.05}O_{2-\delta}$

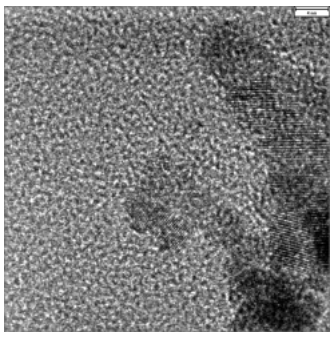

(e) $Ce_{0.90}Al_{0.10}O_{2-\delta}$

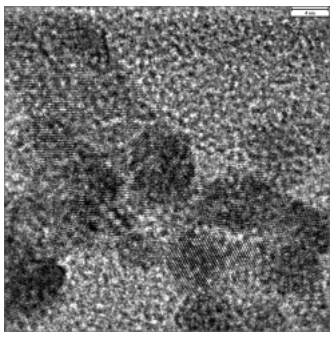

(f) $Ce_{0.85}Al_{0.15}O_{2-\delta}$

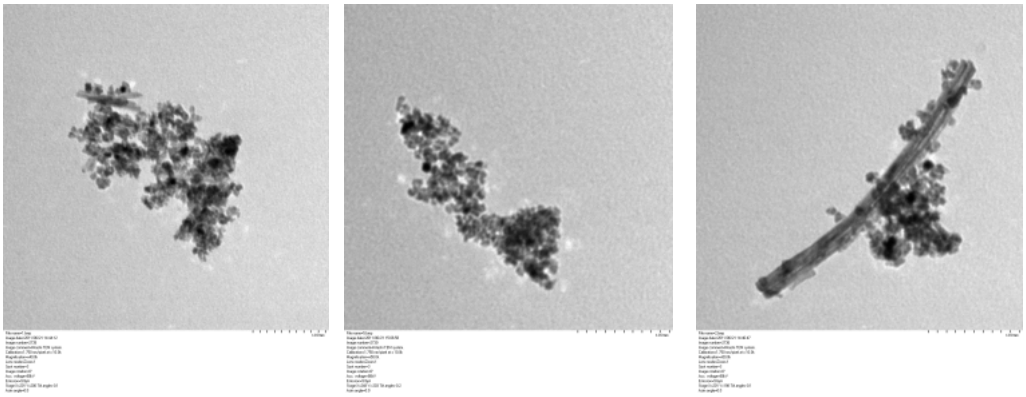

(g)$Ce_{0.95}Co_{0.05}O_{2-\delta}$ (h)$Ce_{0.90}Co_{0.10}O_{2-\delta}$ (i)$Ce_{0.85}Co_{0.15}O_{2-\delta}$

Figure 4.2: TEM images of iron, aluminum and cobalt doped ceria

15% cobalt doped ceria shows a rod like character. Actually the morphology of the products will be changed a lot by adjusting pH value of the solution. In acid solution, the product becomes spherical shape and the product can be spherical and rod–like when the solution is neutral, but if the solution is alkaline, the shape turns rod-like with a ratio of diameter and length about 1:10. According to Shinryo's theory, the formation of rod–like and spherical crystallites depends on the pH value of the solution in the course of Ce^{3+}/Ce^{4+} conversion and the reaction mechanism in acid and alkaline solution obeys the decomposition precipitation mechanism [12]. So the observation of both spherical and rod like cerium oxide particles in the 15% cobalt doped sample can be explained using the above theory.

Energy–dispersive x-ray (EDX) images of the doped cerium oxide nanoaprticles are shown in figure 4.3(a-c). They clearly show the presence of Ce, O and Fe in iron doped ceria, Ce, O and Al in aluminium doped ceria, Ce, O and Co in cobalt doped ceria. The synthesized materials are hence pure without contaminations.

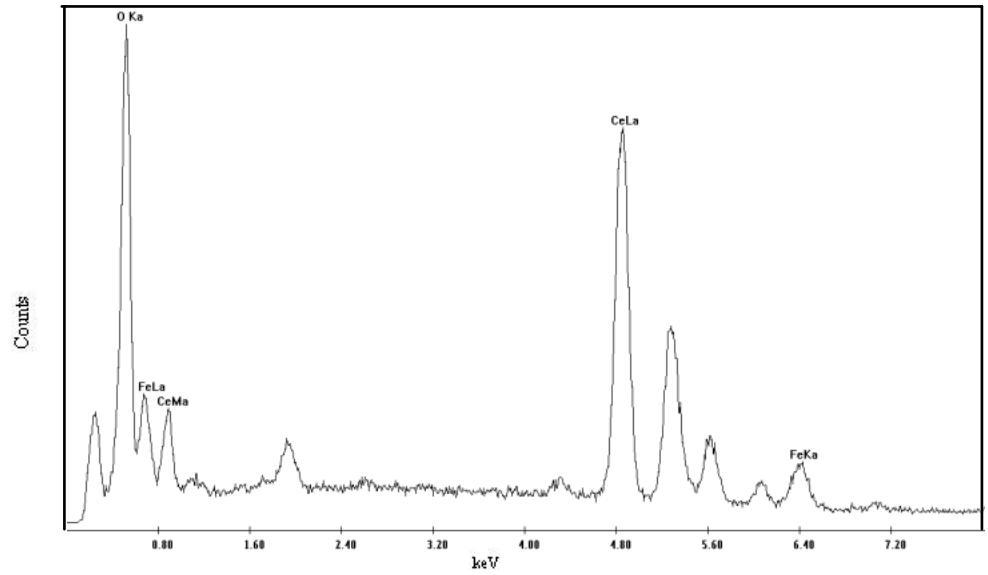

(a) iron doped

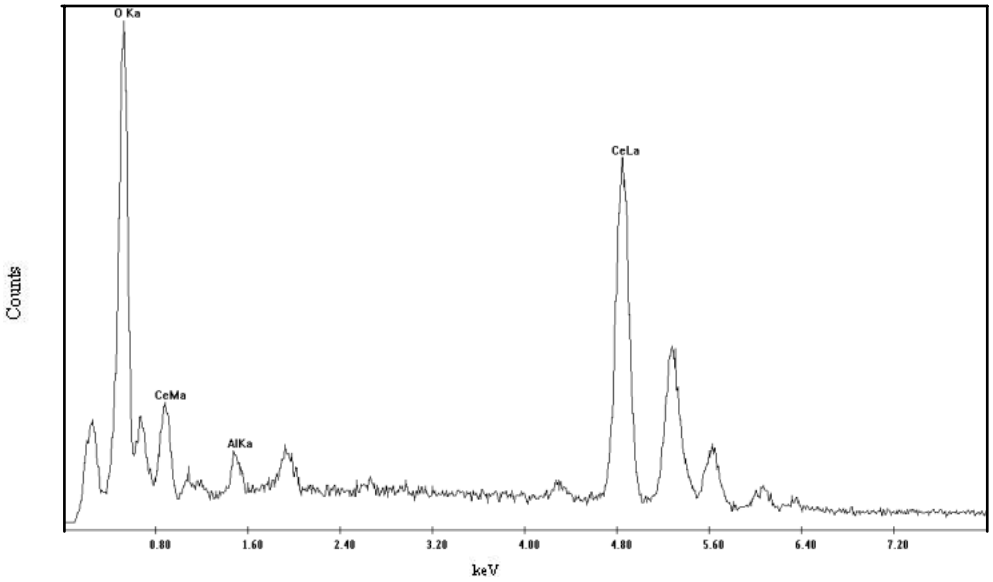

(b) aluminum doped

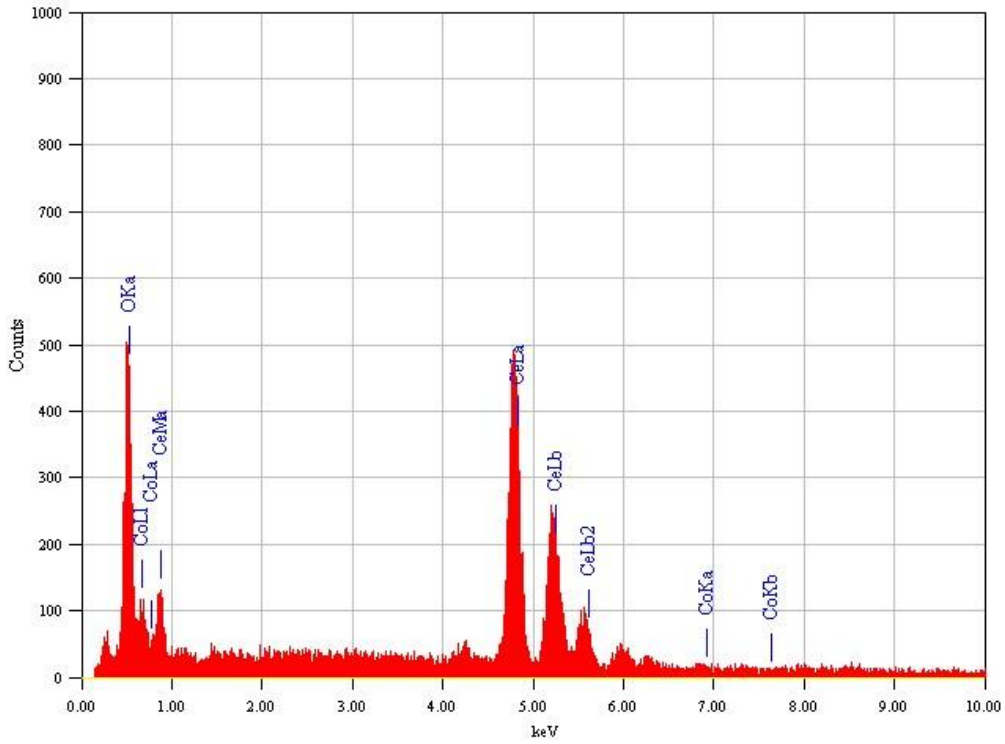

(c) cobalt doped

Figure 4.3: EDX of doped ceria

The FT-IR spectra in the transmission mode of iron, aluminium and cobalt doped ceria in the as-prepared conditions and in different dopant concentrations are presented in figure 4.4 (a-c). All the spectra show a strong peak around 3500 cm^{-1} due to O-H bond of water molecules**.** The carbonation of ceria is unavoidable. These effects can be clearly seen from bands in between 2000 cm^{-1} -1000 cm^{-1}. In figure 4.4 (a) the peaks corresponding to 492 cm^{-1}, 504 cm^{-1}, 506 cm^{-1} represent Ce-O vibration mode, 761 cm^{-1} represents Fe-OH, 880 cm^{-1} represents Fe-O mode. In figure 4.4(b), the peak corresponding to 499 cm^{-1} represents Ce-O mode and 715 cm^{-1} represents Al-O mode[13, 14].

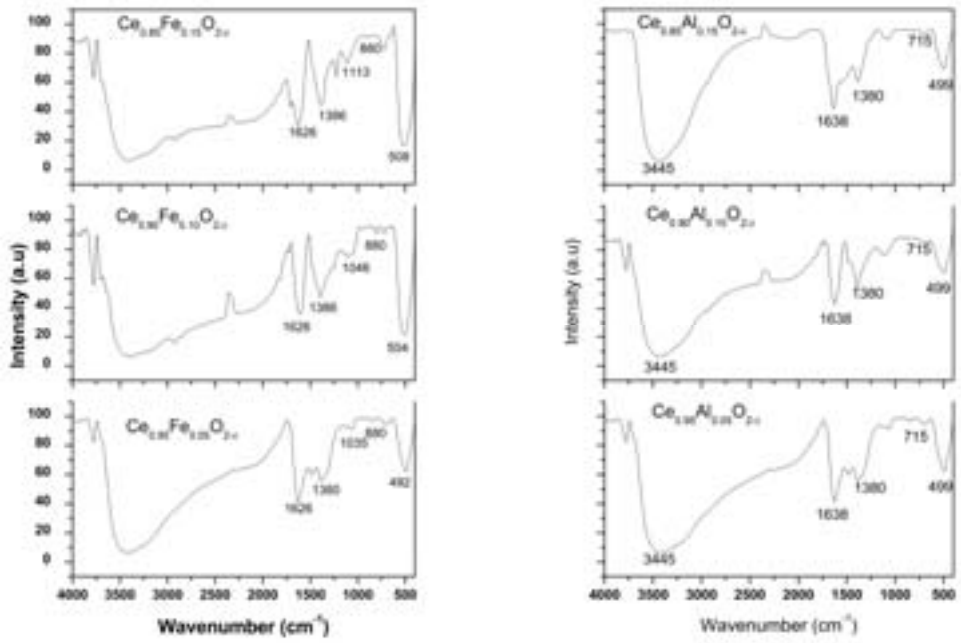

a) iron doped b) aluminum doped

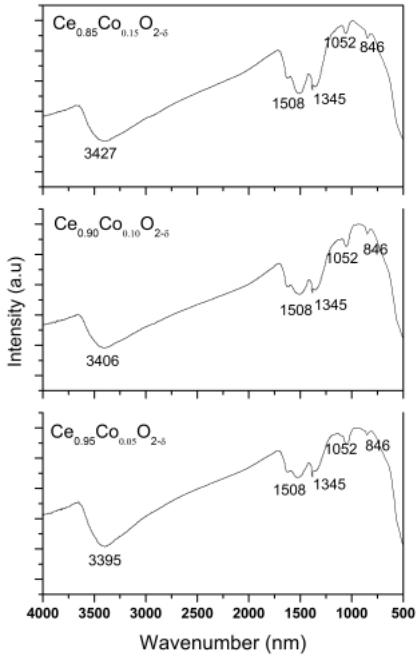

c)cobalt doped

Figure 4.4: FT-IR spectra of iron, aluminum and cobalt doped ceria

Figures 4.5 (a-i) show the diffuse reflectance spectra of iron, aluminium and cobalt doped ceria corresponding to different annealing temperatures and doping concentration. The dips in the iron doped ceria suggest the presence of significant amount of midgap defect states in the system. Earlier studies about defect states in ceria have shown that it is quite prone to oxygen vacancies, while it still retains its fluorite structure over a wide range of non stoichiometic compositions through the inclusion of oxygen vacancies [15].

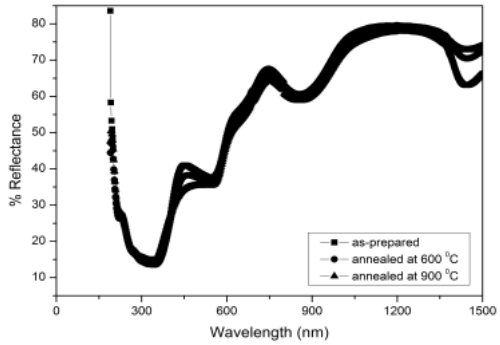

(a) $Ce_{0.95}Fe_{0.05}O_{2-\delta}$

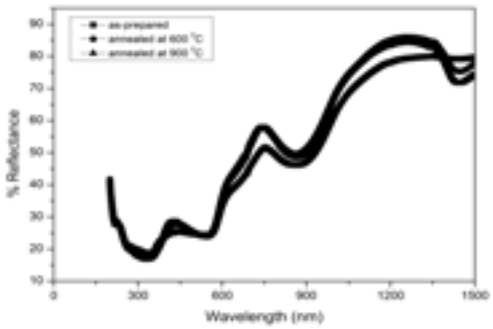

(b) $Ce_{0.9}Fe_{0.1}O_{2-\delta}$

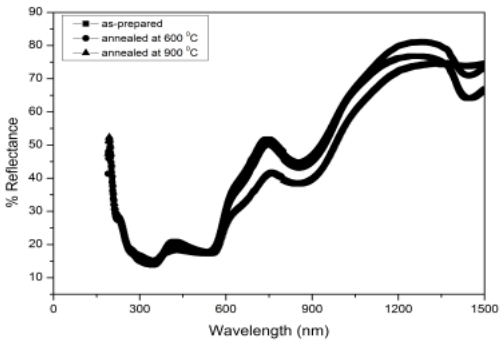

(c) $Ce_{0.85}Fe_{0.15}O_{2-\delta}$

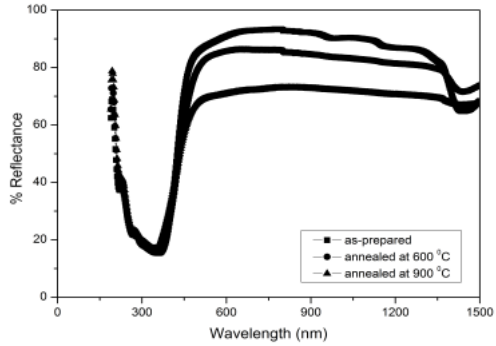

(d) $Ce_{0.95}Al_{0.05}O_{2-\delta}$

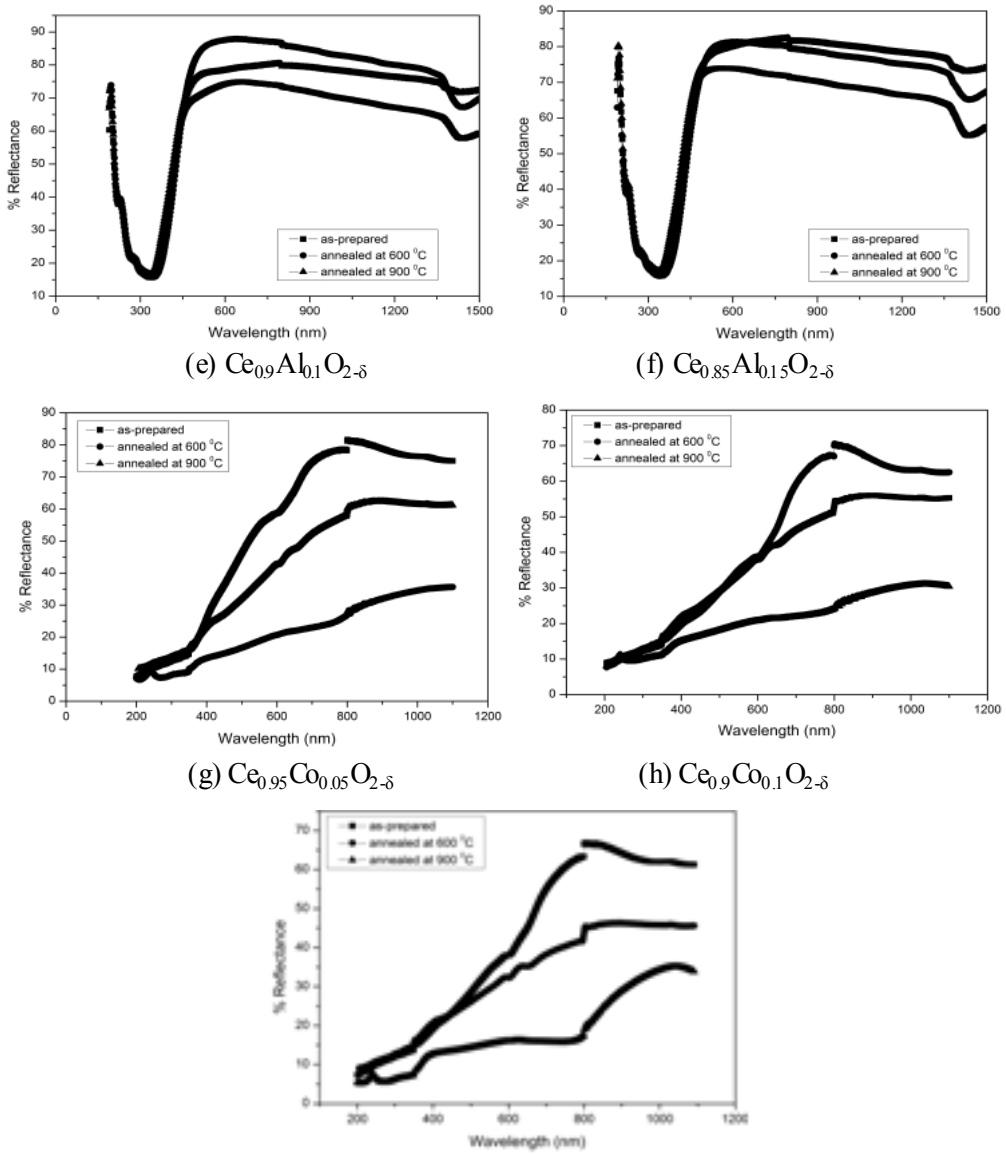

(e) $Ce_{0.9}Al_{0.1}O_{2-\delta}$ (f) $Ce_{0.85}Al_{0.15}O_{2-\delta}$

(g) $Ce_{0.95}Co_{0.05}O_{2-\delta}$ (h) $Ce_{0.9}Co_{0.1}O_{2-\delta}$

(i) $Ce_{0.85}Co_{0.15}O_{2-\delta}$

Figure 4.5: DRS spectra of iron, aluminum and cobalt doped ceria

The absorption coefficients of the samples were calculated from Munk-Kubleka relation, which is useful for compounds that are difficult to analyze in transmission mode [16].

$$\frac{k}{s} = \frac{(1-R_\infty)^2}{2R_\infty} \qquad (2)$$

R_∞ is the diffuse reflectivity from an infinitely thick layer of powder, k the absorption coefficient and s the scattering factor independent of wavelength for particle sizes larger than the wavelength of light. Figures 4.6 (a-i) show the plot of absorption coefficient with wavelength of doped ceria corresponding to various doping concentrations and annealing conditions. The absorption curve is composed of one large band, whose maximum is located at around 340 nm. The low intensity band at 270 nm can be ascribed to the intrinsic character of CeO_2. The intensity of the absorption peak decreases with the increase in particle size. For CeO_2, the fundamental absorption is due to a charge transfer between the filled 2p (O) orbital and the empty 4f (Ce) orbital, which corresponds to an experimental band-gap value of 3.19 eV for the bulk [9]. Iron doped ceria absorbs more UV radiation between 200 to 400 nm than pure ceria sample. The absorption band around 560 nm is due to the presence of α Fe_2O_3. This absorption feature is a characteristic of the d-d transitions of octahedrally coordinated Fe^{3+} ions [17]. Intensity of this band increases with increasing the

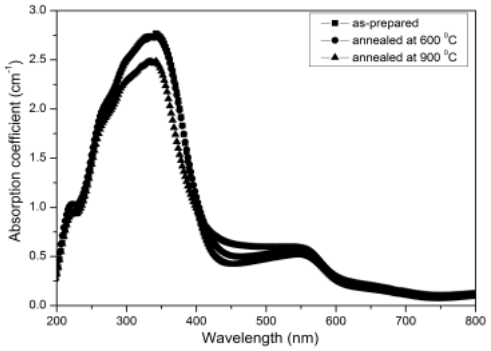

(a) $Ce_{0.95}Fe_{0.05}O_{2-\delta}$

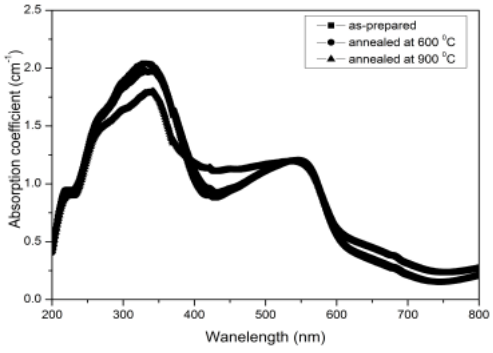

(b) $Ce_{0.9}Fe_{0.1}O_{2-\delta}$

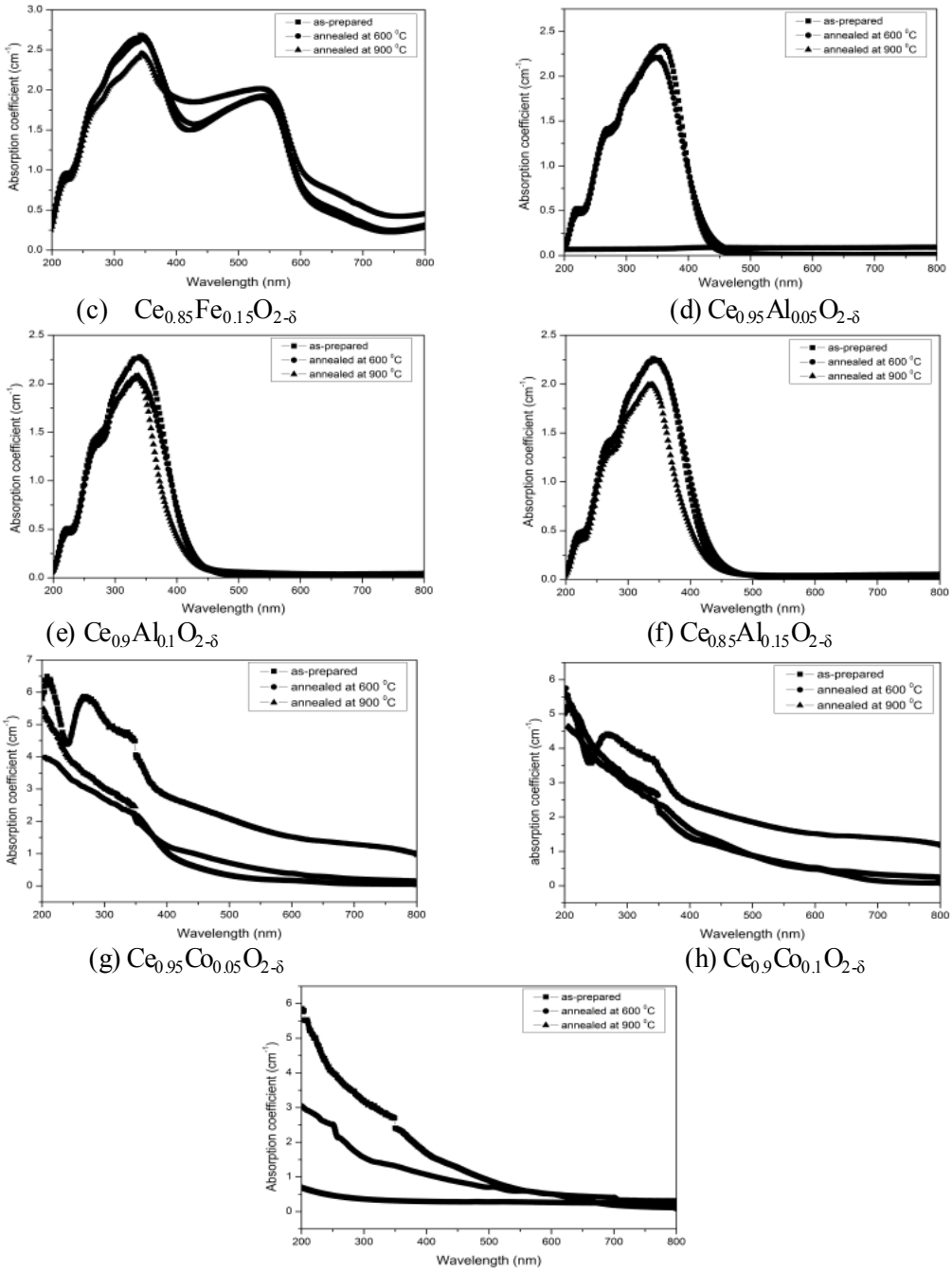

(c) $Ce_{0.85}Fe_{0.15}O_{2-\delta}$ (d) $Ce_{0.95}Al_{0.05}O_{2-\delta}$

(e) $Ce_{0.9}Al_{0.1}O_{2-\delta}$ (f) $Ce_{0.85}Al_{0.15}O_{2-\delta}$

(g) $Ce_{0.95}Co_{0.05}O_{2-\delta}$ (h) $Ce_{0.9}Co_{0.1}O_{2-\delta}$

(i) $Ce_{0.85}Co_{0.15}O_{2-\delta}$

Figure 4.6: Variation of absorption coefficient of iron, aluminium and cobalt doped ceria with wavelength

concentration of Fe^{3+} ions. Aluminium and cobalt doped samples also absorb in the 200 to 400 nm wavelength range. In the case of aluminium and cobalt doped ceria, intensity of absorbance is more or less same with doping concentration. With increasing the dopant ion content, the absorption edge gradually shifts towards higher wavelength.

The relation $(\alpha h\nu) = A(h\nu - E_g)^n$ remains valid if the coefficient α is replaced by k/s. Where E_g is the band gap, ν is the frequency, A is a constant and n can have values 1/2, 3/2, 2 and 3 depending up on the mode of inter band transition i.e. direct allowed, direct forbidden, indirect allowed and indirect forbidden transition respectively. The direct optical band gap E_g is determined by extrapolating the curve $(h\nu k/s)^2$ vs. $(h\nu)$ to zero absorption (Tauc plot) as shown in figure 4.7 (a-i). Similarly plotting $(h\nu k/s)^{1/2}$ as a function of photon energy $(h\nu)$, and extrapolating the linear portion of the curve to absorption equal to zero as shown in figure 4.8 (a-i), gives the value of the indirect allowed transition [18].

Table 4.2 shows a comparison of direct and indirect band gap energies of the as-prepared nano-crystalline samples with different doping concentration and annealing temperature. The heavy doping affects the density of states, carrier mobility, absorption, luminescence properties and hence device properties. Also, heavy doping produces some changes in band structure of semiconductors. One of the changes is band gap narrowing (BGN) or band gap shrinkage due to the formation of density of states, and the tails are resulted from inhomogeneous impurity distribution [19]. Here both direct and indirect band gap energies are found to decrease with increase in the concentration of dopants. This is due to the band tailing effect. The impurity distribution in a

heavily doped semiconductor is not uniform. The fluctuation of potential energy causes a spatial dependence of the local density of states. Macroscopically, it results in a band tail of both conduction band and valence band [20]. The decreasing trend also indicates that the dopants are incorporated into CeO_2 matrix.

As the annealing temperature increases, the particle size increases and both direct and indirect band gap energies decrease. So the band gap has an inverse dependence on the grain size. Electrons are highly localized in nanoparticles and the interaction between these localized states give rise to the observed band gap. As the temperature increases, these localized states spread modifying the band structures, resulting in a reduction in band gap.

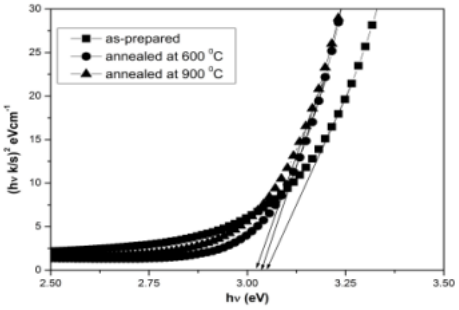

(a) $Ce_{0.95}Fe_{0.05}O_{2-\delta}$

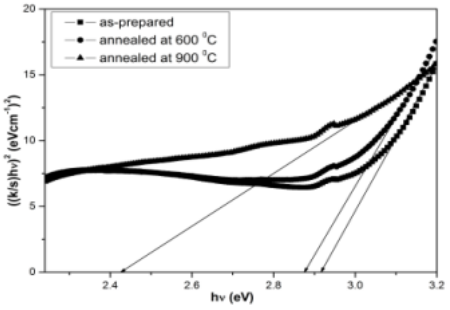

(b) $Ce_{0.9}Fe_{0.1}O_{2-\delta}$

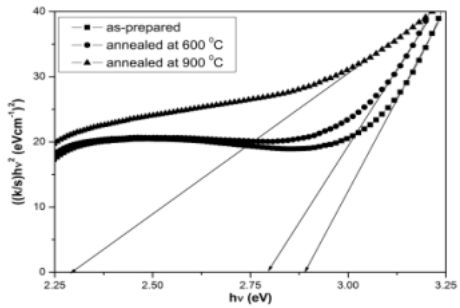

(c) $Ce_{0.85}Fe_{0.15}O_{2-\delta}$

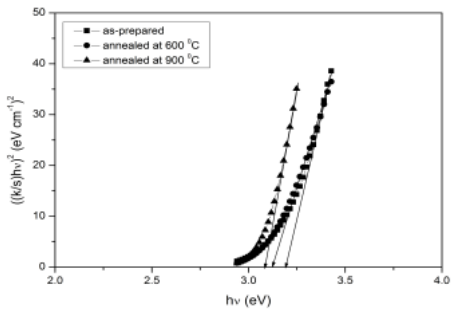

(d) $Ce_{0.95}Al_{0.05}O_{2-\delta}$

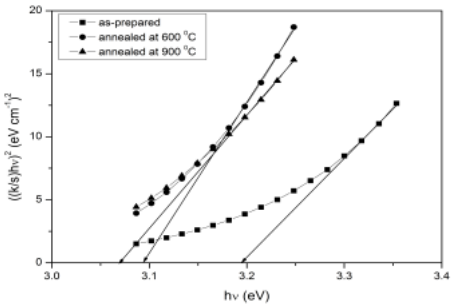

(e) $Ce_{0.9}Al_{0.1}O_{2-\delta}$

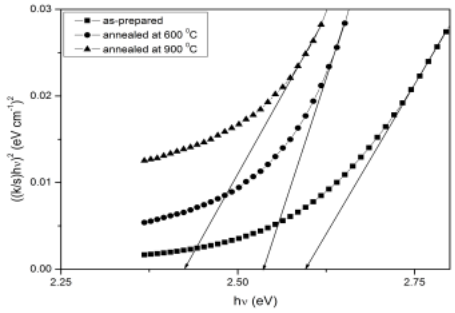

(f) $Ce_{0.85}Al_{0.15}O_{2-\delta}$

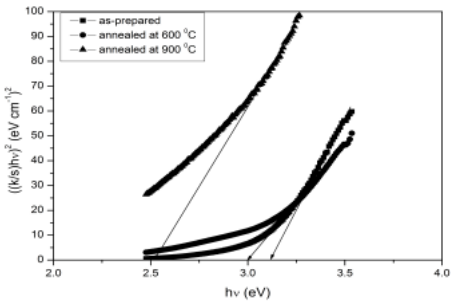

(g) $Ce_{0.95}Co_{0.05}O_{2-\delta}$

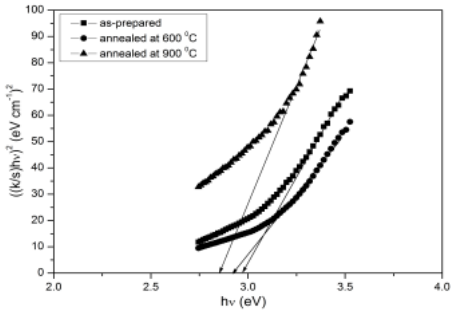

(h) $Ce_{0.9}Co_{0.1}O_{2-\delta}$

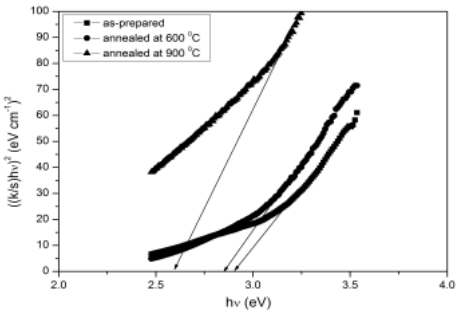

(i) $Ce_{0.85}Co_{0.15}O_{2-\delta}$

Figure 4.7: Tauc plots showing direct band gap energy for iron, aluminium and cobalt doped ceria nanocrystals.

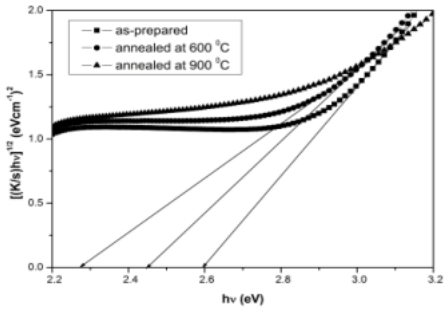

(a) $Ce_{0.95}Fe_{0.05}O_{2-\delta}$

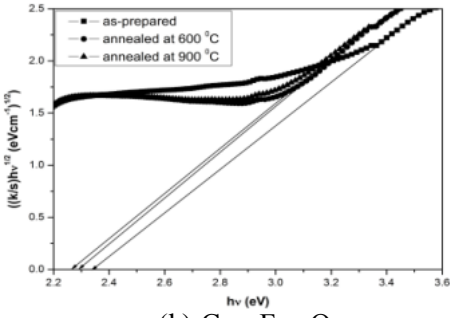

(b) $Ce_{0.9}Fe_{0.1}O_{2-\delta}$

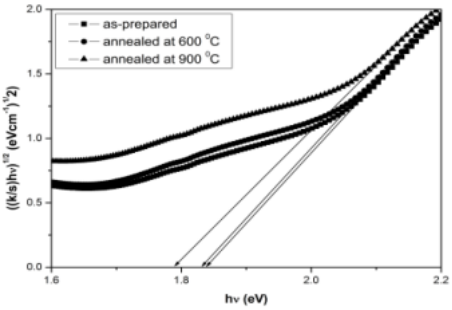

(c) $Ce_{0.85}Fe_{0.15}O_{2-\delta}$

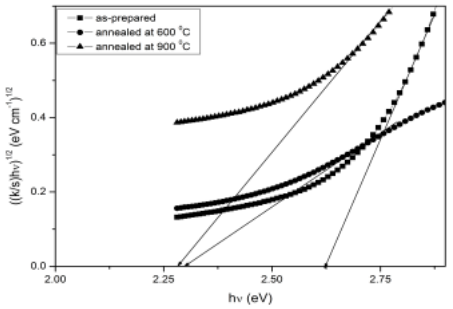

(d) $Ce_{0.95}Al_{0.05}O_{2-\delta}$

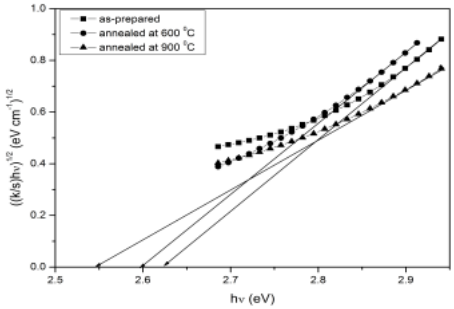

(e) $Ce_{0.9}Al_{0.1}O_{2-\delta}$

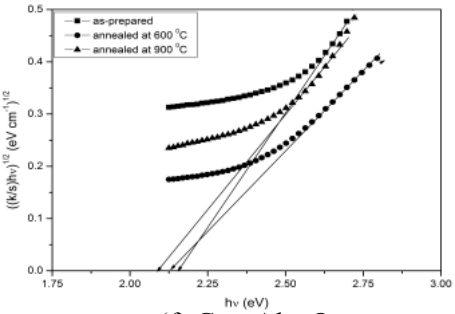

(f) $Ce_{0.85}Al_{0.15}O_{2-\delta}$

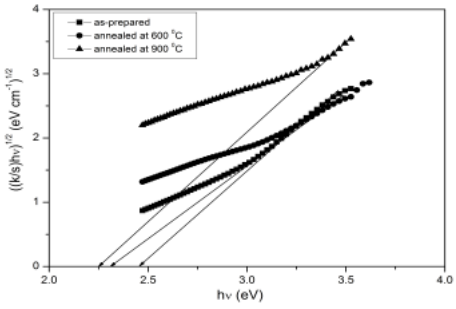

(g) $Ce_{0.95}Co_{0.05}O_{2-\delta}$

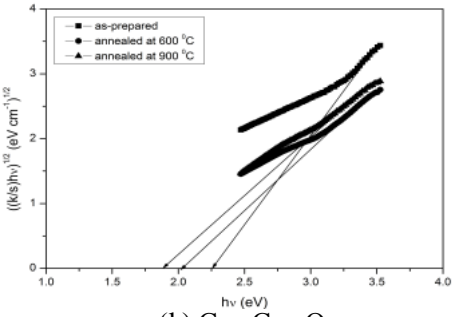

(h) $Ce_{0.9}Co_{0.1}O_{2-\delta}$

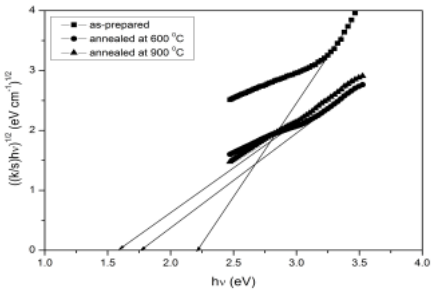

(i) $Ce_{0.85}Co_{0.15}O_{2-\delta}$

Figure 4.8: Tauc plots showing indirect band gap energy of iron, aluminum and cobalt doped ceria nanocrystals

Table 4.2: Variation of direct and indirect band gap energies with annealing temperature.

sample		Direct-Band gap(eV)	Indirect-band gap(eV)
$Ce_{0.95}Fe_{0.05}O_{2-\delta}$	As-prepared	3.14	2.60
	Annealed at 600 ^{0}C	3.06	2.51
	Annealed at 900 ^{0}C	3.05	2.28
$Ce_{0.90}Fe_{0.10}O_{2-\delta}$	As-prepared	2.94	2.34
	Annealed at 600 ^{0}C	2.91	2.29
	Annealed at 900 ^{0}C	2.57	2.26
$Ce_{0.85}Fe_{0.15}O_{2-\delta}$	As-prepared	2.86	1.85
	Annealed at 600 ^{0}C	2.82	1.84
	Annealed at 900 ^{0}C	2.30	1.78
$Ce_{0.95}Al_{0.05}O_{2-\delta}$	As-prepared	3.20	2.75
	Annealed at 600 ^{0}C	3.10	2.67
	Annealed at 900 ^{0}C	3.08	2.59
$Ce_{0.90}Al_{0.10}O_{2-\delta}$	As-prepared	3.19	2.61
	Annealed at 600 ^{0}C	3.08	2.60
	Annealed at 900 ^{0}C	3.07	2.54
$Ce_{0.85}Al_{0.15}O_{2-\delta}$	As-prepared	3.18	2.15
	Annealed at 600 ^{0}C	3.05	2.12
	Annealed at 900 ^{0}C	3.01	2.09
$Ce_{0.95}Co_{0.05}O_{2-\delta}$	As-prepared	3.12	2.46
	Annealed at 600 ^{0}C	3.00	2.32
	Annealed at 900 ^{0}C	2.52	2.25
$Ce_{0.90}Co_{0.10}O_{2-\delta}$	As-prepared	2.97	2.26
	Annealed at 600 ^{0}C	2.93	2.02
	Annealed at 900 ^{0}C	2.85	1.89
$Ce_{0.85}Co_{0.15}O_{2-\delta}$	As-prepared	2. 94	2.25
	Annealed at 600 ^{0}C	2.83	1.77
	Annealed at 900 ^{0}C	2.60	1.59

The ultra violet radiation reaching the earth's atmosphere consists of UV type B sub range (UVB, 290-320 nm) and the UV type A sub range (UVA, 320-400 nm). Theses radiations are the major cause of skin cancers. For the filtration of UVB, nanostructured TiO_2 is being used in sunscreen cosmetic products. But for the filtration of UVA, there are no suitable materials. The need for new materials capable of filtering the UVA radiation has enhanced extensive research in this direction [9]. With a band gap of 3.16 eV, good transparency in visible region, and no known toxicity, nanostructure ceria can hence be a promising inorganic material for UV filtering applications in sunscreen cosmetics. Present studies show that nanostructured doped ceria has peak UV absorption at 320 nm and hence can be used as an efficient UV filter for the UV A radiations.

The room temperature photoluminescence (PL) spectra of as-prepared iron, aluminium and cobalt doped CeO_2 nanoparticle samples are recorded under the excitation wavelength of 325 nm and are shown in figure 4.9 (a-c). The addition of trivalent ions Fe^{3+} and Al^{3+} and divalent ion Co^{2+} introduces oxygen vacancies in the CeO_2 nanoparticles. The majority of luminescence peaks produced in these doped samples are due to the presence of the oxygen vacancies.

In these doped ceria emission peaks located at 421, 440, 452, 470, 483, 494 and 533 can be clearly observed. The emission peak at 371 nm can be related to the hopping from the localized Ce 4f state to the O 2p valence band. The emission peaks ranging from 400 nm to 500 nm can be related to the hopping from different defect levels to the O2p level [21]. These weak blue green emissions are possible due to the surface defects in the CeO_2 nanoparticles. A low intense green emission is also observed at around 533 nm, possibly due to low density of oxygen vacancies incorporated in the sample

[22]. The most intense peak observed at 470 nm can be related to the presence of abundant defect states, which helps in fast oxygen transportation.

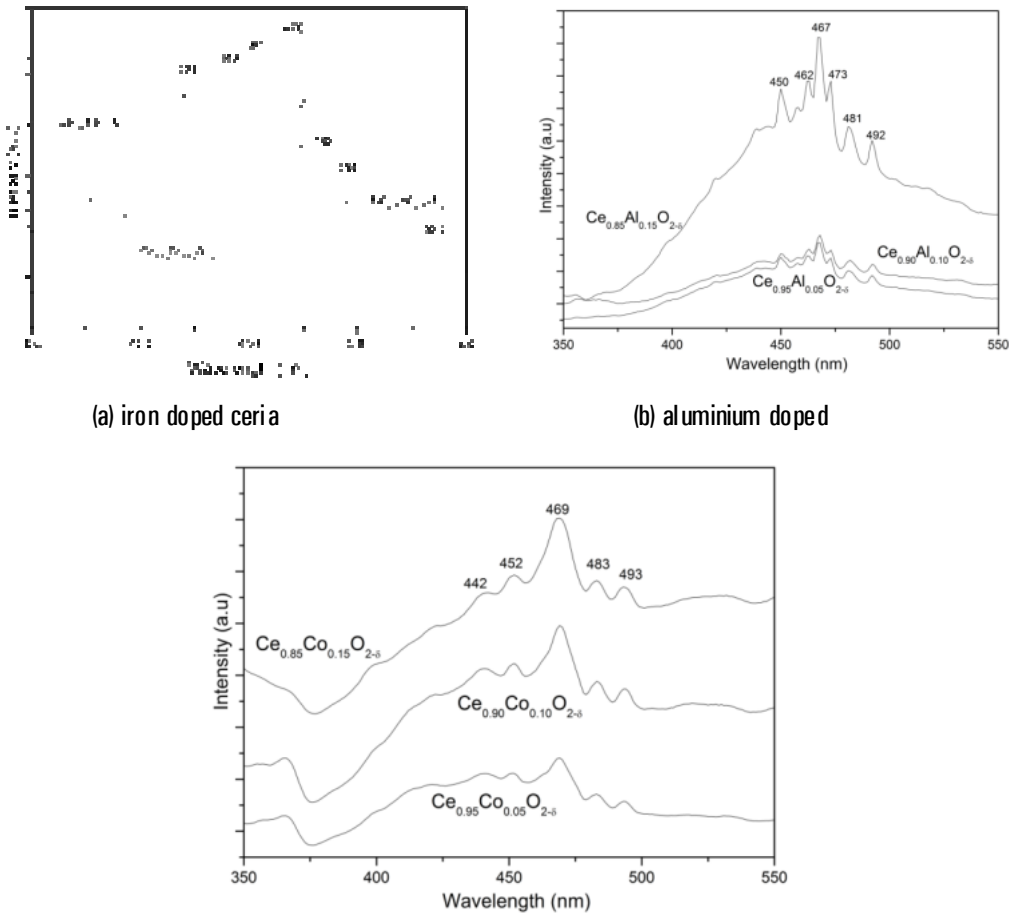

(a) iron doped ceria

(b) aluminium doped

(c) cobalt doped

Figure 4.9: PL spectra of doped ceria

In the aluminium doped ceria, the most intense peak is slightly shifted to higher wavelength region. In cobalt doped ceria, the peaks are found to be broadened. A large number of defect peaks can be observed in iron doped ceria compared to aluminium and cobalt doped PL spectra. The intensity of PL peaks decreases with concentration of iron due to quenching effect of iron whereas, it increases with concentration of aluminum and cobalt.

4.3. Conclusion

Nanocrystalline iron, aluminum and cobalt doped cerium oxide nanoparticles are prepared by chemical precipitation method using optimum conditions. The prepared samples are air annealed at 600 ^{0}C and 900 ^{0}C. XRD and TEM studies confirm the cubic phase $Ce_{1-x}Fe_xO_{2-\delta}$, $Ce_{1-x}Al_xO_{2-\delta}$ and $Ce_{1-x}Co_xO_{2-\delta}$ nanocrystalline particle formation. Particle size increases with increase in annealing temperature and lattice parameter decreases. FTIR studies show the existence of Ce, Fe, Al and O bonds very clearly. The optical absorption studies of the doped ceria samples show that the samples can be used as efficient UV filters for the UV A radiations. One of the highlights of the present investigation is the identification of doped ceria as a promising non toxic inorganic material for UV filtering applications in sunscreen cosmetics. Due to the size effect, both direct and indirect band gap energies are found to decrease with increase in particle size. Due to the band tailing effect, both direct and indirect band gap energies are found to decrease with increase in doping concentrations. PL spectra show the presence of the abundant defect states due to the addition of di or tri valent cation in ceria lattice.

References

[1] G Li, R L Smith, H Inomata, J. Am. Chem. Soc. 123 (2001) 11091

[2] B Matovic, Z Dohcevic-Mitrovic, M Radovic, Z Brankovic, G Brankovic, S Boskovic, Z V Popovic, J. Power Sources 193 (2009) 146

[3] D A Anderson, S I Simak, N V Skorodumova, I A Abrikosov, B Johansson, PNAS 83 (1996) 1

[4] T Dhannia, S Jayalekshmi, M C Santhosh Kumar, T Prasada Rao, A Chandra Bose, J. Phys. Chem. solids, 71 (2010) 1020

[5] T Dhannia, S Jayalekshmi, M C Santhosh Kumar, T Prasada Rao, A Chandra Bose, J. Phys. Chem. solids, 70 (2009) 1443

[6] H Lv, H Tu, B Zhao, Y Wu, K Hu, Solid State Ionics 177 (2007) 3467

[7] B D Cullity, S R Stock, in: Elements of X-RAY Diffraction-third ed., Prentice Hall, New Jersey (2001)

[8] A Gayen, K R Priolkar, A K Shukla, N Ravishankar, M S Hegde, Mater. Res. Bull. 40 (2005) 421

[9] L Truffault, M Ta, T Devers, K Konstantinov, V Harel, C Simmonard, C Andreazza, I P Nevirkovets, A Pineau, O Veron, J Blondeau, Mat. Res. Bull. 45 (2010) 527

[10] Y He, B Yang, G Cheng, Mat. Lett. 57 (2003)1880

[11] C Hu, Z Zhang, H Liu, P Gao, Z L Wang, Nanotechnology 17 (2006) 5983

[12] M Yan, W Wei, N Zuoren, J. Rare earths 25 (2007) 53

[13] K Nakamoto, Infrared and Raman Spectra of Inorganic and Coordination Compounds: part-A; Theory and Application in Inorganichemistry, 5th edn, John Wiley & Sons, New York (1997)

[14] M G Sujana, K K Chattopadyay, S Anand, Appl. Surf. Sci. 254 (2008) 7405

[15] A Tiwari, V M Bhosle, S Ramachandran, N Sudhakar, J Narayanan, S Budak, A Gupta, Appl. Phys. Lett. 88 (2006) 142511

[16] L Djellala, A Bougueliab, H M Kadi, M Trarib, Sol. Energy Mat. Solar cells 92 (2008) 594

[17] C Liu, L Luo, X Lu, Kinetics and Catalysis 49 (2008) 676

[18] S Sathyamurthy, K J Leonard, R T Dabestani, M Parans Paranthaman, Nanotechnology 16 (2005) 1960

[19] M K Hudait, P Modak, S B Krupanidhi, Mater. Sci. Engg. B 56 (1999)1

[20] Y Pan, M Kleefstra, Semicond. Sci. Tech. 5 (1990)312

[21] S Phoka, P Laokul, E Swatsitang, V Promarak, S Seraphin, S Maensiri, Mater. Chem. Phys. 115 (2009) 423

[22] P Patsalas, S Logothetidis, Phys. Rev. B 68 (2003) 035104

Chapter 5

THERMAL AND MAGNETIC PROPERTIES OF CERIA AND DOPED CERIA NANOCRYSTALS

Contents

5.1. Introduction

Diluted magnetic semiconductors (DMS) are currently being explored with a strong drive to find room temperature ferromagnetic materials (RTFM) for possible technological applications. DMS are experimentally obtained by doping the oxide matrix with a small amount of magnetic transition metal ions such as Fe^{3+}, Co^{2+}, Mn^{3+} etc. This procedure may introduce ferromagnetism in otherwise non magnetic materials and open up feasibility of applications in spintronics and magneto optical devices [1]. Spintronics has vast potential in the storage, processing, transmission of digital information and optical and magnetic sensors. Many promising compounds such as: Transition Metals (TM) doped ZnO, TiO_2, CeO_2 and HfO_2 have been observed to show RT-FM, but intrinsic origin of the FM is still under debate. Therefore, these controversial results give an indication that FM in DMS is very sensitive to preparation methods and preparation conditions. High curie temperature (T_c) FM observed in TM doped insulating oxide points towards a mechanism of oxygen vacancy mediated FM so called F-Centre exchange coupling (FCE) instead of the carrier induced FM. Since insulating

materials have no free carriers, high temperature FM is attributed to the oxygen vacancies. In FCE mechanism an electron is trapped in oxygen vacancy which acts as a coupling centre, via which doped magnetic ions align in ferromagnetic order. However, in most of the magnetic semiconductor doped magnetic ions exhibit very low solubility in the host matrix and the origin of FM in some of the compounds has been attributed to the magnetic impurities. Therefore, there is a great need of the host matrix that has high solubility of magnetic ions to form thermodynamically stable magnetic semiconductor [2].

Most of the room temperature ferromagnetics -DMS materials discovered so far have noncubic crystal symmetry. The RTFM in cubic systems will facilitate the integration of spintronic devices with advanced silicon based microelectronic devices. Among the materials with cubic symmetry, cerium oxide is an interesting candidate for advanced multifunctional devices. The recent discovery of RTFM in pure and/or doped CeO_2 nanoparticles and thin films give realization of future spintronic devices [3].

CeO_2 is one of the most important transparent rare earth oxides which are endowed with high dielectric constant. CeO_2 is used in variety of applications such as a buffer layer for silicon on insulator devices and as a high k- dielectric material in capacitors. These applications make CeO_2 a good matrix to develop FM. Therefore, the origin of RT-FM in CeO_2 makes it a potential candidate for use in novel multifunctional devices [3]. In the present investigation vibrating sample magnetometer (VSM) measurements were carried out on ceria and doped ceria nanocrystals to understand the magnetic properties.

Thermo-gravimetric analysis (TGA) is a type of testing performed on samples that determines the changes in weight in relation to change in temperature. TGA is the act of heating a mixture to a high enough temperature so that some of the components decompose into a gas, which dissociates into the air. It is a process that utilizes heat and stoichiometry ratios to determine the percent by mass ratio of a solute. TGA is commonly employed in research and

testing to determine characteristics of materials to determine degradation temperatures, absorbed moisture content of materials, the level of inorganic and organic components in materials, decomposition points of explosives, and solvent residues.

This chapter reports the investigations on the thermal and magnetic properties of as-prepared cerium oxide and doped cerium oxide nanoparticles with the variation in doping concentration and annealing conditions. Thermal properties are investigated using TGA. Magnetic properties are explained based on the room temperature VSM measurements.

5.2. Experimental techniques

5.2.1. Synthesis

The synthesis of cerium oxide and doped cerium oxide (iron and cobalt) nanoparticles was carried out by hydrolysis assisted precipitation technique, which are described in chapter 3 and 4 in detail.

5.2.2. Characterizations

Thermo-gravimetric Analysis (TGA) was done on a SIINT Exstar 6200 TGA/DTA instrument. Samples were heated to 1000 ^{0}C at a scan rate of 10 ^{0}C per minute in nitrogen atmosphere. Magnetic measurements were carried using a Lakeshore 7404 vibrating sample magnetometer (VSM).

5. 3. Results and discussion

Figures 5.1 to 5.3 show the TGA curves of cerium oxide and doped cerium oxide nanocrystals. The thermal analysis has been carried out from room temperature to 1000 ^{0}C with a heating rate of 10 ^{0}C/minute in nitrogen atmosphere. The TGA curve exhibits very less weight loss upto 250 ^{0}C, due to losses of moisture and trapped CO_2 [4]. Almost no weight loss could be observed from 250 ^{0}C to 1000 ^{0}C, suggesting the formation of crystalline CeO_2 as a decomposition product, as confirmed by XRD and FT-IR studies explained in chapter 4.3.

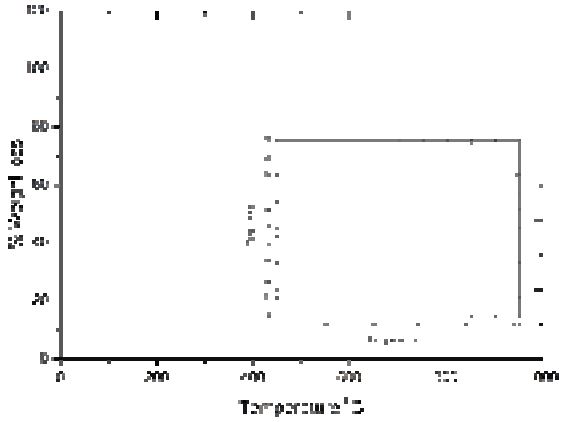

(a) as-prepared

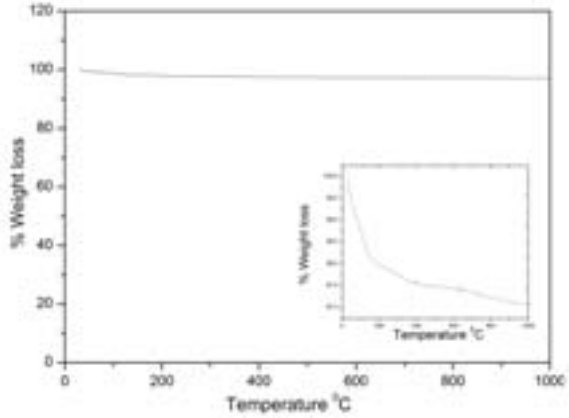

(b) annealed at 600 ^{0}C

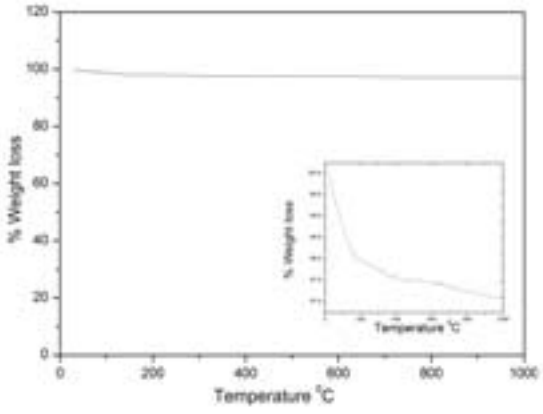

(c) annealed at 900 ^{0}C

Figure 5.1: Variation of % weight loss with temperature in cerium oxide nanoparticles

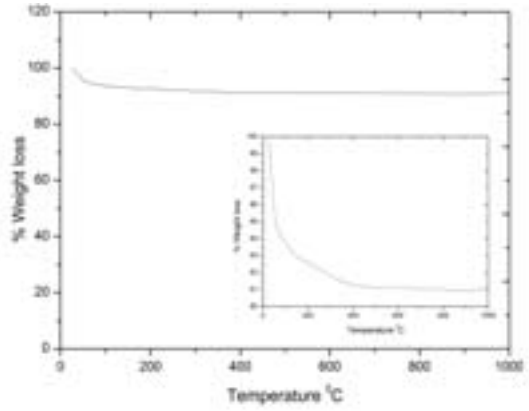

(a) as-prepared

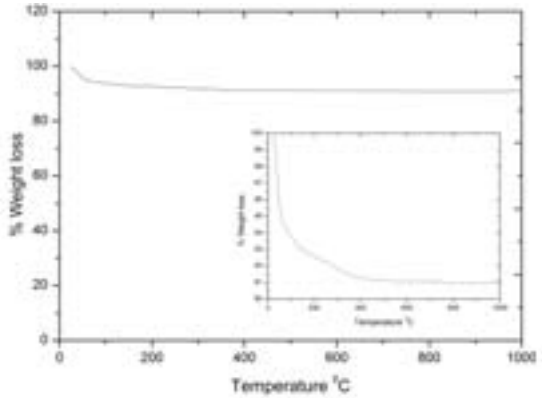

(b) annealed at 600 °C

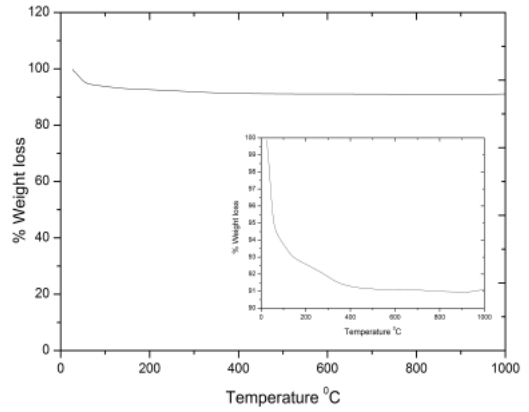

(c) annealed at 900 °C

Figure 5.2: Variation of % weight loss with temperature in iron doped cerium oxide nanoparticles

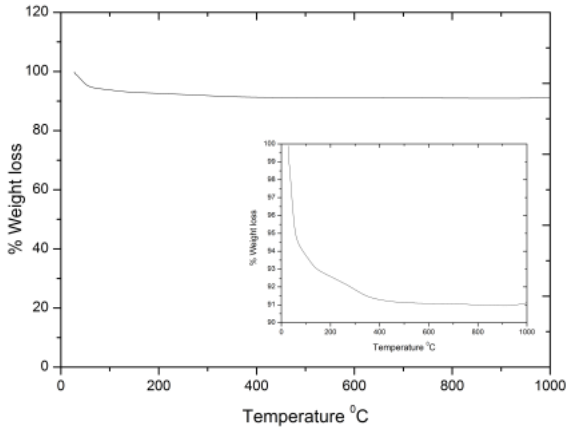

(a) as-prepared

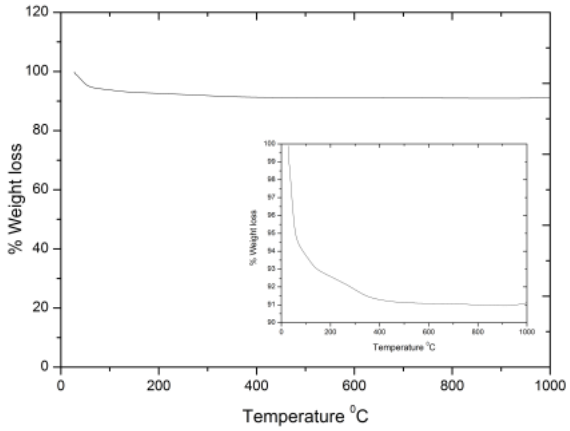

(b) annealed at 600 ^{0}C

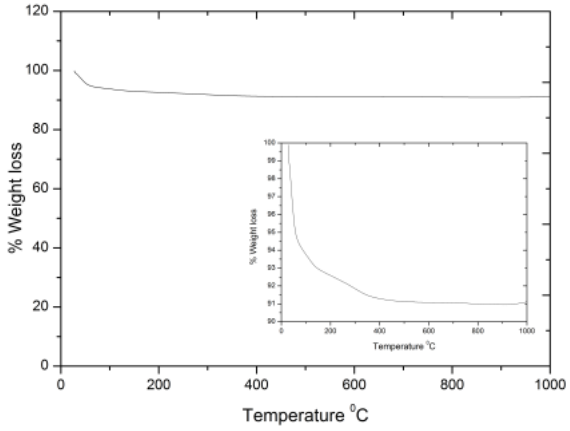

(c) annealed at 900 ^{0}C

Figure 5.3: Variation of % weight loss with temperature in cobalt doped cerium oxide nanoparticles

The magnetic properties of CeO_2 nanocrystals are evaluated by measuring the field dependence of magnetization at room temperature. Figure 5.4(a) shows the room temperature magnetization curves of CeO_2 in the as-prepared and annealed conditions. In this figure, CeO_2 appears to be diamagnetic. However, on close examination (Figure 5.4 (b)) room temperature ferromagnetism can be observed in these figures which are characterized by a closed hysteresis loop. The curves are composed of two parts: at lower field (Hc< 3000 Oe), the curve exhibits magnetic hysteresis with the remanent magnetization (Mr) of 0.010 emu/g and a coercivity of 198 Oe, whereas at higher field (Hc> 3000 Oe), the curve shows diamagnetic behavior. These results indicate the presence of a ferromagnetic component that is overlapped with a diamagnetic one for the CeO_2 nanocrystals at room temperature. Here, the preparation method involves only cerium chloride and ammonia, so it does not involve any magnetic element and therefore the possibility of contamination of magnetic impurities is negligible.

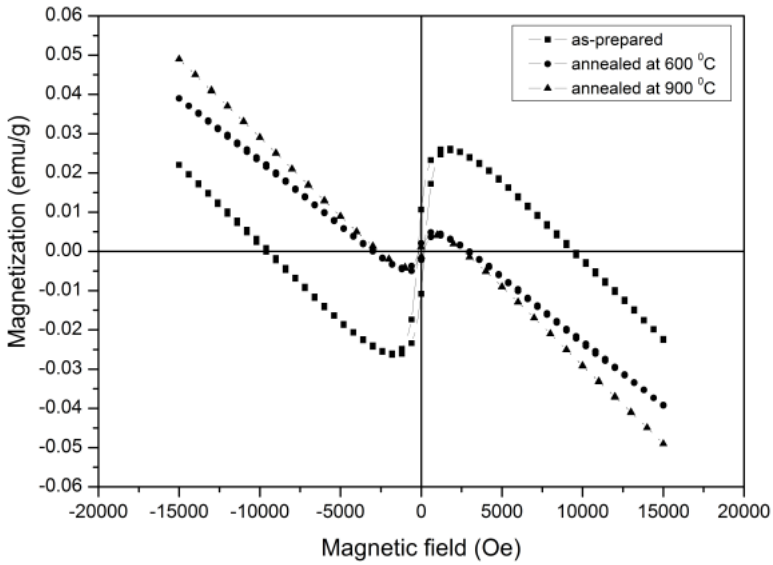

Figure 5.4: (a) Hysteresis loops for CeO_2 nanoparticles

The mechanism of the observed ferromagnetism and its explanations are very much controversial for undoped cerium oxide system. The FM in these insulating materials challenges the carrier induced FM mechanism and strongly support the F center mediated exchange mechanism for diluted ferromagnetism [5].

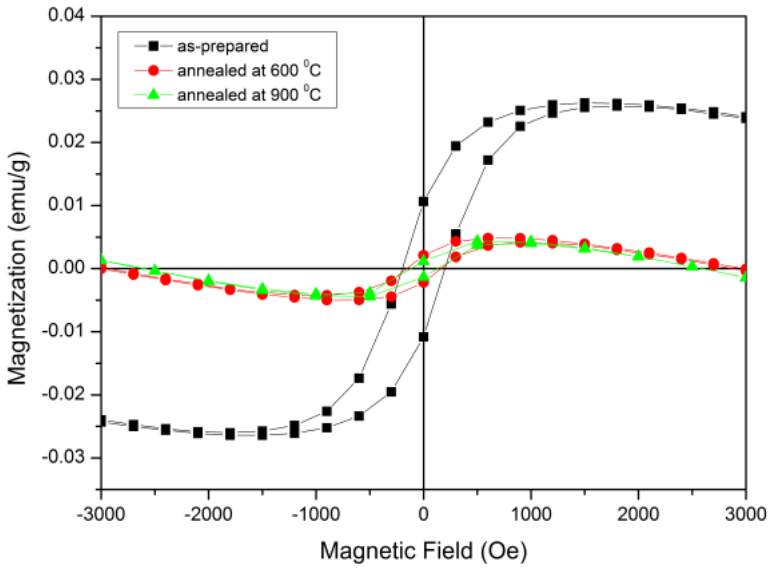

Figure 5.4: (b) Hysteresis loops for CeO_2 nanoparticles

The origin of ferromagnetism in CeO_2 is assumed to be resulting from the oxygen vacancies at the surface of the nanoparticles [6]. Ideal CeO_2 is Ce^{3+} free and therefore is diamagnetic because of the absence of magnetic moments for Xe-and Ne-like closed-shell electronic configuration of Ce^{4+} and O^{2-} respectively. According to the traditional ferromagnetic theory, the appearance of ferromagnetism might be correlated to the interaction between the 3d and/or 4f open-shell electrons. So the oxygen vacancies and defects at the surface/interface dominate the mechanism for room-temperature ferromagnetism. For very small nanocrystals defects may be expelled from the internal bulk lattice to the surfaces by a self purification process. These defective surfaces always show high surface energies and as a result, almost all

nanocrystals have a strong capacity of adsorption species on the surface to reduce the surface energies. These adsorption species would act as the donors of electrons or holes. And these oxygen vacancies and defects at the surfaces of nanoparticles can easily trap the electrons or holes than the bulk vacancies. The surface/interface atoms may have the feature of low coordination number, which could also effectively reduce the distance of defects to the effective magnetic exchange interaction scale. So this magnetic exchange interaction between the high-spin state vacancies gives rise to the ferromagnetism in cerium oxide nanocrystals [7]. The ferromagnetism has been reported as an intrinsic property in a number of undoped and nonmagnetic insulating oxides. Actually a deeper insight into complex defect physics is necessary to understand the ferromagnetic behavior in these systems. From the figure 5.4 it is seen that the annealed cerium oxide samples show a considerable reduction in ferromagnetic behavior, which almost become diamagnetic at higher annealing temperature (900 ^{0}C). This can be understood from the fact that the filling up of the oxygen vacancies due to air annealing, which destroy the ferromagnetic ordering and hence magnetic exchange interaction in the nanocrystalline samples [8].

Figure 5.5 (a and b) shows the magnetization curves of 5% and 15% iron doped CeO_2 in the as-prepared and annealed conditions. The hysteresis loops indicate that all the samples show clear RTFM. In the sample with lower iron concentration (5%) there is also a linear paramagnetic component in the unannealed sample, suggesting that not all of the dopant atoms participate in the FM ordering. The Fe ions enter substitutionally in ceria lattice but certain amount of Fe ions remain in the interstitial sites too. These isolated Fe ions are not magnetically ordered, which can bring about paramagnetic behavior [8]. When doping CeO_2 with divalent or trivalent ions, an oxygen vacancy is

formed to ensure charge neutrality. So the ions that enter substitutionally in place of Ce^{4+} in lattice produce oxygen vacancies. These oxygen vacancies are responsible for the FM behavior in these samples [9].

The key issue is to understand the role of oxygen vacancies in the FM in doped ceria. The exchange mechanisms that could establish the ferromagnetism is Ruderman-Kittel-Kasuya-Yosida (RKKY) interactions and/or bound magnetic polarons (BMP). The former requires a metallic system, whereas the latter can be observed in semiconducting/insulating materials. There is a sub category of BMP theory named F-centre exchange (FCE). This mechanism has been applied to explain the room temperature FM in magnetic insulators [10].

The FCE mechanism for FM due to the presence of oxygen vacancies can be summarized as follows. There are three possible charge states of an oxygen vacancy. These are (a) F^{2+} center with no trapped electrons, (b) F^{+} centre with one trapped electron and (c) F^{0} centre with two trapped electrons. F^{0} centre charge states are in a singlet (S=0) state and form a shallow donor level or lie above the conduction band edge. This can only mediate weak anti ferromagnetic (AFM) exchange between magnetic dopants. In some cases, the impurity band, which is formed due to the F^{0} centre states can overlap with the conduction band of host oxide (4s band). This favors the FM, but its strength is very weak. In contrast to this, singly occupied vacancies (F^{+} centre) lie deep in the gap and favor a strong FM [10].

In the sample with lower iron concentration (5%), the presence of a diamagnetic component in addition to the ferromagnetic one is observed in the annealed samples in the magnetization curve. The magnetization value of the 5% iron doped ceria is observed to be less than pure ceria. The reduction in the magnetization is possibly due to the presence of nearby interstitial Fe ions which, in the absence of oxygen vacancy, can interact antiferromagnetically by

the super exchange interaction. Another possible source of AFM interaction can be the existence of oxygen vacancies with two trapped electrons. These vacancies are in a singlet state can mediate weak AFM interaction between nearby magnetic dopants. From the optical absorption studies it is observed that there is a peak around 560 nm in all the iron doped CeO_2 samples which corresponds to the presence of antiferromagnetic phase αFe_2O_3. The intensity of this peak is found to increase with increase in doping concentration of iron. Although the magnetization curves of iron doped ceria samples show clear RTFM behavior, the curves don't saturate even for a magnetization field of 16000 Oe. The presence of the antiferromagnetic αFe_2O_3 phase in the iron doped ceria samples could be the prime reason for the observed unsaturation of magnetization curves. The magnetic behavior of Fe doped ceria presents a subtle interplay of the competing magnetic interactions: ferromagnetic FCE coupling strongly dependent on the valence state of Fe dopant, AFM interaction and paramagnetism due to isolated Fe ions randomly distributed in host matrix [8].

In these samples, every Fe^{3+} ions in low spin state ($3d^5$) has one unpaired electron spin which can participate in ferromagnetic ordering. Therefore when Fe^{3+} ions enter substitutionally in ceria lattice besides an increase in vacancy concentration one can expect more ferromagnetic Fe^{3+}-V_o-Fe^{3+} groups where V_o stands for oxygen vacancy. Thus in the 15% iron doped ceria the higher concentrations of Fe^{3+}-Vo-Fe^{3+} and Ce^{3+}- Vo- Ce^{3+} complexes are responsible for ferromagnetic coupling and the observed higher magnetization, where V_o stands for oxygen vacancy. In this sample, both for the unannealed and annealed cases (600 and 900 ^{0}C) the presence of diamagnetic component is not observed. The unannealed 15 % iron doped sample shows the highest magnetization which is around 4 X 10^{-2} emu/g. Both the lack of

magnetic saturation (increase of slope at high field) and high coercivity (Hc =1164 Oe) indicate high magnetic anisotropy in the 15% Fe-doped cerium oxide nanocrystals [11].

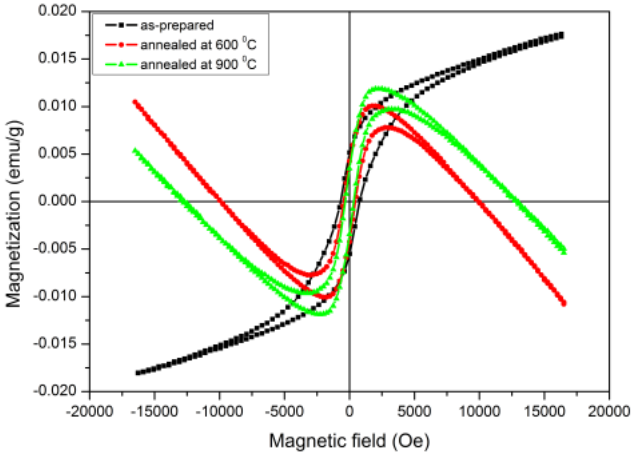

Figure 5.5: (a) Hysteresis loops for $Ce_{0.95}Fe_{0.05}O_{2-\delta}$

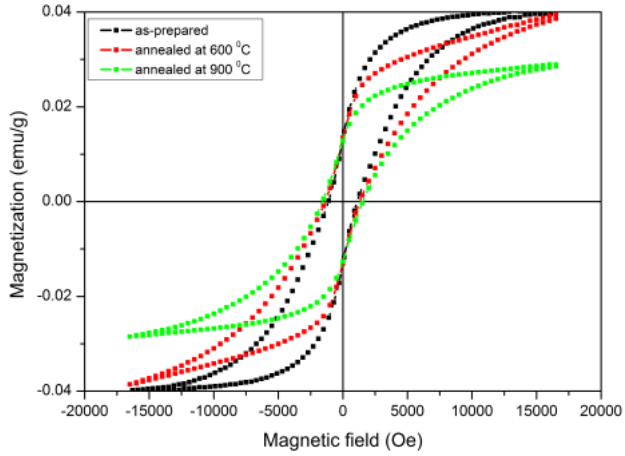

Figure 5.5: (b) Hysteresis loops for $Ce_{0.85}Fe_{0.15}O_{2-\delta}$

From figure 5.5(b) it is obvious that annealing degrades FM properties. With annealing the particles grow and surface to volume ratio decreases followed by decrease in Vo concentration. Hence oxygen vacancy induced FM

should be weakened [8]. The remanence magnetization (Mr) changes from 0.014 emu/g to 0.012 emu/g. The coercivity increases with annealing temperature from 1164 Oe to 1589 Oe. The increase of coercivity by increasing the calcination temperature can be mainly attributed to the enhancement of crystallite size within the single domain region.

Figure 5.6 (a and b) shows the magnetization curves of 5% and 15% cobalt doped CeO_2 in the as-prepared and annealed conditions. The hysteresis loops indicate that all the nanoparticles have clear RTFM. The RTFM in Co doped samples also can be explained on the basis of FCE mechanism. The Cobalt ions that entered substitutionally in place of Ce^{4+} in the lattice produce oxygen vacancies and FM behaviour. Each oxygen vacancy site easily traps an electron from adsorption species forming an F centre. The exchange interaction between the Co^{2+} ions and singly charged vacancy enables indirect FM coupling known as F-centre exchange coupling (FCE). Magnetization is not saturated due to the presence of antiferomagnetic or paramagnetic components [8].

When a divalent or trivalent Co ion is substituted in CeO_2, an oxygen vacancy is naturally formed to ensure charge neutrality. An oxygen vacancy in CeO_2 traps an electron to form F-centers. This F-centre with two Co ions constitutes a Co^{2+} - Vo- Co^{2+} group, where Vo denotes the oxygen vacancy. The electron trapped in the oxygen vacancy occupies an orbital which overlaps the d shells of both Co ion neighbours. The radius of the electron orbital which overlaps the d shells of both Co ion neighbours. Based on Hund's rule and Pauli's exclusion principle, spin orientations of the trapped electrons and the two neighbouring Co ions should be parallel in the same direction, thus ferromagnetic ordering is achieved [3,12].

Co ions are randomly distributed in the CeO_2 host matrix and can be approximately divided into three subsets. One subset of Co is far apart from other Co ions, thus the spins of these isolated Co ions are completely free and the magnetization follows a simple PM behavior. In second set of ions, Co ions have a smaller separation from each other and they are affected by FCE interactions, leading to a typical FM behavior. Meanwhile, there must also be some Co ions that have nearest neighbor Co ions (paired Co). The paired Co ions mediated by one oxygen ion are expected to have super exchange interaction with nearest neighbor Co ions thus giving rise to an antiferromagnetic behavior. When the Co content is small, the first and second subsets of Co ions dominantly coexist, thus a mixture of PM and FM is observed. As Co content increases, more Co ions are mediated by FCE interaction due to smaller distance between Co ions and the increase of concentration of oxygen vacancies. Therefore an increase of magnetization with Co content is reasonably observed in the CeO_2. With further increase of Co content, the number of the third subset of Co ions increases and the antiferromagnetic interactions quickly reduce the FM of Co doped CeO_2 powder. Clearly a competition between the magnetic properties resulting from three subsets of Co ions underlies the complex magnetic behavior in Co doped ceria nanoparticles [12]. Here magnetization value of Co doped ceria is less than pure CeO_2. This decrease of magnetization value with Co is ascribed by the name "paired Co". The paired Co ions via one oxygen ion give rise to an antiferromagnetic behavior by super exchange interaction. Therefore, there must be a critical density of both Vo defect and magnetic ions to establish the percolation threshold for long range FM order [5].

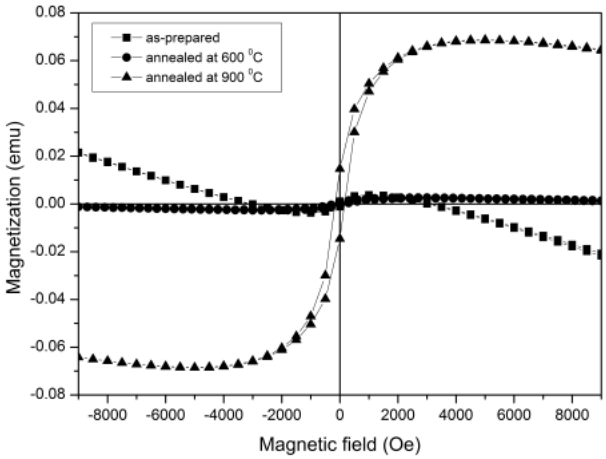

Figure 5.6: (a) Hysteresis loops for $Ce_{0.95}Co_{0.05}O_{2-\delta}$

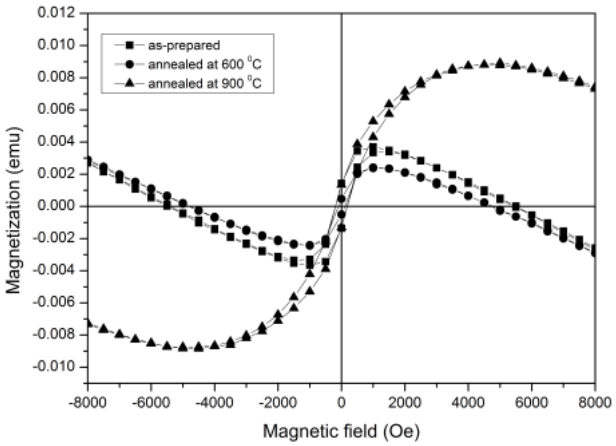

Figure 5.6: (b) Hysteresis loops for $Ce_{0.85}Co_{0.15}O_{2-\delta}$

The M-H curve of the 900 ^{0}C annealed sample shows a well defined hysteresis loop with a coercive field of ∽200 Oe and magnetisation of Ms∽0.07 emu/g. On annealing FM increases and saturation magnetization is observed in Co doped ceria due to high crystallinity and lower surface disorder. Annealing provides thermal energy and crystal lattice reconfirmation happens to form high quality nanocrystals. So FM increases because of lowering of surface spin disorder of larger magnetic nanoparticles [13, 14].

5.4. Conclusion

Room temperature ferromagnetism (RTFM) has been observed in nanocrystalline pure CeO_2, iron doped CeO_2 and cobalt doped CeO_2 powders, which are synthesised using a surfactant free, simple hydrolysis assisted chemical precipitation technique with cerium chloride and ammonia as precursors. The shape of the hysteresis loops indicates the presence of a ferromagnetic component that is overlapped with a diamagnetic one for the CeO_2 nanocrystals at room temperature. The origin of room temperature ferromagnetism in CeO_2 can be ascribed to the exchange interactions between localized electron spin moments resulting from the electrons trapped at the oxygen vacancies at the surface of the nanoparticles (FCE). The width of the hysteresis loops and coercivity decrease with increase in annealing temperature due to the decrease of oxygen vacancies upon annealing. The hysteresis loops in pure ceria show saturation behavior for both the as-prepared and annealed samples. The sample with lower iron concentration (5%) shows the presence of a diamagnetic component in addition to the ferromagnetic one in the magnetization curve. The reduction of magnetization in the 5% iron doped sample compared to pure ceria can be a consequence of the interplay of the competing magnetic interactions which are (1) the ferromagnetic FCE coupling which strongly depends on the valence state of Fe ions (2) the AFM interactions due to the isolated Fe ions randomly distributed in the host cerium oxide matrix and (3) paramagnetism due to the presence of α Fe_2O_3. Annealing the samples at 600 ^{0}C and 900 ^{0}C degrades the FM behavior in both the iron doped samples because of the decrease of oxygen vacancy concentration. In the 15% iron doped samples, the higher concentrations of Fe^{3+}-Vo-Fe^{3+} and Ce^{3+}-Vo- Ce^{3+} complexes are responsible for ferromagnetic coupling and the observed higher magnetization, where V_o stands for oxygen vacancy. In the Co doped samples

(both for 5% and 15%) the presence of a diamagnetic component in addition to the ferromagnetic one is observed in the magnetization curve of the unannealed samples. The magnetisation value of cobalt doped ceria is observed to be less than pure ceria due to the presence of "paired Co". The paired Co ions mediated by one oxygen ion give rise to an antiferromagnetic behaviour by super exchange interaction. In the 15% cobalt doped ceria the magnetization is less than that in the 5% Co doped ceria due to higher concentrations of paired cobalt ions and in both cases magnetization is less than pure ceria. In these samples, however magnetization increases with increase in annealing temperature due to lower surface spin disorder arising from better crystallinity of larger particles formed as a result of annealing. Thermal properties of pure ceria and transition metals (Fe and Co) doped ceria nanocrystals show negligibly small mass loss up to 1000 ^{0}C which establishes the excellent thermal stability of both the pure and doped ceria.

References

[1] T Fukumura, Y Yamada, H Toyosaki, T Hasegawa, H Koinuma, M Kawasaki, Appl. Surf. Sci. 223 (2004) 62

[2] S Kumar, Y J Kim, B H Koo, H Choi, C G.Lee, IEEE Transactions on Magnetic 45 (2009) 2439

[3] A Tiwari, V M Bhosle, S Ramachandran, N Sudhakar, J Narayanan, S Budak, A Gupta, Appl. Phys. Lett. 88 (2006) 142511

[4] S Phoka, P Laokul, E Swatsitang, V Promarak, S Seraphin, S Maensiri, Mater. Chem. Phys. 115 (2009) 423

[5] Q Wen, H Zhang, Y Song, Q Yang, H Zhu, IEEE Transactions on Magnetic 44 (2008) 2704

[6] A Sudaresan, R Bhargavi, N Rangarajan, U Siddesh, C N R Rao, Phys. Rev. B 74 (2006) 161306 (R)

[7] X Chen, G Li, Y Su, X Qiu, L Li, Z Zou, Nanotechnology 20 (2009) 115606

[8] Z D Dohcevic-Mitrovic, N Paunovic, M Radovic, Z V Popovic, B Matovic, B Cekic, V Ivaanovski, Appl. Phys. Lett. 96 (2010) 203104

[9] P C A Brito, D A A Santos, J G S Duque, M A Macedo, Physica B 405 (2010) 1821

[10] L R Shah, B Ali, H Zhu, W G Wang, Y Q Song, H W Zhang, S I Shah, J Q Xiao, J. Phys. Cond. Matt. 21 (2009) 486004

[11] D Peddis, N Yaacoub, M Ferretti, A Martinelli, G Piccaluga, A Musinu, C Cannas, G Navarra, J M Greneche, D Fiorani, J.Phys: Condens. Matter 23 (2001) 426004

[12] Q Wen, H Zhang, Y Song, Q Yang, H Zhu, J Q Xiao, J. Phys: Cond. Matt. 19 (2007) 246205

[13] D Gao, Z Zhang, J Fu, Y Xu, J Qi, D Xue, J. Appl. Phy. 105 (2009)113928

[14] M P Morales, S Veintemillas, M I Montero, C J Serna, Chem.Mater 11 (1999) 3058

Chapter
6

PREPARATION OF CERIA THIN FILMS BY SPRAY PYROLYSIS AND THEIR CHARACTERIZATIONS

Contents

6.1. Introduction

Thin film science has received tremendous attention in recent years because of numerous applications of films in diverse fields such as electronic industries, space science, solar energy utilization, optoelectronics, superconductivity, sensors and microelectronics. The use of materials in many technological applications has been realized through the use of thin films of these materials. Thus the development of any new material will have good application potential if it can be deposited in thin film form with the same properties. The advantageous properties of thin films include the possibility of tailoring the properties according to film thickness, small mass of the materials involved and high surface to volume ratio. Ceria films have been used for applications in optoelectronics, electrochromics, higher storage capacitor devices, UV blocking filters, silicon on insulator structures for microelectronics etc. Ceria films are very promising as buffer layers for high temperature superconductors because of their close match and similar thermal coefficients. The aim of the present work is to investigate the possibility of production of

high quality ceria films on glass substrates by spray pyrolysis method at lower substrate temperature.

Spray pyrolysis is an attractive thin film preparation method because it is inexpensive, easy when doping is required and can under optimal conditions, produce good quality films [1]. The optical properties of oxide films, such as transmittance and band gap energy, are critically dependent on the film thickness, its corresponding microstructure and surface morphology.

This chapter deals with the deposition of CeO_2 nanocrystalline thin films on soda lime glass substrates using spray pyrolysis method. The effect of film thickness on the microstructure, surface morphology, optical properties and magnetic properties has been investigated in detail. The search for RTFM in spray pyrolysed CeO_2 thin films also forms an integral part of the present investigations.

6.2. Experimental techniques

6.2.1. Preparation method

The spray pyrolysis is a cost effective and simple method for the deposition of thin films of metallic oxides. In this deposition technique, a starting solution, containing metal precursors, is sprayed by means of a nozzle, assisted by a carrier gas, over a hot substrate. When the fine droplets arrive at the hot substrate, the compounds in the precursor decompose to become a new chemical compound in solid state, which is then deposited on the substrate surface. All other byproducts are in the gaseous form, and are taken away by the carrier gas. In the present investigation, CeO_2 thin films of various thicknesses were deposited on soda lime glass substrates using the spray pyrolysis technique at a substrate temperature of 623 K. The substrates were cleaned in running water with an industrial detergent solution followed by acetone and deionized water. The substrates were finally cleaned with an ultrasonic bath for 30 minutes and dried in hot air oven. A solution of 0.1 M $CeCl_2.7H_2O$ was used as a precursor, prepared by dissolving the salt in

deionized water. The nozzle was at a distance of 20 cm from the substrate during deposition. The solution flow rate was held constant at 3 ml/min. Air was used as the carrier gas, at the pressure of 2 bar. When aerosol droplets arrive closer to the heated substrates, a pyrolytic process occurs and highly adherent CeO_2 thin films were deposited. Samples with different thickness were deposited under the same preparation conditions, only varying the deposition time. The films were deposited using Holmarc (India) automated spray pyrolysis unit.

6.2.2. Characterization techniques

The XRD patterns were recorded using Rigaku D/Max X-ray diffractometer. The optical measurements of the CeO_2 thin films were carried out at room temperature using Shimadzu UV-1700 Spectrophotometer in the wavelength range 300 to 1100 nm. The thickness was measured using Stylus profile meter. Photoluminescence measurements were carried out using a luminescence spectrometer (Jobin Yvon Flourimeter) at room temperature. Magnetic properties of films were investigated using Lakeshore 7404 vibrating sample magnetometer (VSM)

6.3. Results and discussion

In the present work CeO_2 thin films were deposited at various substrate temperatures and conditions to optimize the deposition conditions. All temperature below 573 K yielded powdery non-adherent films. When the substrate temperature was at 573 K adherent films could be deposited. But these films were found to be amorphous in nature. At a substrate temperature of 623 K (350 ^{0}C) highly crystalline thin films could be deposited by optimizing other deposition conditions like carrier gas pressure and flow rate. Figure 6.1 shows the XRD pattern of the CeO_2 thin films deposited at 573 K and 623 K. The films deposited at 573 K shows almost an amorphous nature from the XRD pattern. These films were whitish-yellow in color with very poor optical transmittance. The samples deposited at 623 K show the characteristic peaks at 2θ = 28.48, 32.96, 48.26 and 56.38, which are in good agreement with JCPDS file

No.81-0792. The X-Ray Diffraction patterns of the as prepared cerium oxide thin films with different thickness are shown in figure 6.2.

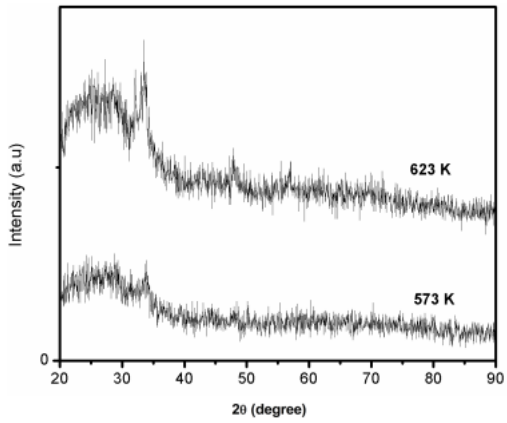

Figure 6.1: XRD patterns of the as-prepared cerium oxide thin films at 573 K and 623 K.

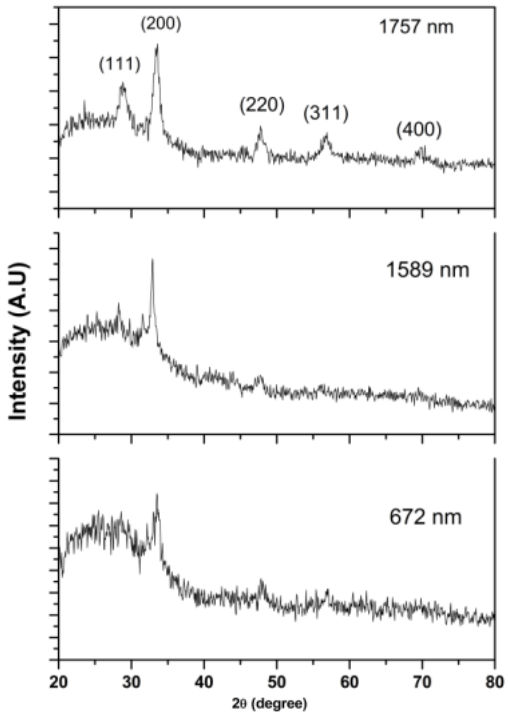

Figure 6.2: XRD patterns of the as-prepared cerium oxide thin films with different thicknesses at 623 K substrate temperature.

To describe the preferred orientation, the texture coefficient TC (h k l), was calculated using the following expression

$$TC\ (hkl) = \left(\frac{\frac{I_{(hkl)}}{I_{r(hkl)}}}{\left[\frac{1}{n} \sum \frac{I_{(hkl)}}{I_{r(hkl)}} \right]} \right) \qquad (1)$$

where I(hkl) is the measured relative intensity of a plane (hkl), I_0(hkl) is the standard intensity of a plane (hkl) taken from the JCPDS data and n is the number of diffraction peaks considered in the calculation [2]. It is clear from the definition that the deviation of texture coefficient from unity implies the film growth in preferred orientation. Texture coefficients calculated for (111), (200) and (220) planes are shown in the table 6.1. The higher value of TC indicates the preferred orientation of the films along that diffraction plane. This means that the increase in preferred orientation is associated with the increased number of grains along that plane [2]. The high value of TC along (200) plane indicates the maximum preferred orientation of the films along the (200) diffraction plane.

Table 6.1: Texture coefficient calculated for thin films of various thicknesses

Film thickness (nm)	TC (hkl)		
	(111)	(200)	(220)
672	--	1.53	0.46
1589	0.54	1.91	0.54
1757	0.42	2.03	0.53

According Baeur [3], there are two possible mechanisms; orientation due to nucleation and final growth orientation. Both of these result from the nucleation at the film/substrate interface. The initial orientation is favoured on smooth surface with the tendency of nuclei to develop a minimum free energy

configuration. The final growth orientation results from survival of nuclei having an energetically unstable plane parallel to the substrate surface among randomly oriented nuclei because of their different growth rates. This means, that, the growth orientation is developed into one crystallographic direction which is of the lowest surface energy. Then, the grains became larger as the film grows with lower surface energy density [3].

The XRD pattern of lower thickness film shows a random crystal orientation comparable to that of standard powder diffraction pattern of bulk material. It can be observed that the lower thickness film exhibits poor crystallinity. As the thickness increases, the peak intensity increases and become narrower indicating a better crystallinity. It is not the result of structural changes in the films, but the result of increase in the film thickness [4].

Grain sizes are calculated from XRD data using Scherrer's formula as given below [5].

$$\text{Average grain size } t_{xrd} = \frac{0.9\lambda}{\beta \cos\theta} \qquad (2)$$

where λ is the wavelength of the incident X-rays (0.15406 nm), β the FWHM and θ the diffraction angle. The calculated particle sizes and lattice parameters of the as-prepared ceria films from XRD spectra are shown in table 6.2. The grain size is found to change dramatically with film thickness. The average grain size increases with film thickness. As deposition time increases, the amount of solute reaching the surface of the substrate increases to form film and therefore the electrostatic interaction between solute particles becomes larger thereby increasing the probability of more solute particles to be gathered together forming a grain. Thus as the thickness increases, grain size also increases [4]. In order to understand the composition and presents of impurities

in the sample EDX spectra were recorded. Figure 6.3 shows the EDX spectra of ceria thin films. The EDX spectra show the presence of cerium and oxygen, confirming the purity of the films formed.

Table 6.2: Variation of grain size and lattice parameter of CeO_2 thin film

Thickness (nm)	Grain size (nm)	Lattice parameter (Å)
672	21	5.37
1589	32	5.37
1757	45	5.37

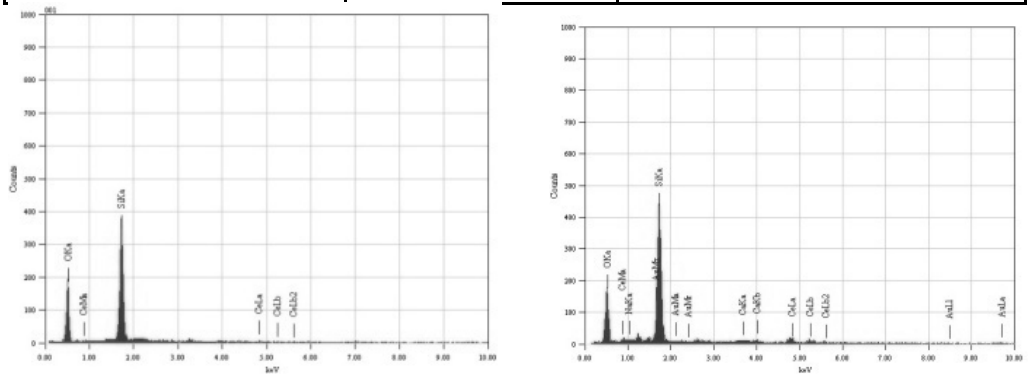

(a) 672 nm (b) 1589 nm

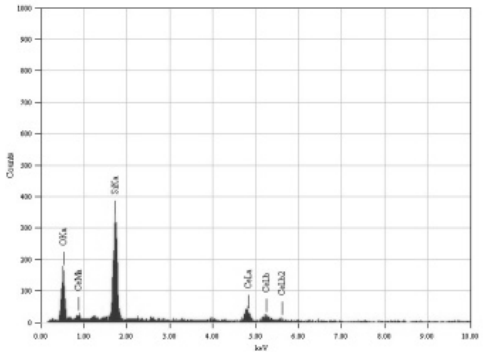

(c) 1757 nm

Figure 6.3: EDX of ceria thin films

Scanning electron micrograms (SEM) were recorded for the CeO_2 thin films with different thicknesses. The micrographs (figure 6.4) show uniform grain distribution when the film thickness is 672 nm. These micrographs show that the obtained films have good adherence to the substrates. As the film thickness increases, more growth occurs on the surface of the films and some of these grains grow as cubic crystallites on the surface of the films. The SEM results are in good agreement with XRD results and the change in crystalline size with film thickness is well in agreement with that found in other oxides [4].

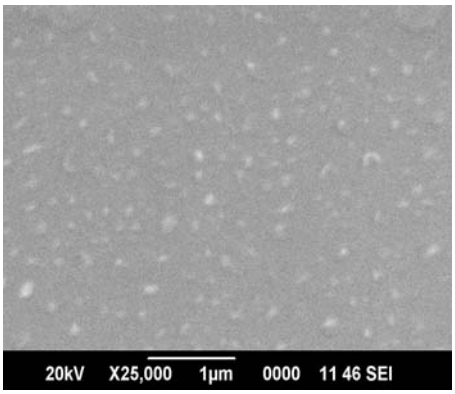

a) 672 nm

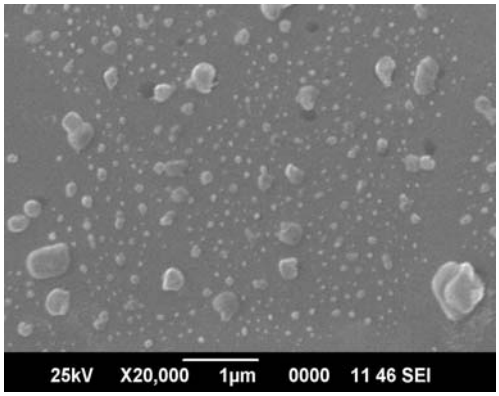

b) 1589 nm

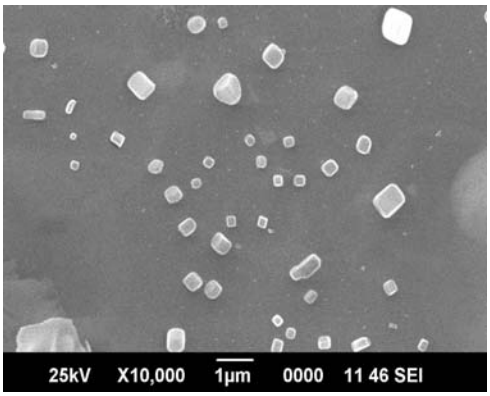

c) 1757 nm

Figure 6.4: SEM images of ceria thin films

Accurate knowledge of the absorption coefficient, optical band gap and refractive index of semiconductors is indispensable for the design and analysis of various optical and optoelectronic devices. It is possible to determine direct and indirect transitions occurring in the materials by optical absorption spectra. The transmittance data can be analyzed to determine optical constants such as refractive index, extinction coefficient and dielectric constant [6]. The optical properties of CeO_2 thin films are determined from transmission and reflection measurements conducted in the wavelength range of 300 nm to 1100 nm at room temperature. The variation of transmittance and reflectance of cerium oxide thin films of different thickness with wavelength is shown in figure 6.5. The sharp absorption edge for these films is around 350 nm in ultra violet region. CeO_2 films of thickness 672 nm exhibits a high transparency (above 80 %) in the visible region. The high transmittance is probably due to the existence of an interfacial layer with low refractive index between CeO_2 and glass [7]. The transmittance found to decrease with the increase of film thickness. This is attributed to the increase in film thickness, which subsequently increases the absorption.

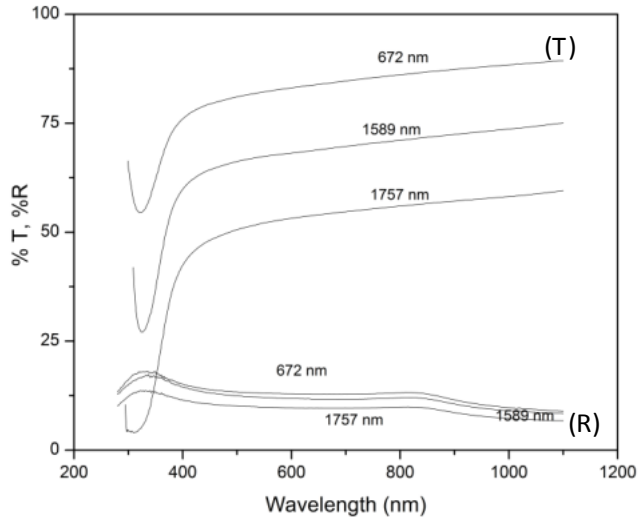

Figure 6.5: Variation of transmission and reflection of ceria thin film with wavelength

The transmission decreases sharply near the ultraviolet region due to the band gap absorption. Additionally, a shift of the absorption edge, proportional to the thickness values, towards lower energies is observed from the spectra. Absorption coefficient α is calculated from the transmission and reflection data using the following relation

$$\alpha = \frac{1}{t}\ln\left(\frac{1-R}{T}\right) \qquad (3)$$

where "t" is the film thickness and "T" is the transmittance and "R" is the reflectance of the film [3]. The variation of absorption coefficient with wavelength is displayed in figure 6.6. Absorption coefficient is found to decrease with increase in wavelength.

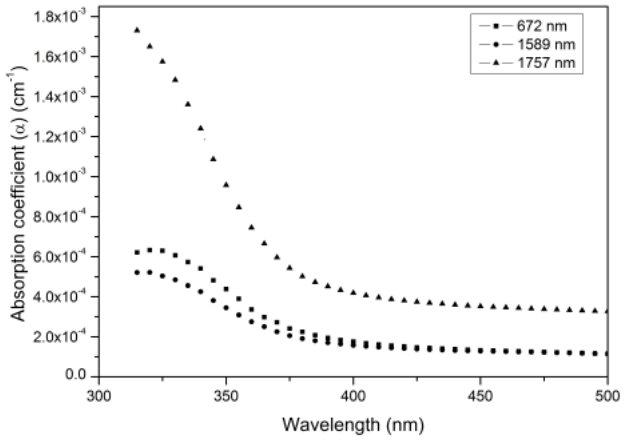

Figure 6.6: Variation of absorption coefficient (α) with wavelength for ceria thin film

In the high absorption region Tauc [8] and Davis and Mott [9] have shown that the absorption coefficient (α) and photon energy (hν) are related by the equation.

$$\alpha h\nu = A(h\nu - E_g)^n \qquad (4)$$

where A is a constant and E_g is the band gap of the material and n has values 1/2, 3/2, 2 and 3 depending on the optical absorption process. Here n = 1/2 is

used for obtaining the direct band gap and n = 2 for indirect band gap. The optical gap E_g is determined by extrapolating the curve $(\alpha h\upsilon)^2$ vs. $h\upsilon$ (Tauc plots) to zero absorption, which gives the value of the direct band gap. Plotting $(\alpha h\upsilon)^{1/2}$ as a function of photon energy ($h\upsilon$), and extrapolating the linear portion of the curve to absorption equal to zero gives the value of the indirect band gap. The Tauc plots are shown in figures 6.7. The variation of direct and indirect bang gap values with film thickness is shown in table 6.3. Both the direct and indirect band gap energies are found to decrease with film thickness. The reduction in the band gap of the as deposited samples is due to the variation of film thickness. The variation in band gap can be explained using size effect in thin films. The variation of band gap with thickness [10] is given by

$$\Delta E = \frac{h}{8m^* t^2} \qquad (5)$$

where m* is the effective mass of electron in the material, t the thickness of the film.

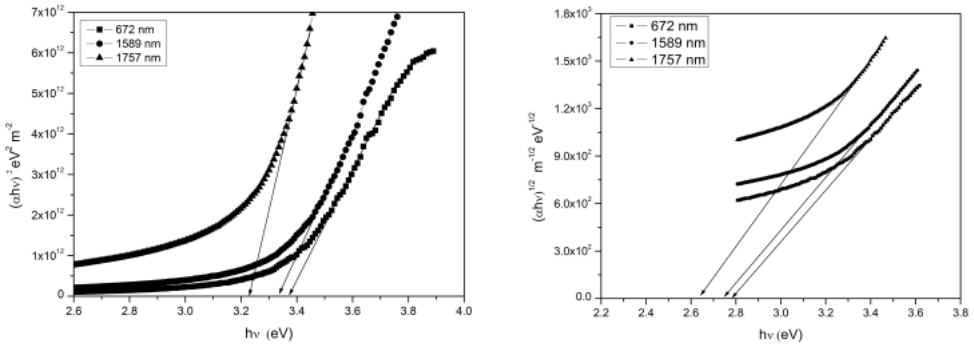

Figure 6.7: Variation of band gap with photon energy

The extinction coefficient (k) was calculated using the relation $\alpha = 4\pi k/\lambda$ and refractive index n by the relation [6]

$$R = \frac{(n-1)^2 + k^2}{(n+1)^2 + k^2} \qquad (6)$$

The variation of refractive index with wavelength is shown in figure 6.8. It increases up to a certain wavelength in UV region and then it decreases exponentially and finally becomes constant in the visible region.

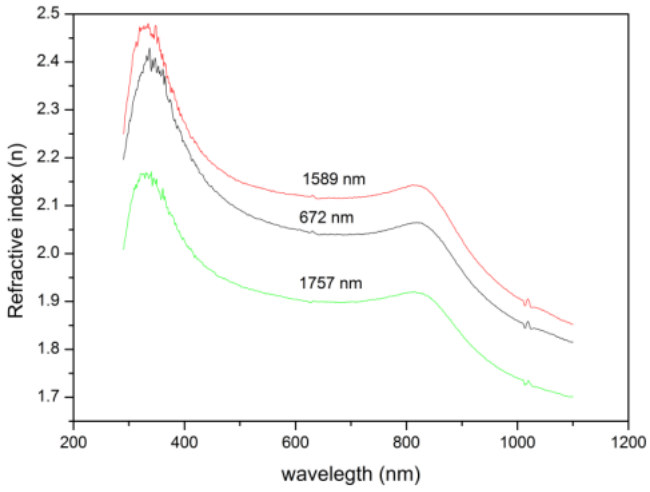

Figure 6.8: Variation of refractive index with wavelength

The variation of refractive index with film thickness at 550 nm is given in table 6.3. The variation of refractive index is in agreement with literature reports in the visible region. The dielectric constant of the as-prepared ceria thin films is expressed as; $\varepsilon_1 = n^2 - k^2$ where ε_1 is the real part the dielectric constant. The dependence of dielectric constant on photon energy with different thickness is shown in figure 6.9. The variations of refractive index with film thickness at 550 nm are given in table 6.3.

Table 6.3: Variations of direct band gap, indirect band gap and refractive index with film thickness.

Film thickness (nm)	Direct band Gap (eV)	Indirect band gap (eV)	Refractive index
672	3.36	2.79	2.065
1589	3.35	2.75	2.090
1757	3.24	2.65	2.133

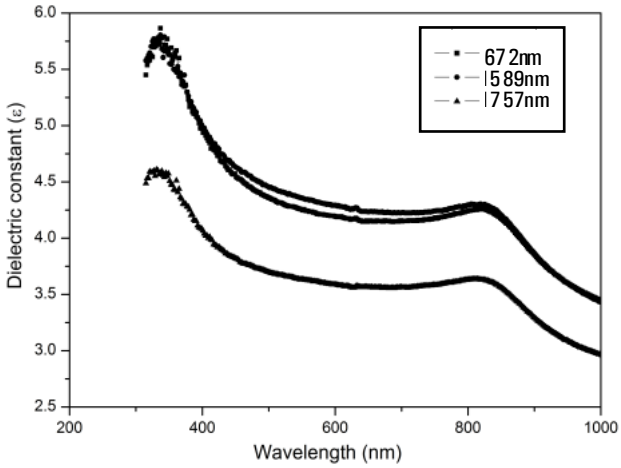

Figure 6.9: Variation of dielectric constant with wavelength.

The room temperature photoluminescence specra of CeO_2 thin films at an excitation wavelength of 325 nm is shown in figure 6.10. The higher thickness films show PL spectra similar to those of nanostructured ceria, as explained in chapter 3. Low thickness film shows PL emission centered around 403 nm. With increasing film thickness most of the characteristic peaks appear in the spectrum.

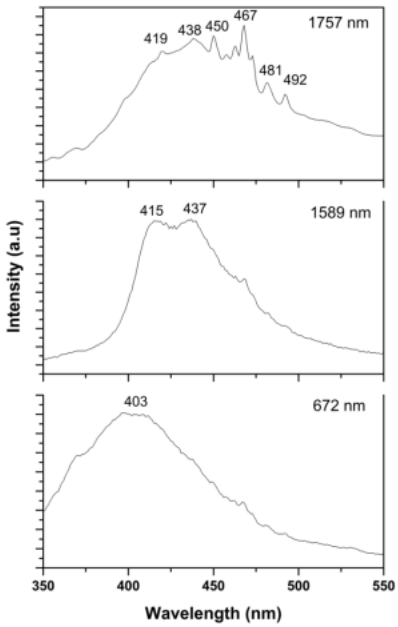

Figure 6.10: PL spectra of ceria thin films with different thicknesses

The PL spectra exhibit a broad-band character from 350 nm to 500 nm. This could be the results of defects including oxygen vacancies in the crystal with electronic energy levels below 4f band and is well explained in chapter 3.3.

The spray pyrolysed ceria thin films with high transmittance in the visible region, high absorbance characteristic in the UV region, are promising for optoelectronic applications. With a band gap of 3.36 eV, good transparency in visible region, nanostructure ceria thin film prepared by spray pyrolysis method can be used as a promising inorganic material for transparent UV filtering films.

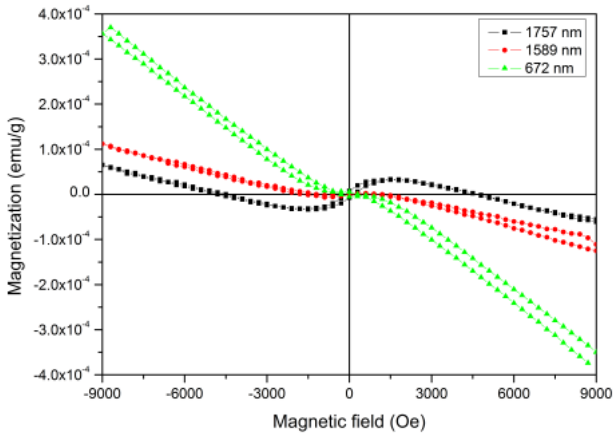

Figure 6.11: Hysteresis loops for cerium oxide thin films with different thickness

The magnetic properties of CeO_2 nanocrystals are characterized by measuring the field dependence of magnetization at room temperature. Figure 6.11 shows the RT magnetization curve of CeO_2 with different thickness in the as-prepared conditions. In this figure CeO_2 appears to be diamagnetic. However, on close examination room temperature ferromagnetism can be observed in these figures which are characterized by a closed hysteresis loop. The origin of ferromagnetism in CeO_2 is assumed to be resulting from the oxygen vacancies at the surface of the nanoparticles and is well explained in the chapter 5.3. With

increasing thickness in cerium oxide films diamagnetic property decreases whereas ferromagnetism increases. Loops are not saturating in lower thickness films due to the presence of diamagnetic component. But it tries to saturate with increase in thickness. Remanence magnetization and coercivity of the ceria thin films are low compared to cerium oxide nanoparticles. Though the remanence magnetization and coercivity are low (Mr-8.86 x 10^{-6} emu/g, Hc-153 Oe) compared to nanostructured powder sample, this is the first time that RTFM has been observed in spray pyrolysed ceria thin films synthesized from $CeCl_3$. The present study is significant since it offers ample scope for optimizing the spray deposition conditions to obtain CeO_2 films with appreciable RTFM.

6.4. Conclusion

Detailed investigations have not been carried out on CeO_2 thin films deposited by spray pyrolysis technique. There are a few reports describing the spray deposition of cerium oxide thin films. However in all these reports the substrate temperature used is quite high which is around 850 K. The highlight of the present work is the fact that good quality cerium oxide thin films could be successfully deposited on glass substrate by spray pyrolysis technique using cost effective precursors such as $CeCl_3$ at comparatively much lower substrate temperatures around 623 K. In the present work the effect of film thickness on the structural, optical and magnetic properties of CeO_2 thin films has been investigated in detail. The most important outcome of the present study is the observation of RTFM in cerium oxide thin films deposited by spray pyrolysis technique, which has not been reported earlier. Although the area of hysteresis loop and the magnetization value are low compared to those of nanostuctured CeO_2 powder sample, the present work offers much scope for further investigations on RTFM in CeO_2 films. By optimizing the deposition conditions it may be possible to improve the ferromagnetic behavior of spray deposited CeO_2 films. This is quite

significance from the view point of the prospecting applications of these cost effective CeO_2 films in the development of spintronic devices.

References

[1] B Elidrissi, M Addou, M Regragui, C Monty, A Bougrine, A Kachouane, Thin Solid Films 379 (2000) 23

[2] T Prasada Rao, M C Santhosh Kumar, Appl. Sur. Sci., 255 (2009) 7212

[3] E Bauer, M H Francombe, H Sato (Eds.), Single Crystal Films, Pergamon, London (1964)

[4] T Prasada Rao, M C Santhosh Kumar, Appl. Sur. Sci., 255 (2009) 4579

[5] B D Cullity, S R Stock, Elements of X-ray Diffraction, 3rd Edn, Prentice Hall, New Jersey (2001)

[6] F Yakuphanoglu, S Ilican, M Caglar, Y Caglar, J. Optoelectronics & Advanced Materials 9 (2007) 2180

[7] S Debnath, M R Islam, M S R Khan, Bull. Mat. Sci. 30 (2007) 315

[8] J Tauc, in F Abels (Ed.), Optical Properties of Solids, North Hlland, Amsterdam (1970)

[9] E A Davis, N F Mott, Phil. Mag. 22 (1970) 903

[10] K L Chopra, Thin film phenomena, McGraw-Hill book Company, New York (1969)

Chapter 7

SYNTHESIS, STRUCTURAL AND OPTICAL PROPERTIES OF POLYMER/CERIA NANOCOMPOSITES

Contents

7. 1. Introduction

The synthesis of polymeric matrixes embedded with nanoparticles has attracted much interest in the field of nanomaterials. Polymers are considered as good choice as host materials, because they can be designed to yield a variety of bulk physical properties, and they normally exhibit long term stability and posses flexible reprocessability. This new class of inorganic-polymer composites may afford potential applications in molecular electronics, optics, photo electrochemical cells, solvent-free coatings etc. Synthesis of polymer/nanoparticles composite materials is very important in advanced material science. These materials combine both the unique properties of nanoparticles and polymers and possess new properties which are not specific to the original components. The polymer matrix also prevents extremely active nanoparticles from aggregation. The addition of inorganic spherical nanoparticles to polymers allows the modification of polymers physical properties as well as the implementation of new features of inorganic nanoparticles.

Polymer nanocomposite structures provide a new method to improve the processability and stability of materials with interesting optical properties. Inorganic /polymer nanocomposites benefit from physical flexibility and ease of processing, which are typical features of polymers. Further, nanocrystals dispersed in suitable solid hosts can be stabilized for long period of time [1]. In the present work, four different polymers are used as the matrix for nanocerium oxide in the nanocomposite. In this study, CeO_2 nanocrystals have been prepared by hydrolysis assisted chemical method which could be suitably embedded in four polymer matrices (polyvinylidene fluoride (PVDF), poly vinyl alcohol (PVA), polymethyl methacrylate (PMMA) and polystyrene (PS).

PVDF is a special plastic material in the fluoropolymer family; it is used generally in applications requiring the highest purity, strength, and resistance to solvents, acids, bases and heat. Compared to other fluoropolymers, it has an easier melt process because of its relatively low melting point of around 177 °C. It has a low density (1.78 g/cc) and low cost compared to the other fluoropolymers. Polyvinyl alcohol (PVA) has excellent film forming, emulsifying and adhesive properties. It has high tensile strength and flexibility. PVA is fully degradable and dissolves quickly. PVA has a melting point of 230 °C. It decomposes rapidly above 200°C as it can undergo pyrolysis at high temperatures. Polymethyl methacrylate (PMMA) is a transparent thermoplastic, sometimes called acrylic glass. Chemically, it is the synthetic polymer of methyl methacrylate. Polystyrene (PS) is an amorphous, optically clear thermoplastic material, which is often chosen as a host matrix because of its ideal properties for investigating optical properties. It is one of the most extensively used plastic materials.

7.2. Experimental techniques

7.2.1. Synthesis

CeO_2 nanoparticles were prepared by hydrolysis assisted precipitation method as explained in chapter 3. PVDF/ CeO_2 nanocompsite solutions were prepared by adding 10 wt % of CeO_2 powder sample into PVDF solution (10% w/v) in NMP. The mixtures were then stirred for 2h and then sonicated for 10 min [2]. Using the same procedure PVA (dissolved in water)/ CeO_2, PMMA (dissolved in Tetrahydrofuran)/CeO_2 and PS (dissolved in tetrahydrofuran)/ CeO_2 nanocomposites were also prepared.

7.2.2. Characterizations

XRD studies were carried out for the polymer/CeO_2 nanocomposites using a Rigaku Ultima-III X-Ray Diffractometer using Cu $K\alpha_1$ radiation in the 2θ range from 10^0 to 70^0. Optical absorption studies were carried out using JASCO V 570 Spectrophotometer at room temperature. Photoluminescence spectra of composite samples were obtained using Flouromax-3 Spectrophotometer at room temperature under an excitation of 325 nm.

7.3. Results and discussion

XRD patterns of various polymer/ceria nanocomposites are shown in figure 7.1. These indicate broad non crystalline peaks of polymer and sharp peaks of cerium oxide. The diffraction peaks corresponding to (111), (200), (220) and (311) planes indicate cubic structure of CeO_2 (JCPDS 34-0394). The broadening of XRD peaks indicates formation of nanosized particles in the as-prepared sample. The presence of CeO_2 produces neither new peaks nor peaks shift with respect to polymer showing that nano CeO_2 filled polymer composites consist of two phase structures.

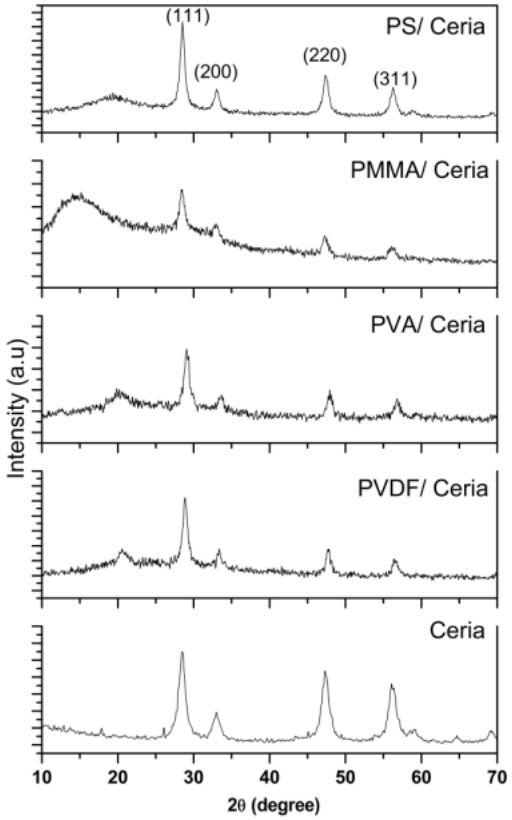

Figure 7.1: XRD patterns of the polymer/ CeO_2 nanocomposites

UV-Vis absorption spectra of the polymer/CeO_2 nanocomposites are shown in figure 7.2. Pure ceria shows a sharp absorption peak around 298 nm and an absorption edge at 387 nm which is explained in chapter 3.3. In PMMA, PVA and PVDF/ceria nanocomposites the absorption edge shifts to longer wavelength side. But in PS/ceria nanocomposite absorption edge is almost at 300 nm. In all the composite samples there is a UV absorption window. The width of the window is from 250 nm to 350 nm for all polymer/ceria nanocomposites except for PS/ceria nanocomposite for which it is from 250 nm to 300 nm.

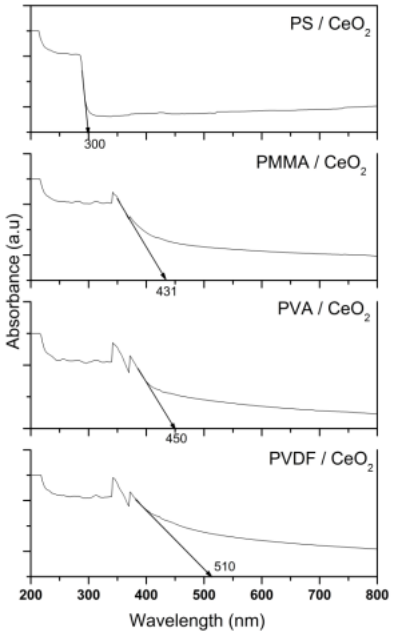

Figure 7.2: UV-Vis absorption spectra of the polymer/ CeO_2 nanocomposites

Pure polymers don't show appreciable UV absorption. But polymer/ceria nanocomposites are covering UV A and UV B regions and part of UV C region, thus showing prospects of acting as efficient UV filters. The mechanism of UV absorption in these materials involves the use of photon energy to excite electrons from the valence band to conduction band.

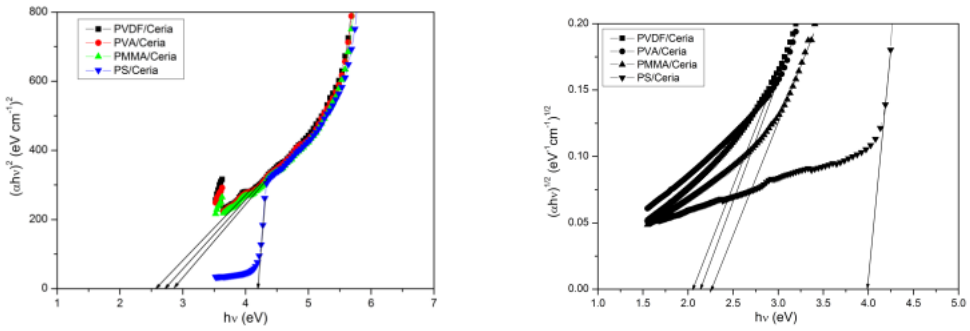

(a) Direct band gap (b) Indirect band gap

Figure 7.3: Band gap energy of the polymer/ CeO_2 nanocomposites

Direct and indirect band gap energies of polymer/CeO_2 nanocomposites are shown in figure 7.3 (a & b). Table 7.1. shows direct and indirect band gap energies of polymer/CeO_2 nanocomposites.

Table 7.1: Direct and indirect band gap energies of polymer/CeO_2 nanocomposites

Sample	Direct band gap (eV)	Indirect band gap (eV)
PVDF/Ceria	2.43	2.05
PVA/Ceria	2.75	2.14
PMMA/Ceria	2.87	2.26
PS/Ceria	4.13	3.99

The present findings reveal an enhanced band gap in the range of 4.13 eV for PS/ceria nanocomposite. So it could be used as a better photocatalyst. Light below this wavelength has sufficient energy to excite electrons and hence absorbed by CeO_2. Light having a wavelength longer than the band gap energy (towards the visible light) will not be absorbed. Therefore PS/CeO_2 nanocomposite is an excellent UV absorber [3].

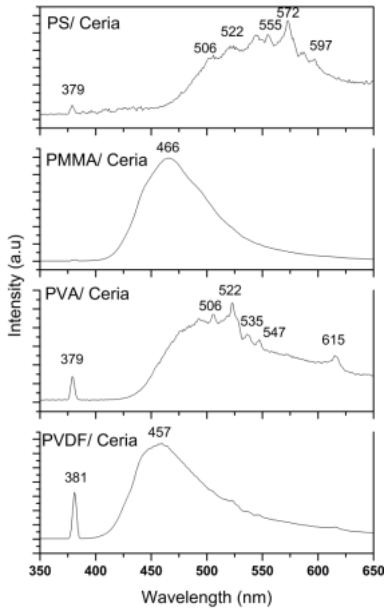

Figure 7.4: PL spectra of the polymer/ CeO_2 nanocomposites

PL spectra of the as-prepared polymer/CeO_2 nanocomposites are shown in figure 7.4. PL studies of polymer/ceria nanocomposites are done to investigate the effects of the polymer matrix on the PL characteristics of ceria. Pure ceria shows a series of high intensity PL emission peaks in the blue-green region and also lower intensity peaks in the UV region which are well explained in chapter 3.3. Polymer matrix provides surface passivation of the ceria nanoparticles and hence modifies the PL spectrum. Passivation effect is highly pronounced in PMMA/Ceria nanocomposite. The PMMA/Ceria nanocomposite has the most intense PL emission peak at 466 nm compared to pure ceria and other polymer composites.

It is observed that free standing films of PS/ceria, PMMA/ceria and PVDF/ceria can be obtained with thickness around 1μm using solution casting. These nanocomposite films also show high dielectric constant value around 20. Due to time constraint, detailed investigations on the various properties of these films couldnot be carried out.

7.4. Conclusion

Polymer/ceria nanocomposites using four different polymers have been successfully synthesized. These nanocomposites show good UV absorption window regions. Polymer matrix provides surface passivation of the ceria nanoparticles and hence modifies the PL spectra. Passivation effect is highly pronounced in PMMA/Ceria nanocomposite.

It is observed that free standing polymer nanocomposite films of ceria can be prepared using PS, PMMA and PVDF which show considerably high dielectric constant values ($\backsim$20). These free standing high dielectric constant nanocomposite films can be of profound applications as gate electrodes for metal oxide semiconductor devices.

References

[1] L L Beecroft, C K Ober, Chem. Mater., 9 (1997) 1302

[2] P P Jeeju, A M Sajimol, V G Sreevalsa, S J Varma, S Jayalekshmi, Polym. Int., 60 (2011) 1263

[3] P K Khanna, N Singh, S Charan, Mat. Lett. 61 (2007) 4725

Chapter 8
SUMMARY AND CONCLUSION

Contents

8.1. General conclusion

Synthesis and processing of nanomaterials and nanostructures are the essential aspects of nanotechnology. Studies on new physical properties and applications of nanomaterials and nanostructures are possible only when nanostructured materials are made available with desired size, morphology, crystal structure and chemical composition. Among the topics of current interest in material science, the identification of rare earth compounds with desirable properties has attracted much attention owing to their wide applications. Among them, cerium oxide (ceria) is one of the important functional materials with high mechanical strength, thermal stability, excellent optical properties, appreciable oxygen ion conductivity and oxygen storage capacity. Ceria finds a variety of applications in mechanical polishing of microelectronic devices, as catalysts for three-way automatic exhaust systems and as additives in ceramics and phosphors[1].

Recently, several methods have been developed to prepare pure and doped CeO_2 powder, including wet chemical synthesis, thermal hydrolysis, flux method, hydrothermal synthesis, gas condensation method, microwave technique etc. In all these, some special reaction conditions, such as high temperature, high pressure, capping agents, expensive or toxic solvents etc. have been involved.

The large scale production of powders needs to be economically feasible and should not be more complex. So compared to these methods, chemical precipitation is more attractive due to the use of cheap salt precursors and simple operation[1]. Although CeO_2 in doped and pristine forms have already been studied, there are no reports on the systematic investigations related to the synthesis and properties of nanostructured cerium oxide (both in pristine and doped forms) using the cost effective technique of hydrolysis assisted chemical precipitation method.

In the present work nanocrystalline CeO_2 powder samples have been prepared by hydrolysis assisted chemical precipitation method employing cerium chloride and ammonia as precursors. XRD and TEM studies confirm the formation of the fluorite CeO_2 nanopartilces of average size around 10 nm. Extensive investigations have been carried out on the structural and optical properties of nanostructured ceria and iron, aluminum and cobalt doped ceria. One of the high-lights of these studies is the observation that both pure and doped ceria offer the prospects of applications as cost effective and non toxic inorganic material for efficient UV filtering in sunscreen cosmetics.

One of the objectives of the present investigation is to look for room temperature ferromagnetism in nanostructured ceria and doped ceria (iron and cobalt) synthesized using the hydrolysis assisted chemical precipitation technique. RTFM has been observed for the first time in pure ceria nanocrystals synthesized by chemical precipitation technique and also in iron and cobalt doped ceria nanocrystals. The origin of RTFM has been ascribed to the presence of oxygen vacancies on the surface of ceria nanopartilces[2]. Based on the experimental data good correlation between the magnetic, structural and optical properties of these samples has also been established.

Photoluminescence has already been reported in cerium oxide synthesized by variety of techniques. In the present work detailed investigation has been carried out on the PL characteristics of cerium oxide nanocrystals. Based on the dependence of PL intensity on annealing temperature a self trapped exciton (STE) mediated PL mechanism has been proposed for the observed photoluminescence in ceria nanocrystals. Though STE mechanism has been reported in some oxide systems such as Li_2O_3, $SrTiO_3$ etc. [3]. it is the first time that such a mechanism is being proposed for PL emission in cerium oxide nanocrystals.

Another high-light of the present work is room temperature ferromagnetism in cerium oxdie thin films deposited by spray pyrolysis technique. High quality CeO_2 thin films could be deposited by the cost effective spray pyrolysis technique at comparatively much lower substrate temperatures around 623 K using simple precursors, $CeCl_3$. There are no reports on RTFM in spray deposited ceria films.

Though the magnetization value is much lower compared to that of cerium oxide powder, the present work offers much scope for detailed investigations on RTFM in cerium oxide films. It should be possible to optimize the spray deposition conditions to improve the FM properties of CeO_2 films with the prospects of applications in developing cost effective spintronic devices.

The field of polymer/ceria nanocomposite with inorganic filler nanomaterials has gained worldwide research attention owing to versatile applications of these nanocomposites in many branches of science and technology. In the present work attempts has been made to synthesize ceria/polymer nanocomposites using a variety of polymers such as PVDF, PVA, PMMA and PS. It is observed that these polymer/ceria nanocomposites possess good UV absorption window regions of approximately 250 nm width.

Hence these nanocomposites having practical applications in developing UV filters.

8.2. Future scope of the present work

The observation of RTFM in CeO_2 nanocrystals and iron and cobalt doped CeO_2 synthesized using surfactant free hydrolysis assisted chemical precipitation is one of the highlights of the present investigations. Another important result is the observation of RTFM in CeO_2 thin films deposited by spray pyrolysis technique. The present investigations offer ample scope for further studies related to RTFM in CeO_2 thin films which has not been pursued widely. It should be possible to optimize the deposition conditions of CeO_2 films in order to improve the FM behavior of CeO_2 films.

The observation of self trapped exciton mediated PL in ceria nanocrystals is another important outcome of the present study. STE mediated mechanism has been proposed for CeO_2 nanocrystals based on the dependence of PL intensity on the annealing temperature. It would be interesting to extent these investigations to the doped forms of cerium oxide and cerium oxide thin films to get deeper insight into STE mechanism.

Due to time constraints detailed investigations could not be carried out on the preparation and properties of free standing films of polymer/ceria nanocomposites. It has been observed that good quality free standing films of PVDF/ceria, PS/ceria, PMMA/ceria can be obtained using solution casting technique. These polymer nanocomposite films show high dielectric constant around 20 and offer prospects of applications as gate electrodes in metal-oxide semiconductor devices.

References

[1] H Chen, H Chang, Colloids and Surfaces A: Physicochem.Eng. Aspects 242 (2004) 61

[2] A Sudaresan, R Bhargavi, N Rangarajan, U Siddesh, C N R Rao, Phys. Rev. B 74 (2006) 161306 (R)

[3] W F Zhang, Z Yin, M S Zhang, Z L Du, W C Chen, J. Phys: Condens. Matter 11 (1999) 5655

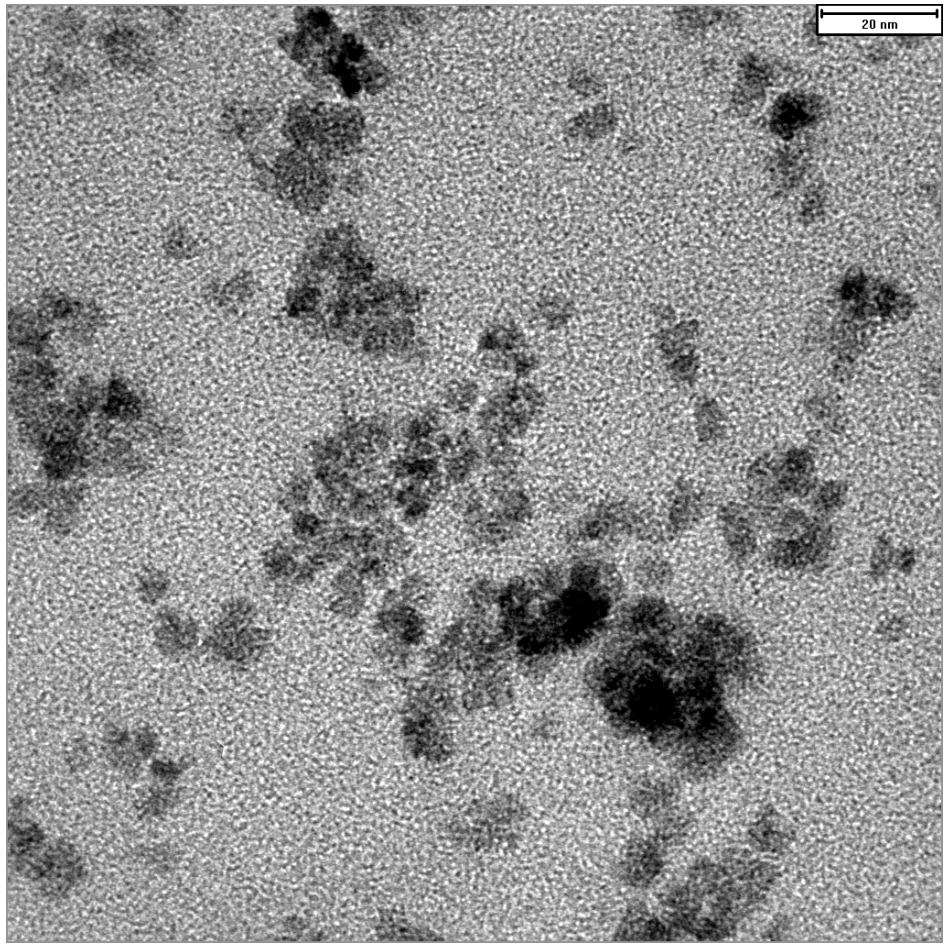

(a)$Ce_{0.95}Fe_{0.05}O_{2-\delta}$

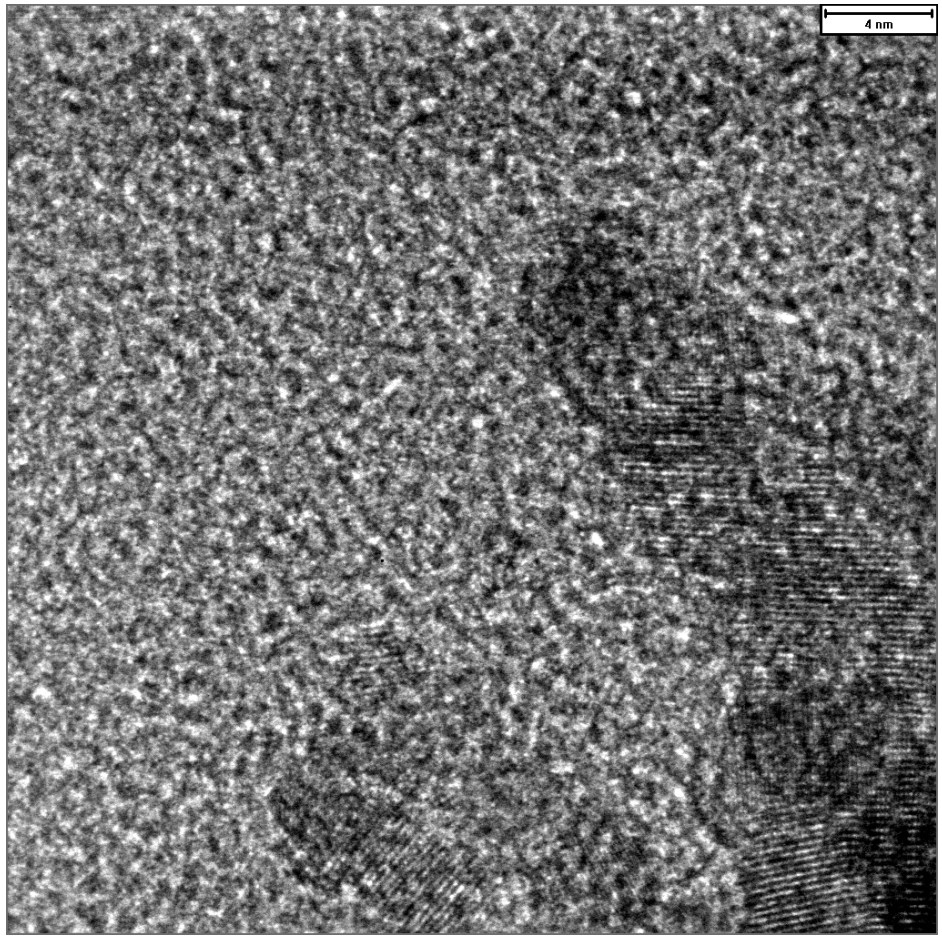

(d) $Ce_{0.95}Al_{0.05}O_{2-\delta}$

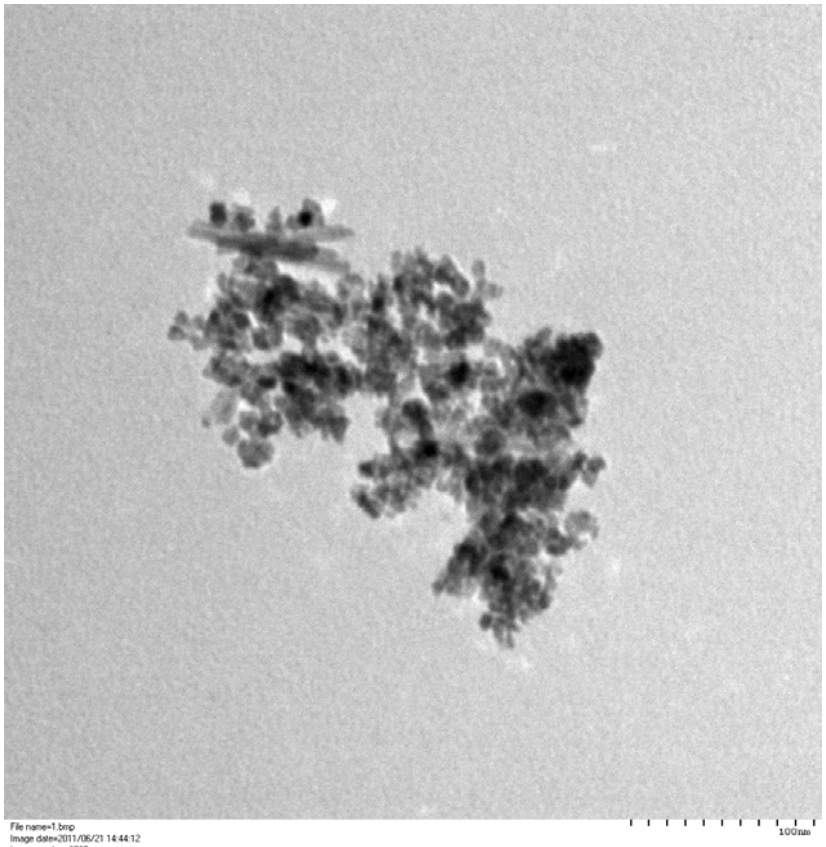

(g)$Ce_{0.95}Co_{0.05}O_{2-\delta}$